

---

# SEARCH FOR TOP SQUARK VIA ALL-HADRONIC DECAY CHANNELS WITH HEAVY OBJECT TAGGING

---



Thesis: Doctor of Philosophy  
Physics and Astronomy  
Rice University, Houston, Texas (October 2019)

RICE UNIVERSITY

**Search for Top Squark via All-Hadronic Decay  
Channels with Heavy Object Tagging**

by

**Matthew Cavenaugh Kilpatrick**

A THESIS SUBMITTED  
IN PARTIAL FULFILLMENT OF THE  
REQUIREMENTS FOR THE DEGREE

**Doctor of Philosophy**

APPROVED, THESIS COMMITTEE:

---

Karl Ecklund, Chair  
Associate Professor of Physics and  
Astronomy

---

Paul Padley  
Professor of Physics and Astronomy

---

David Scott  
Noah Harding Professor

Houston, Texas

October, 2019

ABSTRACT

Search for Top Squark via All-Hadronic Decay Channels with Heavy Object  
Tagging

by

Matthew Cavanaugh Kilpatrick

# Contents

Abstract	ii
List of Figures	vi
List of Tables	ix
<b>1 Introduction</b>	<b>1</b>
1.1 Motivation . . . . .	1
<b>2 Supersymmetry and the Standard Model</b>	<b>2</b>
2.1 The Standard Model . . . . .	2
2.1.1 The Fundamental Particles . . . . .	2
2.1.2 Quantum Field Theory . . . . .	3
2.1.3 Noether's Theorem . . . . .	3
2.1.4 Quantum Electrodynamics (QED) . . . . .	5
2.1.5 Quantum Chromodynamics . . . . .	8
2.1.6 Weak Force . . . . .	10
2.1.7 The Electroweak Lagrangian . . . . .	12
2.1.8 The Higgs Mechanism . . . . .	14
2.1.9 Electroweak . . . . .	16
2.1.10 The Standard Model Lagrangian . . . . .	17
2.2 Fundamental Problems in the Standard Model . . . . .	18
2.2.1 Dark Matter . . . . .	18
2.2.2 Hierarchy Problem . . . . .	19
2.2.3 Grand Unified Theory . . . . .	20
2.3 Supersymmetry . . . . .	21
2.3.1 Supermultiplets and Chirality . . . . .	23

2.3.2	Minimal Supersymmetric Standard Model . . . . .	23
2.3.3	R Parity . . . . .	25
2.3.4	Mass Spectrums . . . . .	26
2.3.5	Supersymmetry Searches . . . . .	27
2.4	Current SUSY Results . . . . .	28
2.5	What are we looking for? And why? . . . . .	32
<b>3</b>	<b>Compact Muon Solenoid</b>	<b>33</b>
3.1	The Detector . . . . .	33
3.1.1	Tracker . . . . .	34
3.1.2	Electromagnetic Calorimeter . . . . .	38
3.1.3	Hadronic Calorimeter . . . . .	40
3.1.4	Superconducting solenoid . . . . .	41
3.1.5	Muon Chambers . . . . .	41
3.2	Detector Methods . . . . .	42
<b>4</b>	<b>Search Strategy</b>	<b>44</b>
4.1	Physics Objects . . . . .	44
4.1.1	Jets . . . . .	44
4.1.2	Heavy Object Tagging . . . . .	45
4.1.3	Missing Transverse Momentum . . . . .	47
4.1.4	$H_T$ . . . . .	48
4.1.5	Soft $b$ -Tagging . . . . .	48
4.1.6	Transverse Energy between $b$ quarks and $\cancel{E}_T$ . . . . .	50
4.1.7	Initial-state Radiation . . . . .	50
4.1.8	Electron and Muon Identification . . . . .	50
4.1.9	Tau Identification . . . . .	51
4.2	Samples . . . . .	52
4.2.1	Filters . . . . .	55
4.3	Baseline Selection . . . . .	56
4.3.1	Search Regions . . . . .	57

<b>5 Top Squark Production and Backgrounds</b>	<b>62</b>
5.1 Production and Decay Modes . . . . .	62
5.2 Standard Model Background . . . . .	64
5.3 Lost Lepton . . . . .	65
5.3.1 Combining All Run 2 Eras . . . . .	65
5.3.2 Transfer Factors . . . . .	66
5.4 Z Boson Decay to Neutrinos . . . . .	82
5.5 Quantum Chromodynamic Events . . . . .	83
5.6 Rare Interactions . . . . .	97
<b>6 Uncertainties and Estimation</b>	<b>99</b>
6.1 Systematic Uncertainties . . . . .	99
6.2 Validation . . . . .	101
6.3 Combination of Search region . . . . .	106
6.4 Higgs Combined Tool . . . . .	109
<b>A Tau Multivariate Analysis</b>	<b>110</b>
<b>Appendix A</b>	<b>110</b>
<b>Bibliography</b>	<b>114</b>
<b>Bibliography</b>	<b>114</b>

# Figures

2.1	Standard Model particles . . . . .	4
2.2	QED Feynman Diagrams . . . . .	7
2.3	QCD Feynman Diagrams . . . . .	10
2.4	CKM Matrix Couplings . . . . .	11
2.5	Weak Feynman Diagrams . . . . .	12
2.6	Hierarchy Problem Loop Correction . . . . .	19
2.7	GUT Force Energy Dependence . . . . .	21
2.8	Supersymmetry and Standard Model Particles . . . . .	22
2.9	Top squark mass hierarchy . . . . .	26
2.10	T2tt Limits . . . . .	29
2.11	T2bW Limits . . . . .	29
2.12	T2tb Limits . . . . .	30
2.13	T2fbd Limits . . . . .	30
2.14	T2bWC Limits . . . . .	31
2.15	T2tt Limits for all decay modes . . . . .	31
3.1	CMS Cross Section . . . . .	34
3.2	CMS Tracker Geometry . . . . .	35
3.3	Pixel Modules . . . . .	36
3.4	FED Throughput . . . . .	37
3.5	Strip Tracker Module . . . . .	39
3.6	Muon Chambers . . . . .	42
4.1	Jet Hadronization . . . . .	45

4.2	Top Decays	46
4.3	Secondary Vertex Diagram	49
4.4	Top Squark Decay Modes	59
5.1	Direct stop production	63
5.2	Gluino mediated stop production	64
5.3	Lost Lepton LM Eras	66
5.4	Lost Lepton HM Eras	67
5.5	Transfer Factor Comparison	69
5.6	Separated Transfer Factor Comparison	70
5.7	Lost Lepton LM Control Region $N_b = 0$	71
5.8	Lost Lepton LM Control Region $N_b = 1$	76
5.9	Lost Lepton HM Control Region	77
5.10	Lost Lepton HM Control Region $N_b = 1$	78
5.11	Lost Lepton HM Control Region $N_b = 2$ with 1 heavy object	79
5.12	Lost Lepton HM Control Region $N_b = 2$ with 2 heavy objects	80
5.13	Lost Lepton HM Control Region $N_b \geq 3$ with 1 heavy object	81
5.14	QCD Multijet LM Control Region $N_b = 0$	85
5.15	QCD Multijet LM Control Region $N_b = 1$	89
5.16	QCD Multijet HM Control Region	90
5.17	QCD Multijet HM Control Region $N_b = 1$	91
5.18	QCD Multijet HM Control Region $N_b = 2$ with 1 heavy object	92
5.19	QCD Multijet HM Control Region $N_b = 2$ with 2 heavy objects	93
5.20	QCD Multijet HM Control Region $N_b \geq 3$ with 1 heavy object	94
5.21	Light Jet Response	95
5.22	B Jet Response	96
6.1	LM Validation Region	102
6.2	Lost Lepton HM Control Region	103
6.3	Example Datacard of T2tt(175,1)	107
6.4	Example Datacard of LL CR	107

6.5 Example Datacard of QCD CR . . . . .	108
A.1 Tau MVA ROC Curve . . . . .	111
A.2 Tau MVA Discriminator . . . . .	112

# Tables

2.1	Fermion Currents . . . . .	6
2.2	Chiral supermultiplets for fermions and bosons . . . . .	24
2.3	Chiral supermultiplets for gauge bosons . . . . .	24
4.1	Data Samples . . . . .	53
4.2	Standard Model Samples . . . . .	54
4.3	Signal Samples . . . . .	55
4.4	Low $\Delta m$ Search Regions . . . . .	60
4.5	High $\Delta m$ Search Regions . . . . .	61
5.1	The LL estimate in the various low $\Delta m$ search regions, bins 0 to 53, using the $136.7 \text{ fb}^{-1}$ dataset. . . . .	72
5.2	The LL estimate in the various high $\Delta m$ search regions, bins 53-93, using the $136.7 \text{ fb}^{-1}$ dataset. . . . .	73
5.3	The LL estimate in the various high $\Delta m$ search regions, bins 94-134, using the $136.7 \text{ fb}^{-1}$ dataset. . . . .	74
5.4	The LL estimate in the various high $\Delta m$ search regions, 135-182, using the $136.7 \text{ fb}^{-1}$ dataset. . . . .	75
6.1	Low $\Delta m$ Search Regions . . . . .	104
6.2	High $\Delta m$ Search Regions . . . . .	105
A.1	TauMVA Background Optimization . . . . .	113
A.2	TauMVA Signal Optimization . . . . .	113

A.3 Tau Identification Comparisons . . . . .	113
--	-----

## Chapter 1

### Introduction

#### 1.1 Motivation

## Chapter 2

# Supersymmetry and the Standard Model

The fundamental theory of particle physics, known as the Standard Model (SM) can predict interactions between the fundamental particles in our universe. With these predictions we can look for and confirm these processes, but there are some aspects of the universe that have not yet been explained. In this Chapter, we will analyze the Standard Model, look at some specific shortcomings, and introduce supersymmetry as a possible solution.

### 2.1 The Standard Model

After decades of theoretical and experimental research the SM has been developed into a theory that explains the Electromagnetic (EM), Strong, and Weak forces. The SM has not yet been able to include Gravity within the theory. With the robust theoretical and experimental methods used in the SM, we have discovered new elementary particles and predicted others.

#### 2.1.1 The Fundamental Particles

All matter can be explained by three kinds of elementary particles: leptons, quarks, and gauge bosons. Each of these can be distinguished by various quantum properties. The leptons and quarks are fermions, which are particles that have half-integer spin. Leptons are particles that only interact with the EM and Weak force,

while quarks interact with all three forces of the SM. The gauge bosons are the force carriers for each respective force and have integer spin.

There are three generations of leptons and quarks which are differentiated by a charge  $\pm e$ , the charge of an electron, and the mass of the respective lepton. Leptons have three different charged particles: electron ( $e$ ), muon ( $\mu$ ), and tau ( $\tau$ ), with each charged particle having a corresponding neutrino ( $\nu$ ) of the same flavor, see fig 2.1. Quarks are also separated into three generations of doublets, the down-type ( $-\frac{1}{3}e$ ): down ( $d$ ), strange ( $s$ ), and bottom ( $b$ ) and up-type ( $\frac{2}{3}e$ ): up ( $u$ ), charm ( $c$ ), and top ( $t$ ), see fig 2.1. Each of the quarks has a color associated with it which is analogous to an electric charge, except there are three colors charges: red, blue, and green.

### 2.1.2 Quantum Field Theory

The interactions of all these particle fields are described by quantized fields whose operators describe the creation and annihilation of particles. Each of the particle fields of the SM have a corresponding gauge boson which is described by a quantized gauge field, see fig. 2.1. The most well-known being the EM field and its interactions. In order to write a concise theory of the particles in the SM, the symmetry and conservation laws of the SM can be derived by starting with Noether's Theorem.

### 2.1.3 Noether's Theorem

Noether's theorem states, "to each symmetry of a local Lagrangian, there corresponds a conserved current" [2]. This can be done by allowing for an infinitesimal symmetry variation. Requiring the Lagrangian to be invariant under  $\phi(x) \rightarrow \phi'(x) = \phi(x) + \alpha\Delta\phi(x)$ , where  $\alpha$  is infinitesimal real parameter and  $\Delta\phi$  is a deformation to

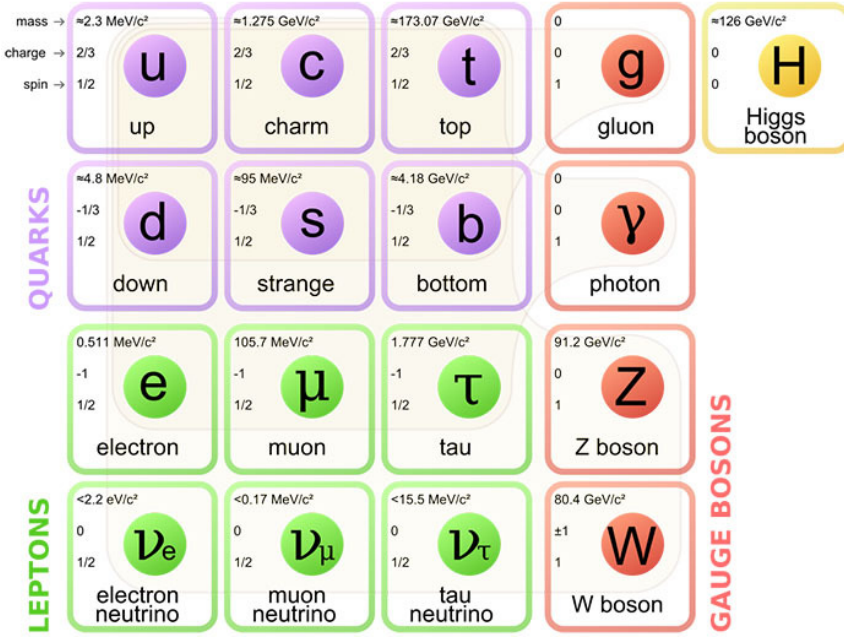


Figure 2.1 : The fundamental particles of the Standard Model. There are three generations of quarks and leptons. Along with the five bosons, where four of them relate to the interactions of the three forces included in the SM: Electromagnetism, the Weak force, and the Strong force and the final being the Higgs boson.

the field, up to a 4-divergence, the Lagrangian transforms as,

$$\mathcal{L}(x) \rightarrow \mathcal{L}(x) + \alpha \partial_\mu \mathcal{J}^\mu(x), \quad (2.1)$$

where  $\mathcal{J}^\mu$  is a current. If we apply the Euler-Lagrange equation,

$$\partial_\mu \left( \frac{\partial \mathcal{L}}{\partial (\partial_\mu \phi)} \right) - \frac{\partial \mathcal{L}}{\partial \phi} = 0, \quad (2.2)$$

to Eqn. 2.1 with the addition of the fluctuation of the particle field. After some simplification we get a conserved current [1, 2],

$$\begin{aligned} \partial_\mu j^\mu(x) &= 0, \text{ where} \\ j^\mu(x) &= \frac{\partial \mathcal{L}}{\partial (\partial_\mu \phi)} \Delta \phi - \mathcal{J}^\mu. \end{aligned} \quad (2.3)$$

We see from the above equation that the current  $j^\mu(x)$  of the Lagrangian is conserved. Now let's apply this to the particle fields of the SM.

#### 2.1.4 Quantum Electrodynamics (QED)

First, we start with the assumption that the wave function  $\psi(x)$  should transform as,

$$\psi(x) \rightarrow e^{i\alpha(x)} \psi(x), \quad (2.4)$$

where  $\alpha(x)$  has an arbitrary dependence on space and time. If one were to include this into the Lagrangian for a spin-1/2 particle in a vacuum,

$$\mathcal{L}_{QED}^{vac} = i\bar{\psi} \gamma^\mu \partial_\mu \psi - m\bar{\psi} \psi \quad (2.5)$$

Type	Form	Components	Space Inversion
Scalar	$\bar{\psi}\psi$	1	+ under $P$
Vector	$\bar{\psi}\gamma^\mu\psi$	4	Space comps.: - under $P$
Tensor	$\bar{\psi}\sigma^{\mu\nu}\psi$	6	
Axial Vector	$\bar{\psi}\gamma^5\gamma^\mu\psi$	4	Space comps.: + under $P$
Pseudoscalar	$\bar{\psi}\gamma^5\psi$	1	- under $P$

Table 2.1 : A table showing all forms of the fermion currents. These can be symmetric under parity transformation in all or some components.

where the  $\gamma^\mu$  are the Dirac matrices,  $\partial_\mu$  is the partial derivative,  $\bar{\psi}$  is the hermitian conjugate of the wave function  $\psi$ , and  $m$  is the mass of the particle. As a small aside, the bilinear quantities  $\bar{\psi}(4 \times 4)\psi$  have certain properties under Lorentz transformations when the  $4 \times 4$  matrix is a  $\gamma$ -matrices. These are of the form,

$$\gamma^0 = \begin{bmatrix} \mathbf{I} & 0 \\ 0 & -\mathbf{I} \end{bmatrix}, \boldsymbol{\gamma} = \begin{bmatrix} 0 & \boldsymbol{\sigma} \\ -\boldsymbol{\sigma} & 0 \end{bmatrix}, \gamma^5 = \begin{bmatrix} 0 & \mathbf{I} \\ \mathbf{I} & 0 \end{bmatrix} \quad (2.6)$$

where the  $\mathbf{I}$  is the identity matrix and  $\boldsymbol{\sigma}$  are the Dirac matrices. We can combine the first two parts of Eqn. 2.6 and write it compactly as  $\gamma^\mu$  where  $\mu = 0, 1, 2$ , and 3. The possible interesting quantities of the above transformations are shown in Table 2.1.

To allow for the field to be invariant, we must include a derivative,  $D_\mu$ , that is covariant under phase transformations,

$$D_\mu \equiv \partial_\mu - ieA_\mu. \quad (2.7)$$

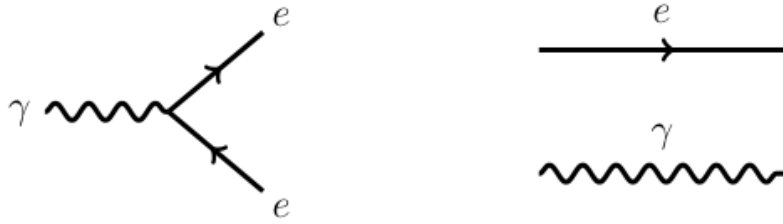


Figure 2.2 : The possible Feynman diagrams in QED. The  $e$  can be replaced with any spin-1/2 charged particle. We see that the electron and photon can propagate freely in space or a vertex with one photon and a particle-antiparticle pair is allowed.

The covariant derivative includes the vector field  $A_\mu$  which must also transform as,

$$A_\mu \rightarrow A_\mu + \frac{1}{e} \partial_\mu \alpha. \quad (2.8)$$

So after requiring that there be a local gauge transformation, we were forced to introduce a vector field  $A_\mu$ , called the gauge field, which couples to Dirac particles in the same way as the photon field. We will think of this new field as the real photon field, which means we need to add a kinematic energy portion to the Lagrangian. This kinematic term will be invariant under Eqn. 2.8, which leads us to final representation of the QED Lagrangian which can be written down concisely as,

$$\mathcal{L}_{QED} = \bar{\psi}(i\gamma^\mu \partial_\mu - m)\psi + e\bar{\psi}\gamma^\mu A_\mu \psi - \frac{1}{4}F^{\mu\nu}F_{\mu\nu}, \quad (2.9)$$

where  $A_\mu$  is the EM field operator and  $F^{\mu\nu}$  is the EM field tensor. This Lagrangian describes the interactions between spin-1/2 charged particles and the  $U(1)$  EM force. Each of the parts of this equation is Lorentz invariant which allows this to be true in all reference frames.

From the QED Lagrangian Eqn. 2.9, we see that particles that interact elec-

tromagnetically can interact with the photon. This can be shown as a Feynman diagram, see Fig. 2.2, which has a vertex interaction with a photon and a particle-antiparticle pair. These, and the inclusion of freely moving particles, are the basic types of Feynman diagrams for QED.

### 2.1.5 Quantum Chromodynamics

Let's now transition from the description of the  $U(1)$  EM field to the  $SU(3)$  Quantum Chromodynamic (QCD) field and the transformation of quark fields. A quark in a vacuum is described by,

$$\mathcal{L}_{QCD}^{vac} = \bar{q}_j(i\gamma^\mu \partial^\mu - m)q_j, \quad (2.10)$$

where  $q_1, q_2$ , and  $q_3$  are quark fields with three possible color charges. From this we want to require that the field is again invariant under another local phase transformation such as,

$$q(x) \rightarrow Uq(x) \equiv e^{i\alpha_a(x)T_a}q(x), \quad (2.11)$$

where  $U$  is a  $3 \times 3$  unitary matrix,  $T_a$  with  $a = 1, \dots, 8$  are a set of linearly independent traceless  $3 \times 3$  matrices, and  $\alpha_a$  are the group parameters. Since the generators  $T_a$  do not necessarily commute with each other, we can see that it is a non-Abelian transformation and the commutator can be represented as,

$$[T_a, T_b] = if_{abc}T_c, \quad (2.12)$$

where  $f_{abc}$  are constants.

We need to impose  $SU(3)$  local gauge invariance on Eqn. 2.10, to allow for the

following phase transformations,

$$\begin{aligned} q(x) &\rightarrow (1 + i\alpha_a(x)T_a)q(x), \\ \partial_\mu q &\rightarrow (1 + i\alpha_a T_a)\partial_\mu q + iT_a q \partial_\mu \alpha_a. \end{aligned} \tag{2.13}$$

From this it seems straight forward that we can proceed in exactly the same manner as QED, which is to add a transformation to the derivative,

$$D_\mu = \partial_\mu + ig_Q T_a G_\mu^a. \tag{2.14}$$

where the field  $G_\mu^a$ , which are the gluons, transforms as,

$$G_\mu^a \rightarrow G_\mu^a - \frac{1}{g_Q} \partial_\mu \alpha_a, \tag{2.15}$$

where  $g_Q$  is the coupling strength of QCD interactions. This will give us a similar Lagrangian to the QED one described above, but this is not sufficient for a non-Abelian gauge transformation and it does not produce a gauge-invariant Lagrangian. One final transformation is required for the  $G_\mu^a$  fields,

$$G_\mu^a \rightarrow G_\mu^a - \frac{1}{g_Q} \partial_\mu \alpha_a - f_{abc} \alpha_b G_\mu^c. \tag{2.16}$$

This finally gives us a gauge invariant kinetic energy term for all the  $G_\mu^a$  fields and thus we can write the QCD interactions as,

$$\mathcal{L}_{QCD} = \bar{q}(i\gamma^\mu \partial_\mu - m)q - g_Q (\bar{q}\gamma^\mu T_a q)G_\mu^a - \frac{1}{4} G_{\mu\nu}^a G_a^{\mu\nu}. \tag{2.17}$$

From the QCD Lagrangian Eqn. 2.17, we can see that it includes all of the same interactions we showed for QED, but also includes a  $SU(3)$  interaction due to the

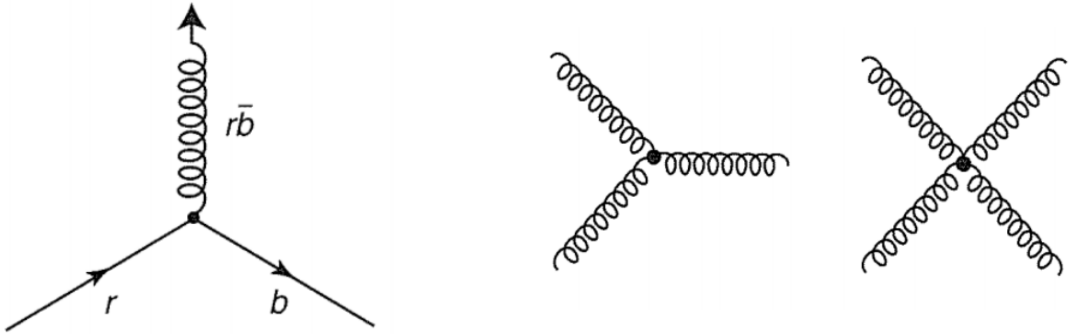


Figure 2.3 : The possible feynman diagrams in QCD where each vertex needs to conserve color chargel. Here is just an example of a red-blue vertex. QCD also includes a 3- and 4-vertex with gluons.

quark-gluon interactions with a certain color charge. However, QCD also included a 3- and 4-vertex interaction between the gluons, which arises due to the non-abelian nature of the force. From this, it is easy to tell that QCD is a much more complicated theory. We seem to be missing a vital part of the SM, specifically a theory for the Weakly interacting processes which is mediated by the massive bosons,  $W$  and  $Z$  from fig. 2.1.

### 2.1.6 Weak Force

The Weak force is responsible for nuclear decay. The Weak force has an interaction of the type  $\frac{1}{2}\gamma^\mu(1 - \gamma^5)$  so it is a  $V - A$  interaction with  $SU(2)$  symmetry. From this, we can conclude that it violates Parity. Parity is a transformation from  $(x, y, z) \rightarrow (-x, -y, -z)$  or space inversion. Since it violates Parity, the next step is to consider a conservation of  $CP$ , where  $C$  is charge conjugation (particle-to-antiparticle).

Now the Weak force is mediated by two vector bosons,  $W$  and  $Z$ , see fig. 2.1.

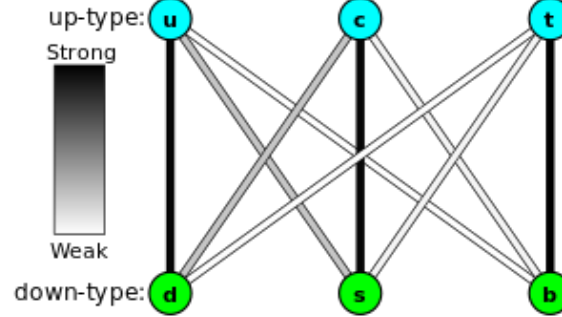


Figure 2.4 : A grammatical representation to show the couplings for Weak interactions, known as the Cabibbo-Kobayashi-Maskawa Matrix.

These are unlike the other forces because these vector bosons have a large mass of  $m_W = 80.379 \pm 0.012$  GeV and  $m_Z = 91.1876 \pm 0.0021$  GeV. The  $W$  boson is a charged particle and interacts with many nuclear decays.

The  $W$  boson interacts very interestingly for quarks in the SM. There is a mixing of flavors of quarks for particles. They will mix partners between up-type and down-type particles, see fig. 2.4. [Kobayashi, M. and Maskawa, K. (1973) Progress in Theoretical Physics, 49, 652]. The interactions for the generalized three generations of quarks is known as the Cabibbo-Kobayashi-Maskawa (CKM) matrix,

$$\begin{bmatrix} d' \\ s' \\ b' \end{bmatrix} = \begin{bmatrix} V_{ud} & V_{us} & V_{ub} \\ V_{cd} & V_{cs} & V_{cb} \\ V_{td} & V_{ts} & V_{tb} \end{bmatrix} \begin{bmatrix} d \\ s \\ b \end{bmatrix}, \quad (2.18)$$

where for example,  $V_{ud}$  is the coupling of  $u$  to  $d$  which is exactly ( $d \rightarrow u + W^-$ ). This matrix can be reduced to a form which has three generalized Cabibbo angles ( $\theta_{12}, \theta_{23}, \theta_{13}$ ) and a phase factor ( $\delta$ ). The coupling between the third generation does

not mix with the other two generations. From that we can recover the Cabibbo-GIM matrix[cite here]. For the moment, we can only determine these values from experimentation.

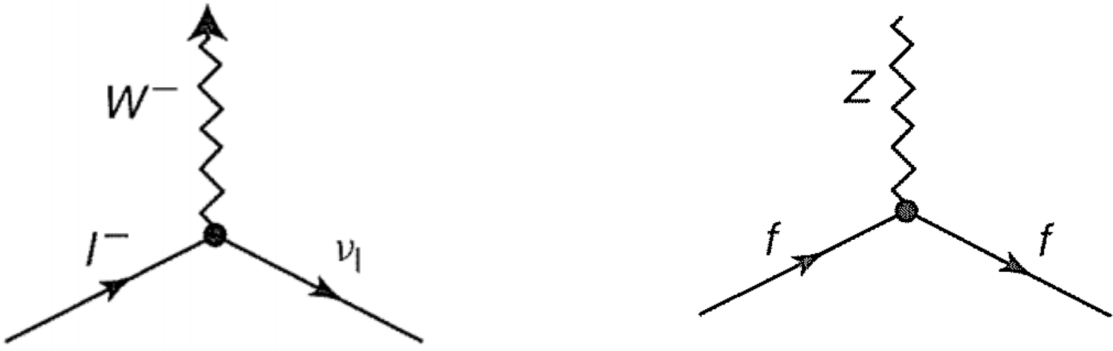


Figure 2.5 : Feynman diagram for Neutral Weak interaction and the charged weak current.

The  $Z$  boson is known as the neutral current. This boson mediates forces between particles and their respective antiparticles, see fig. ???. This interaction for the neutral weak force is  $\gamma^\mu(c_V^f - c_A^f\gamma^5)$  which is quite similar to the charged weak interaction, but differs by the constants  $c_V^f$  and  $c_A^f$ . The Weak interactions are shown in Fig. 2.5. We see the charged  $W$  boson interactions with the charged leptons and their respective neutrinos or allows for flavor changing interactions with quarks. Event though the neutral  $Z$  boson interacts with a  $V - A$  interaction we can still replace the  $\gamma$  in any QED Feynman diagram with a  $Z$ .

### 2.1.7 The Electroweak Lagrangian

The simplest group for the Electroweak interaction is  $SU(2)_L \times U(1)_Y$  which will give the left-handed interactions in doublets with the addition of massive gauge

bosons  $W$  and  $Z$  with a massless photon. We first consider the free Lagrangian,

$$\mathcal{L} = \bar{\psi}_j \gamma^\mu \psi_j, \quad (2.19)$$

where  $j$  is the fermion wave function. We are not including the mass parameter because it would cause the left and right-handed parts to mix. This is assumed to transform under the global invariant

$$\begin{aligned} \chi_L &\rightarrow \chi'_L = e^{i\frac{\tau_a}{2}\alpha^a(x) + i\beta(x)Y} \chi_L, \\ \psi_R &\rightarrow \psi'_R = e^{i\beta(x)Y} \psi_R \end{aligned} \quad (2.20)$$

where the transformation  $e^{i\frac{\tau_a}{2}\alpha^a(x)}$  with  $a = 1, 2, 3$  is the  $SU(2)_L$  transformation and only acts on the left-handed doublet. The next step is to require that the Lagrangian is invariant under local  $SU(2)_L \times U(1)_Y$ . We allow for the following covariant derivatives,

$$\begin{aligned} D_\mu \psi_1 &= [\partial_\mu - ig_W \frac{\tau_a}{2} W_\mu^a - ig'_W y_1 B_\mu] \psi_1 \\ D_\mu \psi_2 &= [\partial_\mu - ig'_W y_2 B_\mu] \psi_2 \\ D_\mu \psi_3 &= [\partial_\mu - ig'_W y_3 B_\mu] \psi_3 \end{aligned} \quad (2.21)$$

where  $g_W$  and  $g'_W$  are the Weak force coupling constants while  $W_\mu^a$  and  $B_\mu$  are four gauge bosons and can be the possible candidates for  $W^\pm$ ,  $Z$  and  $\gamma$ .

Just like the above descriptions the fields need to transform along with the wave

functions and derivatives. These transformations are,

$$\begin{aligned} B_\mu \rightarrow B'_\mu &= B_\mu + \frac{1}{g'_W} \partial_\mu \beta(x) \\ W_\mu \rightarrow W'_\mu &= U_L W_\mu U_L^\dagger - \frac{1}{g_W} \partial_\mu U_L U_L^\dagger \end{aligned} \quad (2.22)$$

where  $U_L = e^{i\frac{\tau_a}{2}\alpha^a(x)}$ . These transformation are similar to the QED and QCD transformation. If we include all of these invariant transformations in the free Weak Lagrangian Eqn. 2.19 and we get a free invariant Lagrangian, but this does not allow us to include a mass term for the fermions. Therefore this is not a viable procedure to include the Electroweak interactions into the model. In order to do this we must include the Higgs Mechanism.

### 2.1.8 The Higgs Mechanism

We are interested in the spontaneous symmetry breaking of a local  $SU(2)$  group. Specifically, the following Lagrangian,

$$\mathcal{L} = (\partial_\mu \phi)^\dagger (\partial^\mu \phi) - \mu^2 \phi^\dagger \phi - \lambda (\phi^\dagger \phi)^2, \quad (2.23)$$

with  $\phi$  being a  $SU(2)$  doublet of complex scalar fields,

$$\phi = \frac{1}{2} \begin{bmatrix} \phi_1 + i\phi_2 \\ \phi_3 + i\phi_4 \end{bmatrix} \quad (2.24)$$

and is invariant under global  $SU(2)$  phase transformations  $\phi \rightarrow e^{i\alpha_a \tau_a/2} \phi$ . To allow for local invariance, we first allow for a covariant derivative,

$$D_\mu = \partial_\mu + ig_W \frac{\tau_a}{2} W_\mu^a, \quad (2.25)$$

where we now have three gauge fields,  $W_\mu^a$ . If we assume an infinitesimal gauge transformation for the  $SU(2)$  doublet  $\phi(x) \rightarrow \phi'(x) = (1 + i\frac{\tau_a}{2}\alpha^a(x))\phi(x)$ , then the gauge fields will transform as,

$$W_\mu^a \rightarrow W_\mu^a - \frac{1}{g_W} \partial_\mu \alpha_a - f_{abc} \alpha_b W_\mu^c. \quad (2.26)$$

You can see that Eqn. 2.26 is similar to Eqn. 2.16 where we have replaced the QCD gauge field with the three gauge fields  $W_\mu^a$ . If we include these locally invariant transformations into the above  $SU(2)$  Lagrangian we get,

$$\mathcal{L} = (\partial_\mu \phi + ig_W \frac{1}{2} \tau_a W_\mu^a \phi)^\dagger (\partial^\mu \phi + ig_W \frac{1}{2} \tau_a W^{a\mu} \phi) - \mu^2 \phi^\dagger \phi + \lambda (\phi^\dagger \phi)^2 - \frac{1}{4} W_{\mu\nu}^a W^{a\mu\nu}, \quad (2.27)$$

where the gauge field kinetic term has been included at the end. The most interesting regions of this Lagrangian is when  $\mu^2 < 0$  and  $\lambda > 0$ , and the potential has a minimum at  $\phi^\dagger \phi = -\frac{\mu^2}{2\lambda}$ . With this we will expand the potential around the minimum and require that,

$$\phi_1 = \phi_2 = \phi_4 = 0, \phi_3^2 = -\frac{\mu^2}{2\lambda} \equiv v^2. \quad (2.28)$$

This is the spontaneous symmetry breaking of the  $SU(2)$  symmetry, because of this we are able to substitute an expansion for the field,

$$\phi = \sqrt{\frac{1}{2}} \begin{bmatrix} 0 \\ v + h(x) \end{bmatrix} \quad (2.29)$$

with this specific transformation of the  $SU(2)$  doublet and the simplification of Eqn. 2.27, the only remaining field is  $h(x)$  which is referred to as the Higgs field. This is what is known as the Higgs Mechanism for a  $SU(2)$  symmetry.

### 2.1.9 Electroweak

We want to include the Higgs Mechanism into the weak isospin and weak hypercharge,  $SU(2)_L \times U(1)_Y$ , transformations of electroweak interactions. Weak isospin and hypercharge is defined as  $I_3 = \frac{1}{2}(n_u - n_d)$  and  $Y \equiv B + S$ , respectfully, where  $n_u, n_d$  is the number of up or down quarks,  $B$  is the baryon number, and  $S$  is the strangeness. The weak isospin triplet for weak currents can be written down using Eqn. 2.27,

$$J_\mu^i(x) = \bar{\chi}_L \gamma_\mu \frac{1}{2} \tau_i \chi_L, \text{ with } i = 1, 2, 3. \quad (2.30)$$

Since this is a current we can calculate the charge by integrating of all of space,  $T^i = \int J_0^i(x) d^3x$ , which will give us the generators of the  $SU(2)_L$  symmetry  $[T^i, T^j] = i\epsilon_{ijk}T^k$ . Weak hypercharge,  $Y$ , is then defined by  $Q = T^3 + \frac{Y}{2}$  where  $Q$  is the charge and  $T^3$  is the third component of the weak isospin. The weak hypercharge is a conserved quantity of the  $U(1)_Y$  symmetry.

First, we need to include the coupling of the Weak current  $J_\mu^a$  and the gauge field  $W^{a\mu}$  such that,

$$-ig_W J_\mu^a W^{a\mu} = -ig_W \bar{\chi}_L \gamma_\mu T^a W^{a\mu} \chi_L \quad (2.31)$$

which is the basic interaction for the  $SU(2)_L$  symmetry. Then, we also need to include the weak hypercharge current with the fourth vector boson  $B^\mu$ ,

$$-i\frac{g'_W}{2} j_\mu^Y B^\mu = -ig'_W \bar{\psi} \gamma_\mu \frac{Y}{2} \psi B^\mu, \quad (2.32)$$

here the operators  $T^a$  and  $Y$  are generators for the  $SU(2)_L$  and  $U(1)_Y$  gauge transformations, respectively. Now we combine the two symmetries with the transformations of the left and right hand components of  $\psi$  and from this we can write down the contributions of the two gauge fields  $W_\mu^3$  and  $B_\mu$  and the missing angle  $\theta_W$  to find

the interactions of the two neutral currents. The physical fields are thus,

$$-ig_W J_\mu^3 W^{3\mu} - i \frac{g'_W}{2} j_\mu^Y B^\mu = -ie j_\mu^{em} A^\mu - \frac{ie}{\sin\theta_W \cos\theta_W} [J_\mu^3 - \sin^2\theta_W j_\mu^{em}] Z^\mu. \quad (2.33)$$

From this we can write down the Electroweak Lagrangian, for any fermion that interacts with the field. Moreover, we can formulate the Higgs mechanism, such that we can calculate the theoretical masses of the gauge bosons and fermions as,

$$\begin{aligned} M_W &= \frac{1}{2} v g_W \\ M_Z &= \frac{1}{2} v \sqrt{g_W^2 + g'_W^2}, \end{aligned} \quad (2.34)$$

but these masses cannot be predicted since they depend on the values from the chosen Higgs field.

### 2.1.10 The Standard Model Lagrangian

With the inclusion of the Higgs mechanism and the formulation of a local gauge invariant Lagrangian for the Electroweak and QCD fields, we have the complete SM Lagrangian as,

$$\begin{aligned} \mathcal{L} = & -\frac{1}{4} W_{\mu\nu}^a W^{a\mu\nu} - \frac{1}{4} B_{\mu\nu} B^{\mu\nu} - \frac{1}{4} G_{\mu\nu}^a G_a^{\mu\nu} \\ & + \bar{L} \gamma^\mu (i\partial_\mu - g_W \frac{1}{2} \tau^a W_\mu^a - g'_W \frac{Y}{2} B_\mu - g_Q T_b G_\mu^b) L \\ & + \bar{R} \gamma^\mu (i\partial_\mu - g'_W \frac{Y}{2} B_\mu - g_Q T_b G_\mu^b) R \\ & + |(i\partial_\mu - g_W \frac{1}{2} \tau^a W_\mu^a - g'_W \frac{Y}{2} B_\mu) \phi|^2 - V(\phi) \\ & - (G_1 \bar{L} \phi R + G_2 \bar{L} \phi_c R + \text{hermitian conjugate}), \end{aligned} \quad (2.35)$$

where the first terms are the kinetic energies and self-interactions of the  $W^\pm$ ,  $Z$ ,  $g$ , and  $\gamma$  bosons, the second and third terms are the kinetic energies and interactions of the leptons and quarks with the  $W^\pm$ ,  $Z$ ,  $g$ , and  $\gamma$  bosons where  $L$  is a left-handed fermion doublet and  $R$  is a right-handed fermion singlet. The fourth term is the  $W^\pm$ ,  $Z$ ,  $\gamma$  and Higgs masses and couplings. The final term is the lepton and quark masses and couplings to the Higgs field.

## 2.2 Fundamental Problems in the Standard Model

The SM is able to accurately and precisely describe many facets of the universe. Whether it comes to predicting the existence of a sixth quark or the confirmation of  $g - 2$  for the muon to 9 orders of magnitude. Unfortunately, there is some evidence of matter or interactions that cannot be described such as dark matter, the Hierarchy problem, and a possible grand unified theory. Let's look into each of these further.

### 2.2.1 Dark Matter

The main motivation for Dark Matter is the difference between the visible matter and the measurable matter in the universe. This has most notably been seen in the radial velocities of stars in galaxies. In a galaxy which is solely made up of visible matter, matter that interacts with light, the radial velocity of stars should decrease as  $1/\sqrt{r}$  the further away it is from the galactic nuclei, although measurements show the velocity becoming constant as a function of radius.

The original study of this was from the galaxy NGC 1560, where the measured galactic velocity curve provided a result that was 400 times large than the visible matter in the cluster (A. H. Broeils Astron. and Astrophys. 256 19 (1992)). To reproduce these features in models, the mass of the galaxy must be significantly

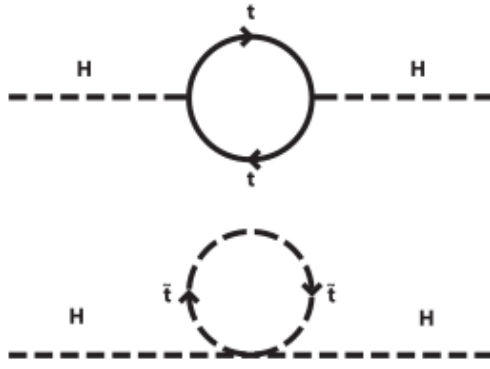


Figure 2.6 : The loop corrections to the Higgs boson interacting with a top quark and its superpartner the top squark. This is a next-to-leading order (NLO) correction to the Higgs boson mass.

more than what is seen. This implies some unseen dark matter, that still interacts with the gravitational field but not with the EM field. There is currently no such particle in the SM that has these properties.

### 2.2.2 Hierarchy Problem

The Higgs boson is a beautiful solution to electroweak symmetry breaking and gives a method for particles to acquire mass, see Sec. 2.1.8, and was discovered to have a measured mass of  $m_H = 125.18 \pm 0.16$  GeV [3]. This value though is not predictable with the SM and leads to some inconsistencies when you include loop corrections. Since the Higgs is strongly coupled to particles with large masses, the dominant loop correction is due to interactions with the  $t$  quark. These higher order loop corrections to the Higgs mass,  $m_H^2$ , caused by the fermionic  $t$  loop, see fig 2.6,

are,

$$\Delta m_H^2 = -\frac{|\lambda_t|^2}{8\pi^2} \Lambda_{UV}^2 + \dots, \quad (2.36)$$

where  $\lambda_f$  is the vertex factor for the respective fermion and  $\Lambda_{UV}$  is the ultraviolet momentum cutoff. The Higgs boson loop corrections are highly dependent on all virtual and real particles that couple to the Higgs field, we can see the corrections from Eqn. 2.36 from the  $t$  quark will cause a large divergence. The quadratic divergence of the Higgs mass is only renormalizable with a fine tuning of the parameters  $\lambda_f$  and  $\Lambda_{UV}$ .

This means the only way for the SM to reconcile this unfortunate fact is to have a relatively lucky cancellation of very large numbers of order  $10^{32}$  with equally small numbers. Fortunately, if we add the contribution of a bosonic partner of the fermion the Higgs loop corrections reduce to,

$$\Delta m_H^2 = \frac{\lambda_S}{16\pi^2} [\Lambda_{UV}^2 - 2m_S^2 \ln(\Lambda_{UV}/m_S) + \dots]. \quad (2.37)$$

With the introduction of a scalar partner to the  $t$ , there is a logarithmic divergence to the Higgs boson mass and can be renormalized through the normal methods.

### 2.2.3 Grand Unified Theory

The SM is able to accurately describe three of the fundamental sources at typical energy scales, 1 to  $10^4$  GeV, but ideally the forces would be able to merge into a single force at higher energies. This has not been directly observed, but many theories, such as supersymmetry (SUSY), predict its existence [4].

At standard energies for particle physics experiments the difference in the strength of each force is quite noticeable. But it has been shown that in the SM the strengths

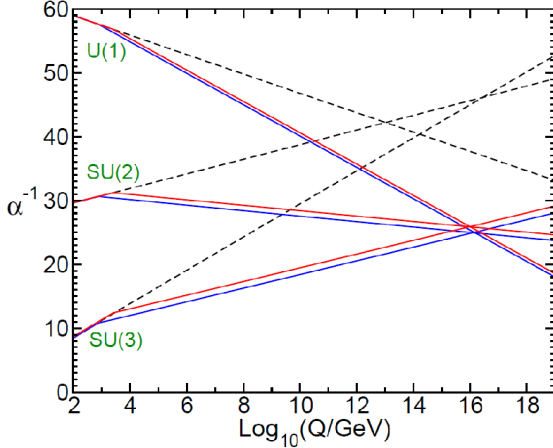


Figure 2.7 : The energy dependence of the inverse gauge couple of each force in the SM (dashed line) and the MSSM (solid lines). The MSSM gives two thresholds for the sparticle mass 750 GeV and 2.5 TeV.

of each force are dependent on the energy scale and it would be ideal that they converge to a single force at large energies, such as  $10^{16}$  GeV. In fig. 2.7, we see the extrapolated energy scales of the forces in the SM shown as the dotted line. These unfortunately, do not meet at a single point to become one force, but if we include supersymmetry into the model we get a nice convergence between the forces [4].

### 2.3 Supersymmetry

We have seen from the above three problems that there is still more to learn. Some of the features of the universe, such as; dark matter, the hierarchy problem, and a grand unified theory have not been explained. We saw from the Hierarchy problem that the addition of a bosonic partner to a fermion will allow for the loop corrections to be renormalizable without fine tuning. Fortunately, some theories have allowed for such a problem to be solved. Namely the theory of SUSY which essentially states

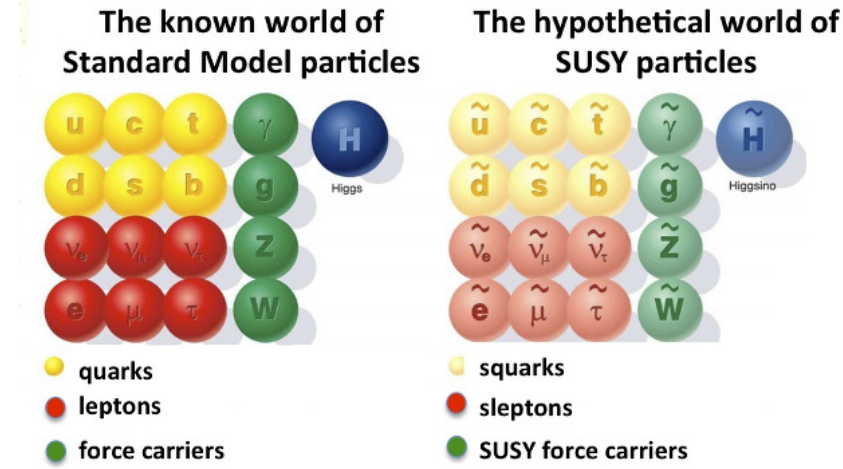


Figure 2.8 : The corresponding SUSY particles which are partners to the SM particles.

that each particle in the SM has a superpartner that has only the spin changed, that every fermion has a bosonic partner that has all the same quantum numbers except the spins differ by 1/2, and vice-versa.

The partners to the fermions are denoted with a 's' in front of the name to notify that it is the scalar form of the particle and the partners to the bosons have an 'ino' attached at the end, such as photino, gluino, wino, and Higgsino. So for the partners to the fermionic particles in the standard model we have: sup ( $\tilde{u}$ ), sdown ( $\tilde{d}$ ), scharm ( $\tilde{c}$ ), sstrange ( $\tilde{s}$ ), stop ( $\tilde{t}_1$ ), and sbottom ( $\tilde{b}$ ) for the squarks and selectron ( $\tilde{e}$ ), smuon ( $\tilde{\mu}$ ), and stau ( $\tilde{\tau}$ ) for the charged sleptons. The partners to the neutrinos, which are always left-handed if you neglect the minimal masses, are sneutrinos ( $\tilde{\nu}_e, \tilde{\nu}_\mu, \tilde{\nu}_\tau$ ), where we have one for each flavor of lepton, see Fig. 2.8.

If the SUSY was unbroken the superpartners would have exactly the same properties as the SM pairs except their spin. This would cause a massless photino or a

$m_{\tilde{e}} = 0.511$  keV selectron. These particles would certainly have been detected at this point, which leads us to think that SUSY is a broken symmetry where all the superpartners have a mass that is significantly higher than their SM partners.

### 2.3.1 Supermultiplets and Chirality

A supermultiplet is any symmetry where the number of bosonic degrees of freedom and fermionic degrees of freedom are equal,  $n_B = n_F$ . The simplest way to achieve this is to have a combination of a single Weyl fermion, which is a chiral representation of the fermion and has two spin helicity states,  $n_F = 2$ , and two real scalars with each having  $n_B = 1$ . It becomes convenient for the mathematics to combine the two real scalars into one complex scalar field. Now the combination of a complex scalar field and a Weyl fermion is known as a chiral supermultiplet.

### 2.3.2 Minimal Supersymmetric Standard Model

We have discussed how the fermions transform under the rules of SUSY, but how do the scalar field mediators translate into this new framework. First, lets look at the Higgs boson. We know that there is not only one chiral supermultiplet. If there was only one in the electroweak gauge symmetry, with a Higgsino of spin-1/2, would not have the anomaly cancellation of the traces,  $Tr[T_3^2 Y] \neq 0$  and  $Tr[Y^3] \neq 0$ , where  $T_3$  is the third component of weak isospin and  $Y$  is the weak hypercharge. In the SM, the traces of these for the fermions are already satisfied. So we must include two chiral supermultiplets of the Higgsino, with  $Y = \pm \frac{1}{2}$ , see table 2.2.

It turns out that this is also necessary for the Higgsino to give mass to different particles in the SM. A Higgs boson with  $Y = 1/2$  has the Yukawa couplings that allow it to interact with the up-type quarks ( $u, c, t$ ). Only a Higgs boson with  $Y = -1/2$

Names		spin 0	spin 1/2	$SU(3)_C, SU(2)_L, U(1)_Y$
squarks, quarks ( $\times 3$ families)	$Q$	$(\tilde{u}_L \ \tilde{d}_L)$	$(u_L \ d_L)$	$(\mathbf{3}, \mathbf{2}, \frac{1}{6})$
	$\bar{u}$	$\tilde{u}_R^*$	$u_R^\dagger$	$(\overline{\mathbf{3}}, \mathbf{1}, -\frac{2}{3})$
	$\bar{d}$	$\tilde{d}_R^*$	$d_R^\dagger$	$(\overline{\mathbf{3}}, \mathbf{1}, \frac{1}{3})$
sleptons, leptons ( $\times 3$ families)	$L$	$(\tilde{\nu} \ \tilde{e}_L)$	$(\nu \ e_L)$	$(\mathbf{1}, \mathbf{2}, -\frac{1}{2})$
	$\bar{e}$	$\tilde{e}_R^*$	$e_R^\dagger$	$(\mathbf{1}, \mathbf{1}, 1)$
Higgs, higgsinos	$H_u$	$(H_u^+ \ H_u^0)$	$(\tilde{H}_u^+ \ \tilde{H}_u^0)$	$(\mathbf{1}, \mathbf{2}, +\frac{1}{2})$
	$H_d$	$(H_d^0 \ H_d^-)$	$(\tilde{H}_d^0 \ \tilde{H}_d^-)$	$(\mathbf{1}, \mathbf{2}, -\frac{1}{2})$

Table 2.2 : The chiral supermultiplets of the MSSM. Spin-0 fields are complex scalars and spin-1/2 fields are left-handed two component Weyl fermions [4].

Names	spin 1/2	spin 1	$SU(3)_C, SU(2)_L, U(1)_Y$
gluino, gluon	$\tilde{g}$	$g$	$(\mathbf{8}, \mathbf{1}, 0)$
winos, W bosons	$\widetilde{W}^\pm \ \widetilde{W}^0$	$W^\pm \ W^0$	$(\mathbf{1}, \mathbf{3}, 0)$
bino, B boson	$\tilde{B}^0$	$B^0$	$(\mathbf{1}, \mathbf{1}, 0)$

Table 2.3 : The chiral supermultiplets of the MSSM [4].

has the correct Yukawa couplings to interact with the down-type quarks ( $d, s, b$ ) and the charged leptons ( $e, \mu, \tau$ ).

The SM vector boson will also have a corresponding chiral supermultiplet. They have fermionic superpartners that are referred to as gauginos. For the  $SU(3)_C$  color gauge interactions of QCD, which are a spin-1/2 color-octet, has a partner called a gluino ( $\tilde{g}$ ). The electroweak gauge theory  $SU(2)_L \times U(1)_Y$  has the superpartners  $\widetilde{W}^+, \widetilde{W}^0, \widetilde{W}^-$ , and  $\tilde{B}^0$  each with spin-1/2, called winos and bino, see table 2.3. The gaugino mixtures of  $\widetilde{W}^0$  and  $\tilde{B}^0$  give the corresponding zino ( $\tilde{Z}^0$ ) and photino ( $\tilde{\gamma}$ ). The chiral supermultiplets shown in table 2.2 and 2.3 give the particles of the Minimal Supersymmetric Standard Model (MSSM).

The five higgsinos and electroweak gauginos mix with each other because of electroweak symmetry breaking [4]. The neutral higgsinos ( $\tilde{H}_u^0$  and  $\tilde{H}_d^0$ ) and neutral gauginos ( $\tilde{B}$  and  $\tilde{W}^0$ ) mix into four mass eigenstates, which are called neutralinos,  $\tilde{\chi}_1^0, \tilde{\chi}_2^0, \tilde{\chi}_3^0$ , and  $\tilde{\chi}_4^0$ . The charged higgsinos ( $\tilde{H}_u^+$  and  $\tilde{H}_d^-$ ) and charged gauginos ( $\tilde{W}^+$  and  $\tilde{W}^-$ ) can mix into two mass eigenstates with charge  $\pm 1$  called charginos,  $\tilde{\chi}_1^\pm$  and  $\tilde{\chi}_2^\pm$ .

### 2.3.3 R Parity

$R$ -parity or matter parity is the multiplicatively conserved quantum number defined as,

$$P_R = (-1)^{3(B-L)+2s}, \quad (2.38)$$

where  $B$  is the baryon number,  $L$  is the lepton number, and  $s$  is the spin of the particle. From this we can find the  $R$ -parity of all the particles in the SM and MSSM. The definition of  $R$ -parity is quite useful because all the particles of the SM have an  $R$ -parity of  $P_R = +1$ , while all of the squarks, sleptons, gauginos, and higgsinos have  $P_R = -1$ .

$R$ -parity is thought to be exactly conserved in SUSY, where there is no mixing between particles ( $P_R = +1$ ) and sparticles ( $P_R = -1$ ). This leads to three important consequences:

- The lightest sparticle that has  $P_R = -1$  is called the "lightest supersymmetric particle" or LSP, which must be absolutely stable. If it is electrically neutral, it is a possible non-baryonic dark matter candidate.
- Every sparticle, other than the LSP, must eventually decay into an odd number of LSPs.

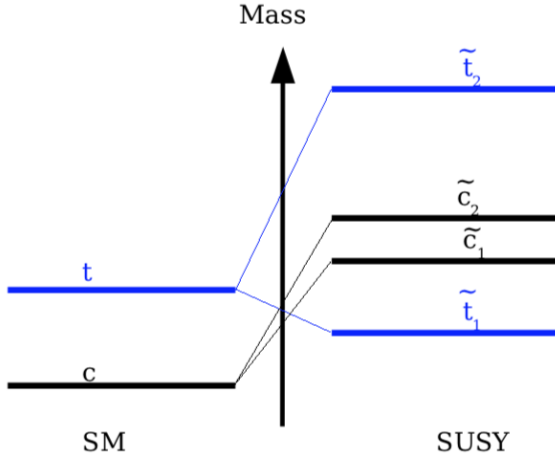


Figure 2.9 : On the right we have the arbitrary masses of the top and charm quarks. The left and right handed states mix into two mass eigenstates. It is possible that the top squark will have the smallest mass of the squarks.

- For collider experiments, sparticles will only be produced in even numbers.

We are going to be investigating a MSSM that conserves  $R$ -parity. This is quite well motivated by the possibility of a dark matter candidate.

### 2.3.4 Mass Spectrums

The third family of squarks and sleptons should have quite different masses compared to their first- and second-family counterparts, which is caused by the large Yukawa ( $y_t, y_b, y_\tau$ ) and soft ( $a_t, a_b, a_\tau$ ) couplings, which are holomorphic parameters proportional to the Yukawa couplings. This causes significant mixing between the chiral superpartners  $(\tilde{t}_L, \tilde{t}_R), (\tilde{b}_L, \tilde{b}_R)$ , and  $(\tilde{\tau}_L, \tilde{\tau}_R)$ . We will concentrate on how the mass of the top squark,  $\tilde{t}_1$  evolves in the MSSM. Given many contributions to the top squark mass such as; squared-mass terms, 4-vertex interactions terms with the up-type Higgs, the 3-vertex interactions with the down-type Higgs, and scalar potential

couplings. We have a square-mass matrix for the top squarks,

$$\mathcal{L}_{\text{stop masses}} = - \begin{bmatrix} \tilde{t}_{1L}^* & \tilde{t}_{1R}^* \end{bmatrix} \mathbf{m}_{\tilde{t}_1}^2 \begin{bmatrix} \tilde{t}_{1L} \\ \tilde{t}_{1R} \end{bmatrix} \quad (2.39)$$

where

$$\mathbf{m}_{\tilde{t}_1}^2 = \begin{bmatrix} m_{Q_3}^2 + m_t^2 + (\frac{1}{2} - \frac{2}{3}\sin^2\theta_W)\cos(2\beta)m_Z^2 & v(a_t^*\sin\beta - \mu y_t\cos\beta) \\ v(a_t\sin\beta - \mu^* y_t\cos\beta) & m_{\tilde{u}_3}^2 + m_t^2 + (\frac{2}{3}\sin^2\theta_W)\cos(2\beta)m_Z^2 \end{bmatrix}. \quad (2.40)$$

This is a hermitian matrix and can be diagonalized to give eigenstates  $\tilde{t}_1$  and  $\tilde{t}_2$  which are linear combinations of the left and right-handed  $\tilde{t}_1$ , see fig. 2.9. Now we get the eigenvalues for the mass states as  $m_{\tilde{t}_1}^2 < m_{\tilde{t}_2}^2$ . From this models predict that the  $\tilde{t}_1$  is the lightest squark [4].

### 2.3.5 Supersymmetry Searches

The SM of particle physics has been a powerful model for predicting interactions between quarks, leptons, and force carriers, with an accurate prediction for precision measurements, but has some faults such as, the Hierarchy problem, dark matter, and a Grand Unified Theory. We have seen that including SUSY can allow for possible solutions, such as: a dark matter candidate as the LSP, bosonic-fermionic loop corrections for the Higgs boson mass, and a unification of the fundamental forces at large energies. Then once investigating the theory of SUSY we were able to determine that the top squark could be the lightest squark, which allows us to develop multiple searches for this proposed theory.

## 2.4 Current SUSY Results

Here we see the most current results from searches for the top squark. These have been completed with data from the first part of Run 2 with  $35.9 \text{ fb}^{-1}$ . This analysis was completed with the most up-to-date identification methods for particles in the SM. From this Analysis, all 104 search region bins, as well as the corresponding single-lepton control region bins, the  $\gamma+\text{jets}$  control region bins and the QCD control regions, are fit simultaneously in order to evaluate the cross section excluded at 95% confidence level for each signal benchmark point.

The easiest way to think about the plots shown in 2.10, 2.11, 2.12, 2.13, 2.14, is that there is a calculated limit for each mass point. The  $x$ -axis is the possible mass range for the  $\tilde{t}_1$ ,  $m_{\tilde{t}_1}$  and the  $y$ -axis is the possible range for the  $\tilde{\chi}_1^0$ ,  $m_{\tilde{\chi}_1^0}$ . Each point in this 2D space has a color representation for the value of the upper limit on the cross section at a confidence level of 95%.

With the comprehensive analysis that was performed in 2016, we have various limits on the multiple decay modes of the  $\tilde{t}_1$  which will be covered completely in Section 5. The comprehensive limits on the  $\tilde{t}_1$  mass range from values of 550 to 1.1 TeV for all of the all-hadronic decay modes. The CMS Collaboration has also combined the limits from the separate analyses which concentrate on the 1-lep, 2-lep, MT2, and HT missing analyses. The combination of these has shown that we can set limits on the  $\tilde{t}_1$  mass range for masses of 800 to 1100 GeV.

From the Fig. 2.10, 2.11, 2.12, 2.13, 2.14, and 2.15, we know that we are able to exclude a large mass range for the  $\tilde{t}_1$  and  $\tilde{\chi}_1^0$ . Since this is one for a luminosity of  $36.8 \text{ fb}^{-1}$ , we can expect improved limits with all of the data from Run 2, which is  $137 \text{ fb}^{-1}$ . The new version of the analysis also has a redesigned search region to allow for more sensitive results, while also improving various object definitions.

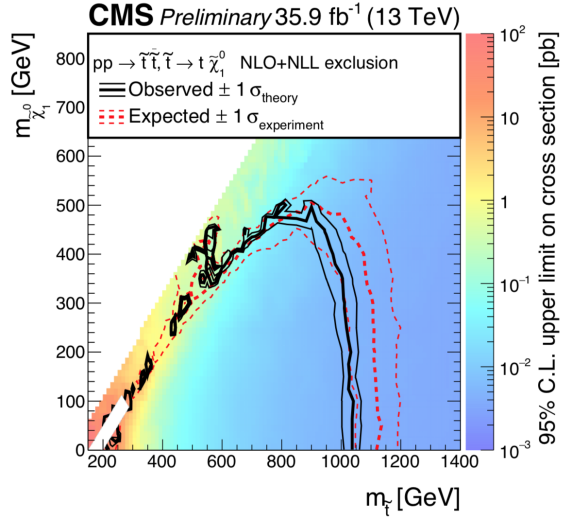


Figure 2.10 : Limits for the mass parameter space for T2tt decays. With a current limit of 1.1 TeV for a minimal neutralino mass.

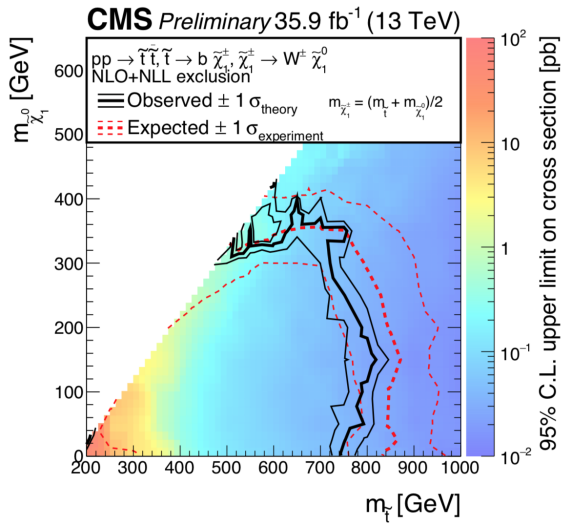


Figure 2.11 : Limits for the mass parameter space for T2bW decays. With a current limit of 750 GeV for a minimal neutralino mass.

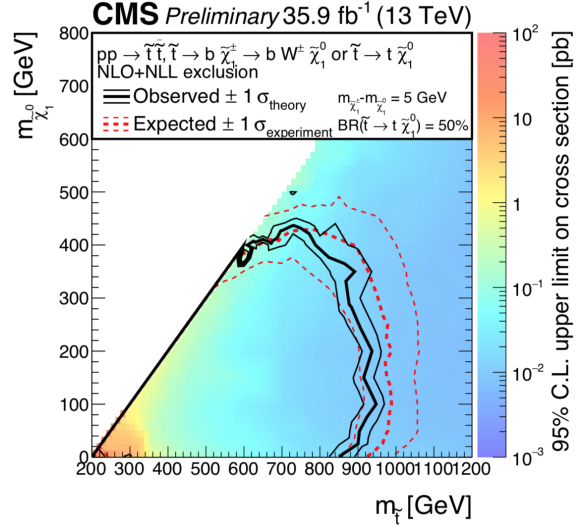


Figure 2.12 : Limits for the mass parameter space for T2tb decays. With a current limit of 850 GeV for a minimal neutralino mass.

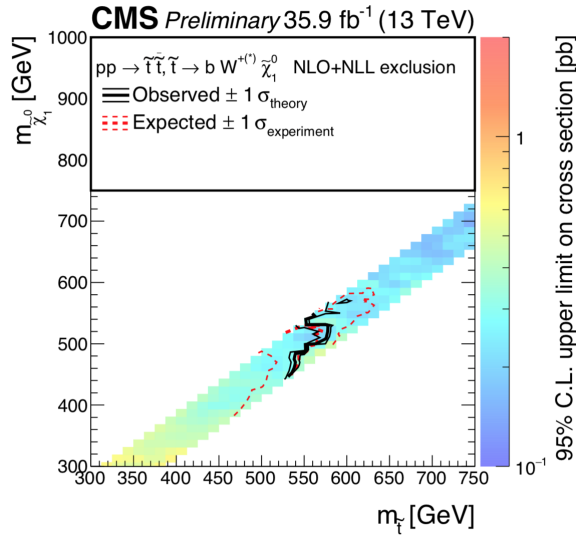


Figure 2.13 : Limits for the mass parameter space for T2fbd decays. Which has a range of 550 GeV for a  $\tilde{\chi}_1^0$  mass of approx. 500 GeV.

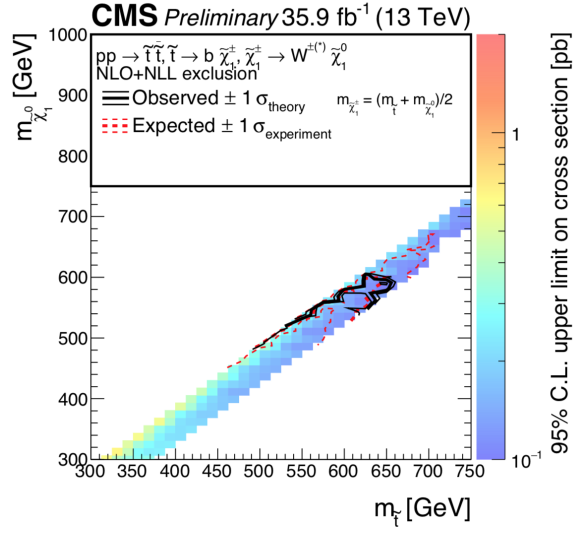


Figure 2.14 : Limits for the mass parameter space for T2bWC decays. Which has a range of 550 to 675 GeV for a  $\tilde{\chi}_1^0$  mass of 600 GeV.

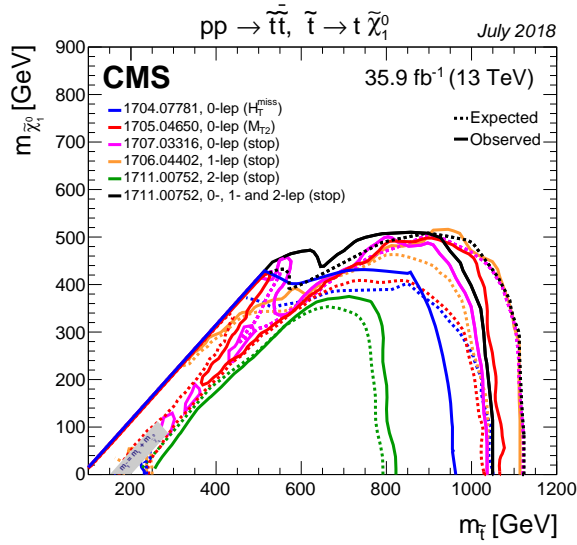


Figure 2.15 : Limits for the mass parameter space for T2tt decays using results from all the analysis in CMS. With a current limit of 800 GeV to 1.1 TeV for a minimal neutralino mass.

## 2.5 What are we looking for? And why?

As discussed in Sec. 2.1, the SM is a robust theory that is useful for describing the iterations of visable matter in the universe. It has been through many robust test, while also able to make many predictions. Unfortunately, we have seen that a few unknowns such as, dark matter, the hierarchy problem, and a possible GUT, are currently unexplained. We then showed that a possible solution to these is SUSY, Sec. 2.3, provides a good dark matter candidate, LSP, allows for the convergence of the EM, Weak, and Strong force at large energy scales, and allows the Higgs mass to be renormalizable without fine tuning.

From this, we have determined that the top squark is most likely to have the smallest squark mass in the MSSM. There has been many searches for the top squark decaying to many modes which are summarized in Fig. 2.15. As of right now we have set a limit on the  $\tilde{t}_1$  mass,  $m_{\tilde{t}_1} > 800$  GeV or  $m_{\tilde{t}_1} > 1100$  GeV depending on the analysis. Now we plan on using all of the data from Run2,  $137 \text{ fb}^{-1}$ , along with an improved search design to probe further into the mass parameter space of the  $\tilde{t}_1$  and  $\tilde{\chi}_1^0$ .

## Chapter 3

### Compact Muon Solenoid

#### 3.1 The Detector

The Compact Muon Solenoid (CMS) is a particle detector as part of the Large Hadron Collider (LHC) which is located near Geneva, Switzerland as part of the CERN collaboration. The CMS detector is 21.6 m long, 15 m diameter, and 14,000 tons and is used to detect many different species of particles. It is separated into layers that, from the interaction vertex outward are, the silicon tracker, Electromagnetic Calorimeter (ECAL), Hadronic Calorimeter (HCAL), superconducting solenoid, and the muon chambers, see Fig. 3.1.

The CMS detector is designed to detect the decay products of most of the particles of the SM, except for neutrinos since they are weakly interacting and will almost certainly pass through the entire earth without an interaction. A defining feature of CMS is the 12.6-m long, 5.9 m inner diameter, 3.8 T superconducting solenoid. This is used to bend the trajectory of charged particles throughout the detector, such that we can reconstruct the momentum and charge of the particles. The LHC provides a 13 TeV proton-proton beam (4.5 TeV heavy ion) beam with a bunch crossing every 25 ns (50 ns) to produce interaction at luminosities up to  $2.5 \times 10^{34} \text{ cm}^{-2} \text{ s}^{-1}$ .

The coordinate system of CMS has the origin at the nominal collision point in the center of the detector. The  $y$ -axis points vertically upward,  $x$ -axis points radially inward toward the center of the LHC, and  $z$ -axis points along the beam directions

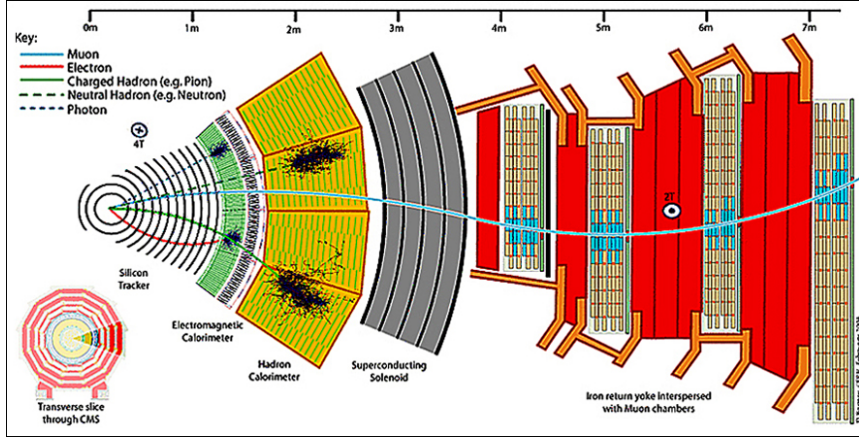


Figure 3.1 : A cross-section of the CMS detector, oriented by looking down the direction of the beam pipe.

towards the Jura mountains from LHC Point 5. The polar angle  $\theta$  is measured from the  $z$ -axis and the azimuthal angle  $\phi$  is measured in the  $x - y$  plane from the  $x$ -axis. The pseudorapidity of a particle is defined as  $\eta = -\ln \tan(\theta/2)$  where  $\theta$  is the angle between the particle momentum and the positive direction of the beam axis, two notable values are  $\eta = 0$  at  $\theta = \pi/2$  and  $\eta = \inf$  at  $\theta = 0$ . Pseudorapidity is quite useful since the difference of pseudorapidities is Lorentz invariant. The transverse components of momentum,  $p_T$ , and energy,  $E_T$ , are computed using the  $x$  and  $y$  components of the particles.

### 3.1.1 Tracker

The silicon tracker is made up of two different detectors, the silicon pixels and the silicon strip tracker. This is the inner most detector for CMS and receives the largest flux of particles during operation. This requires it to be radiation hard and operate with a fine granularity.

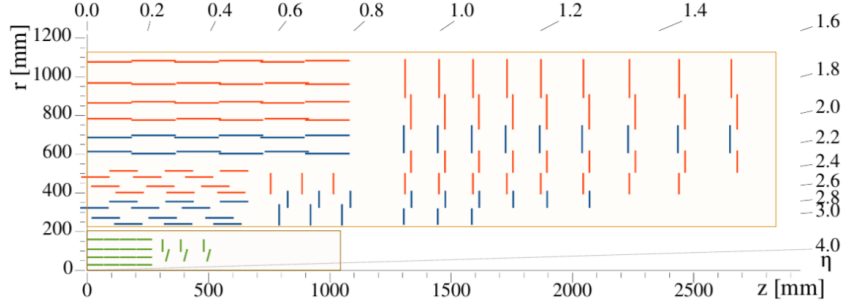


Figure 3.2 : Geometry of the CMS Tracker, the inner most region in green is the pixel detector while the outer region in blue and red are the silicon strips.

### 3.1.1.1 Pixel Detector

The pixel detector was recently upgraded during the winter of 2016/2017. It is approximately 1 m long with four barrel layers ranging from 3.0, 6.8, 10.2, and 16.0 cm from the beam axis and three endcap disks, see fig. 3.2. Since it is the closest detector to the interaction vertex it therefore has the highest particle flux at  $10^7/\text{cm}^2/\text{s}$  at  $r = 10$  cm. The resolution is  $9.4\ \mu\text{m}$  in  $r - \phi$  and  $20 - 45\ \mu\text{m}$  in  $z$ .

The pixel detector contains 1,184 modules in the barrel pixels (BPIX) and 672 modules in the forward pixels (FPIX). The number of individual pixels is 79 (45) million in the BPIX (FPIX) regions, respectively, with a pixel size of  $100 \times 150\ \mu\text{m}^2$ . A pixel module contains two layers, a silicon layer that is bump bonded to 16 Readout Chips (ROCs) which form a module of 66560 pixels, see fig. 3.3. Each unit is controlled with one or more Token Bit Managers (TBMs) which controls the readout of the digital signal from the pixels to the Front-end Driver (FED). For BPIX Layers 3, 4 and all of FPIX there is 1 TBM per module. BPIX layer 2 has 2 TBMs with each one controlling 8 ROCs, while BPIX layer 1 has 4 TBMs with each one controlling 4 ROCs. The information from each module is split into two channels with each

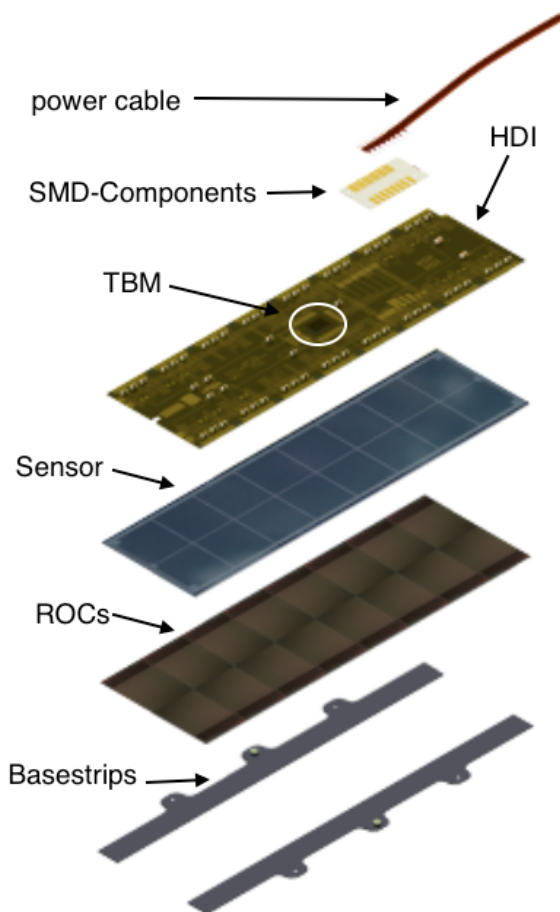


Figure 3.3 : Components of the pixel modules. Made up of a silicon layer, a grid of 8 ROCs which are attached via bump bonds. This is all controlled with a TBM connection to read out data.

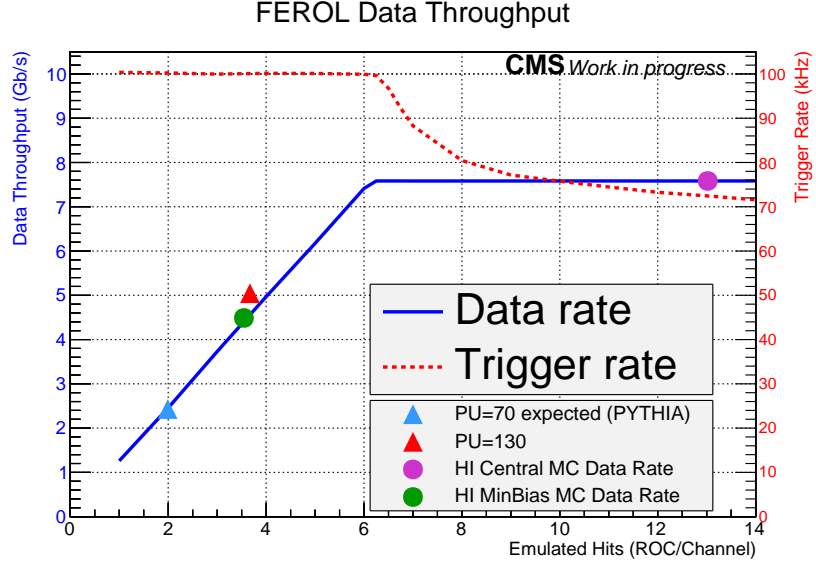


Figure 3.4 : Measuring the throughput of the FED with the emulated and simulated events provided by the FED Tester. The Data rate is shown as the solid blue line with the corresponding trigger rate as the dotted red line. The simulated event sizes are shown as their equivalent emulated hits/ROC/channel on the data line.

containing 8, 4, or 2 ROCs. These are encoded together by the TBM before being sent to the FED.

The silicon pixel system is set up as a reverse p-n junction, where the pixels are in the n-type region. As a charged particle travels through the silicon it creates electron-hole pairs. A voltage difference is applied to the silicon such that the electrons will deposit onto the pixels. Since the detector is inside of the magnetic field, a Lorentz drift will cause the electrons to reach more than one pixel and increase the resolution. As the pixel system continues to be irradiated with large quantities of particles the voltage in the silicon decreases. This will lead to less charge sharing between the pixels and a decrease in resolution of particle locations.

The data, from the pixels, is sent via optical fiber to the FED where is decoded

and processes the information. The FED is responsible for identifying the relevant data, determining possible error states, and packaging the information to be sent to the central Data Acquisition (cDAQ) of CMS. Each of the 108 FEDs, for the pixels, receives 24 independent fibers from the detector. Each of these fibers contains 2 channels from the pixel module. Through robust testing with the FED Tester [Cite here], we have confirmed that the FED is able to attain a maximum data throughput of approximately 7.5 Gbps, see fig. 3.4.

### 3.1.1.2 Silicon Strips

The silicon strips have a  $200 \text{ m}^2$  active region with 15,148 modules that are distributed in 10 barrel layers and 9 + 3 endcap disks. This has a cell size ranging from  $10 \text{ cm} \times 80 \mu\text{m}$  to  $25 \text{ cm} \times 180 \mu\text{m}$  since the particle flux decreases further away from the vertex, Fig. 3.5. It has a resolution of  $23 - 24 \mu\text{m}$  in  $r - \phi$  and  $23 \mu\text{m}$  in  $z$  for the microstrip tracker.

There are two types of silicon strip module, see Fig. 3.5, which are in the layers shown in Fig. 3.2. The orange modules are single sided reverse p-n silicon sensors, while the blue modules are double sided by having two single modules mounted back-to-back at a 100 mrad angle. This improves the 3D tracking, but unlike the pixel detector this is an analog readout system.

### 3.1.2 Electromagnetic Calorimeter

The ECAL is a homogeneous calorimeter made out of 61,200 lead tungstate ( $\text{PbWO}_4$ ) crystals in the barrel and 7,324 crystals in each endcap. The barrel region has an inner radius of 129 cm and covers a pseudorapidity range of  $0 < |\eta| < 1.479$ . The encap are 314 cm from the interaction point and cover a range  $1.479 < |\eta| < 3.0$

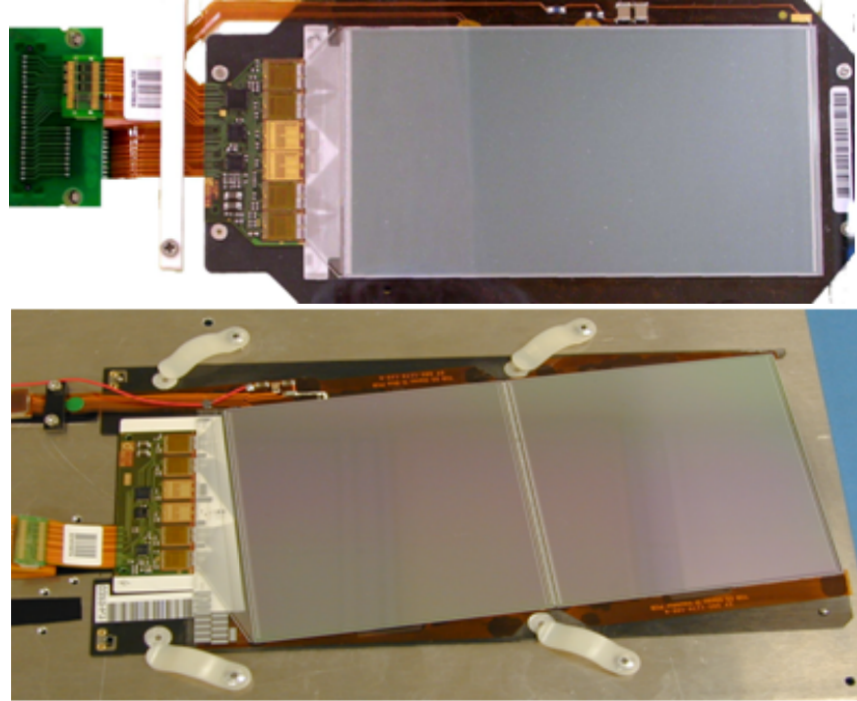


Figure 3.5 : The top module is a single sided reverse p-n silicon sensor. The bottom is two silicon sensors mounted back-to-back at a 100 mrad angle.

in pseudorapidity. Lead tungstate was chosen for the crystals since it has a short radiation length,  $X_0 = 0.89$  cm , fast with 80% of the light being emitted within 25 ns, and it's radiation hard. Each crystal in the barrel has a cross-section of  $\approx 22 \times 22$  mm<sup>2</sup> and length of 230 mm, while the endcap crystals are  $28.6 \times 28.6$  mm<sup>2</sup> and length of 220 mm corresponding to  $25.8X_0$  and  $24.7X_0$ , respectively. An ECAL uses electromagnetic showers to detect particles that interact electromagnetically. Electrons travelling through the material will radiate a photon via bremsstrahlung then the photon will pair produce two electrons. Combining these two processes leads to electromagnetic showers as the particles travel through the detector. The process will continue until a critical energy is reached such that an electron cannot

radiate any further and will then lose energy via collisions. The hadrons that are created in the collisions will also interact in this way, but because of their large mass they penetrate through the entire ECAL. The resulting light is recorded by silicon avalanche photodiode (vacuum phototriodes) in the barrel (endcap).

### 3.1.3 Hadronic Calorimeter

The HCAL is a hermetic calorimeter consisting of alternating layers of brass as the absorber material and a scintillator. Brass is chosen since it is non-magnetic and has a relatively short interaction length. In the scintillator, a portion of the energy from the hadron is converted into visible light which is then measured by a hybrid photodiode tube to measure the energy. The barrel part of the HCAL consists of 2304 towers that are segmented into  $\Delta\eta \times \Delta\phi = 0.087 \times 0.087$  pieces that cover a region  $0 < |\eta| < 1.4$  in pseudorapidity. The endcap region consists of 2304 towers with varying segmentation sizes and a coverage of  $1.3 < |\eta| < 3.0$ .

There are two additional parts of the HCAL to allow for maximum coverage of the detector volume. There is an outer hadron detector that is located outside the superconducting solenoid, which covers a slightly smaller pseudorapidity range as the barrel region. They serve as a tail catcher for hadron showers that penetrate all the way through the inner HCAL and solenoid. A forward hadron calorimeter, located 11.2 m from the interaction point covering a pseudorapidity  $3.0 < \eta < 5.0$ , made out of steel/quartz fiber is specifically designed for the columnated Cerenkov light in this region.

### 3.1.4 Superconducting solenoid

Surrounding most of this is the superconducting solenoid which is 12.6 m long with a 5.9 m radius. The field strength is 3.8 T which has a stored energy of approximately 2.7 GJ. The magnet is designed such that a muon with momentum,  $p = 1 \text{ TeV}$ , will have a momentum resolution of  $\Delta p/p \approx 10\%$ . The solenoid is a high-purity aluminium-stabilized conductor, which is a similar material used in other large solenoids.

### 3.1.5 Muon Chambers

The muon system has three main detection systems that are used to identify a muon candidate. In the barrel region, drift tube (DT) chambers are used since the neutron background, muon rate, and magnetic field are all small. In the endcaps, cathode strip chambers (CSCs) are used since the relative values stated before are much larger. The neutron background is largely radially dependent so the CSCs will receive a larger flux, while the muon rate is dominated by low  $p_T$  muons which will interact in the endcap regions. Included throughout the whole system are resistive plate chambers (RPC).

The DT consists on 250 chambers in 4 barrel layers at a radii of 4.0, 4.9, 5.9, and 7.0 m from the beam axis. A DT chamber is an array of anode wires in a gaseous medium where the walls are cathodes. A muon passing through the gas will ionize some atoms which are then forced towards the anode wires by the electric field. The drift time of the electrons can then be calculated to within a couple of ns such that a good spatial resolution is achieved. The maximum designed drift length is 2.0 cm. Each station of the DT will give muon vector for each candidate with a  $\phi$  precision of  $100 \mu\text{m}$  in position and 1 mrad in direction.

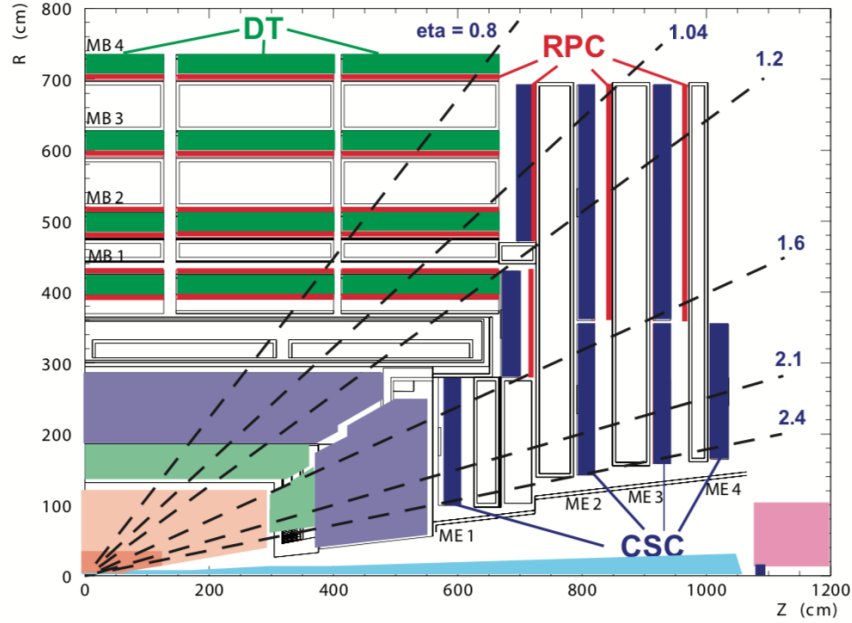


Figure 3.6 : A quarter cross-section of the three muon detection systems for CMS.

The CSC system uses the same concept as the DT system, but also includes a measurement of the ions that follow the electric field to the cathode strips. In this system the anode wires and the cathode strips are perpendicular so the collected charge on both provide an accurate position measurement. The RPC system contains two parallel plates, anode and cathode, the charge is measured by external metallic strips that can quickly measure the momentum of a muon and decide if the event should be triggered.

### 3.2 Detector Methods

Using the objects and information from each of the subdetectors we can measure the important information required for doing innovative physics analysis, such as,

the  $\tilde{t}_1$  search. Since the search is dependent on large missing energies it is dependent on measuring all forms of energy in the standard model and checking for any inefficiencies. The CMS detector is designed to be an all encompassing detector to measure multiple processes in the SM and beyond.

# Chapter 4

## Search Strategy

### 4.1 Physics Objects

There are many different types of physics objects that we are interested in when working with particle physics experiments. Since these particles have very short lifetimes,  $\mathcal{O}(\text{decay}) = 10^{-23}$  s, we mainly interact with the decay products of the event, such as, jets ( $N_j$ ), heavy object tagging ( $N_b, N_t, N_W, N_{res}$ ), missing transverse momentum ( $\cancel{E}_T$ ), scalar sum jet momentum ( $H_T$ ), soft-b tagging, denoted as  $N_{sv}$ , transverse mass between tagged  $b$  quarks and  $\cancel{E}_T$  ( $m_T(b_{1,2}, \cancel{E}_T)$ ), Initial State Radiation, and lepton identification. We will look into each of these objects further in this chapter.

#### 4.1.1 Jets

In an interaction whenever a quark is made it comes in pairs ( $q\bar{q}$ ) such that the total color charge of the interaction is neutral. Typically due to conservation of momentum the quarks may originally be produced near the interaction point but will quickly start to move away from each other. Eventually the quarks will move far enough apart and will have enough potential energy in the gluon connections between them that it is now more efficient to create a new quark-antiquark ( $q\bar{q}$ ) pair. This will continue to occur in a sequence of radiating gluons and producing new pairs of charged particles, see fig. 4.1. In the final state, the energy deposited in the

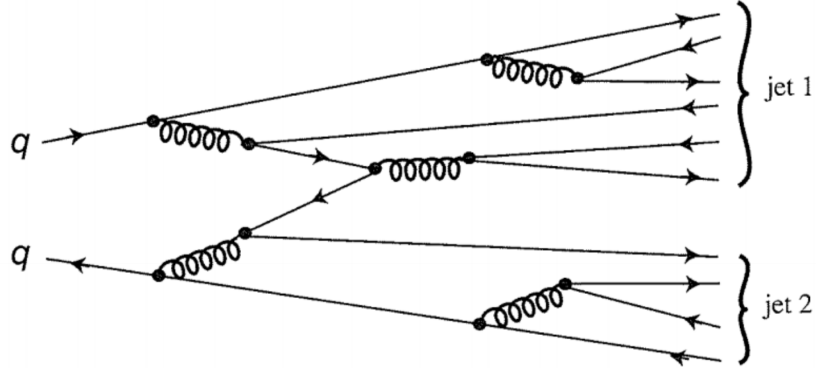


Figure 4.1 : A diagram of a quark pair radiating gluons that decay into more quark pairs in a process called hadronization [8].

HCAL is a cluster of charged particles of a radius,  $\Delta R = \sqrt{\Delta\eta^2 + \Delta\phi^2}$ . There are many algorithms to reconstruct the jets, we are mainly interested in the anti-kT Jet algorithm [5] method which uses the transverse momentum of the particles within a certain radius  $\Delta R = 0.4(0.8)$  for AK4(AK8) jets [6, 7]. Once the jets have been identified, we can analyze their respective properties to determine the likelihood of the particle it originated from, such as a  $b, t$ , or  $W$ .

#### 4.1.2 Heavy Object Tagging

Since this search is looking for a massive particle which then decays to slightly less massive particles we need to be able to identify and distinguish between them. We use various algorithms and neural networks to identify jets from  $b$  quarks,  $t$  quarks, or from  $W$  bosons.

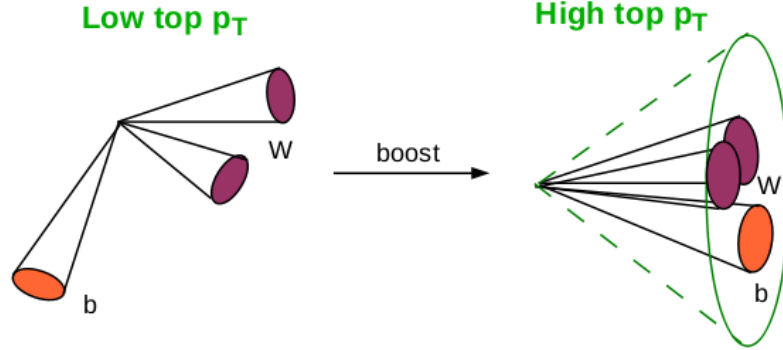


Figure 4.2 : The two types of top quark reconstructions, when each decay product is easily identifiable (resolved) or when the particles are close together (boosted).

#### 4.1.2.1 B-Tagging

Firstly,  $b$ -tagged jets which are jets that are likely to have originated from a  $b$  quark. For  $b$  quarks with large transverse momentum, we use a Deep Combined Secondary Vertex (DeepCSV) algorithm that involves neural networks [9]. The medium working point recommended by the B-tag POG, corresponding to a threshold of 0.6324, 0.4941, and 0.4184 for the 2016, 2017, and 2018 respectively [10–12]. The medium working point is defined such that the percentage of a light jet being misidentified as a  $b$  – jet is 1%.

#### 4.1.2.2 Top/W Tagging

The anti- $\text{kt}$  algorithm using a distance parameter,  $\Delta R = 0.8$ , is expected to contain the energy clusters of all of the decay products of boosted  $t$  quarks, see Fig. 4.2, with  $p_T > 300 \text{ GeV}$  or  $W$  bosons with  $p_T > 200 \text{ GeV}$ . The requirements are:

- Medium working point  $> 0.937, 0.895, 0.895(0.973, 0.991, 0.991)$  for boosted  $t$  ( $W$ ) for the separate 2016, 2017, and 2018 eras, respectively.

- Reconstructed soft drop [13] mass:  $105 < m_t < 210$  GeV and  $65 < m_W < 105$  GeV.
- Boosted tops:  $p_T = 300$  GeV,  $|\eta| < 2.0$  and  $W$ :  $p_T = 200$  GeV,  $|\eta| < 2.0$

There is another type of top that can be reconstructed, which is when each subjet of the top decay can be resolved into each individual jet, denoted as a resolved top, see Fig. 4.2. The requirements are:

- Medium working point: 0.92 for all eras.
- $|\eta(j_{1,2,3})| < 2.4$  and  $b$ -tag discriminator:  $> 0.6324, 0.4941, 0.4184$  for the separate 2016, 2017, and 2018 eras, respectively. The number of jets in the event that pass these cuts should be  $\geq 2$ .

These object definitions,  $N_t$ ,  $N_W$ ,  $N_{res}$ , are orthogonal to each other and are used to bin our search and control regions.

#### 4.1.3 Missing Transverse Momentum

The missing transverse momentum is the negative vector sum of the total transverse momentum measured in the detector,

$$\cancel{E}_T = - \sum_{i \in \text{vis}} \vec{p}_{i,T}, \quad (4.1)$$

where the momentum runs over every visible(vis) particle in the event. Ideally, if the detector was 100% efficient this quantity would always be zero due to conservation of momentum, but many things, such as detector efficiency, particles that are weakly interacting, or particles beyond the SM will cause the missing energy. Because of these, this object is a good discriminator for searching for physics beyond the SM.

#### 4.1.4 $H_T$

Another interesting quantity is  $H_T$ , which is the scalar sum of the  $p_T$  of all of the jets in an event,

$$H_T = \sum_{i \in \text{jets}} p_{i,T}. \quad (4.2)$$

This quantity is quite useful when trying to identify massive particles and is quite good at suppressing QCD multijet background.

#### 4.1.5 Soft $b$ -Tagging

The ability to identify secondary vertices is essential in searches for the top squark, see Sec. 5.1. Since the  $b$  quark is a long lived particle, about  $10^{-12}$  seconds, that will travel many millimeters before decaying into other particles. A  $b$  quark is identified during reconstruction, where the jet originating from a point separated from the primary vertex ( $PV$ ), known as the secondary vertex ( $SV$ ). The displaced vertex of the long lived  $b$  quark with low  $p_T$  has many interesting kinematic properties that we can use to identify them, known as soft  $b$ -tagging.

Since this search also targets models that produce very soft bottom or charm quarks. A large fraction of events contain  $b$  quarks with  $p_T$  below the 20 GeV jet threshold which may thus fail to be reconstructed as jets or become  $b$ -tagged. Identification of these soft quarks improves our ability to separate potential signal events from the SM background. We therefore aim to identify  $b$  or  $c$  quarks based on the presence of a  $SV$  reconstructed using the Inclusive Vertex Finder (IVF) [14]. Additional requirements on  $SV$  observable are applied to suppress the background originating from light quarks. These selected  $SV$  may be referred to as soft  $b$ -tags and are constructed to be orthogonal to the jets and  $b$ -tagged jet used in this analysis.

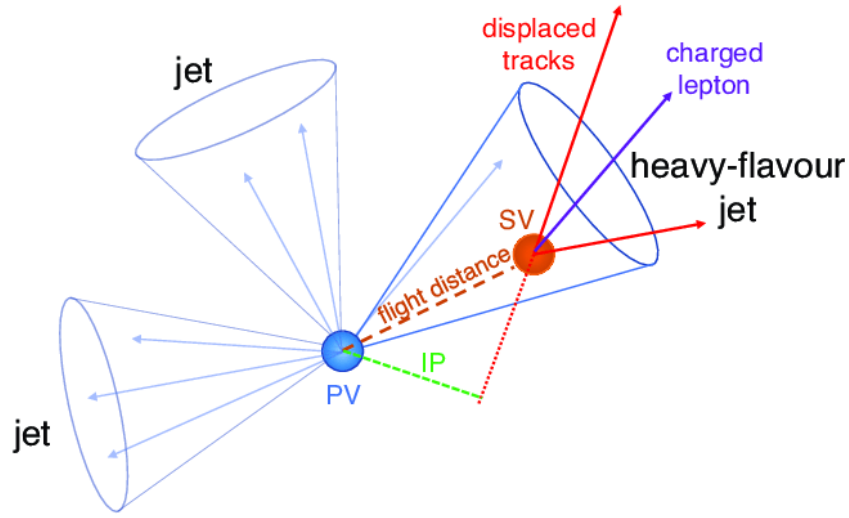


Figure 4.3 : A interaction that produces a long lived particle that has a reconstructed SV.

The requirements on each SV to pass the soft b-tagging definition are:

- The distance in the transverse plane between the SV and the PV  $\leq 3$  cm.
- The significance of the distance, SIP3D, between the SV and the PV  $\geq 4$ .
- The pointing angle, defined as  $\cos(\overrightarrow{PV}, \overrightarrow{SV}, \overrightarrow{p_{SV}}) \geq 0.98$ , where  $\overrightarrow{p_{SV}}$  is the total four-momentum of the tracks associated to the SV.
- The number of tracks associated to the SV is greater or equal to 3.
- The  $p_T$  of the SV is less than 20 GeV.

Identification of soft b-quarks is necessary for potential signal region where the stop does not directly decay into a top quark and is essential for some of our search region bins.

#### 4.1.6 Transverse Energy between $b$ quarks and $\cancel{E}_T$

We will end up dividing the search regions we are interested in into two different groups. They will be distinguished by a parameter known as the transverse mass between the leading  $b$  – jet and  $\cancel{E}_T$  defined as:

$$M_T(b_{1,2}, \cancel{E}_T) = \sqrt{2 \cdot \cancel{E}_T \cdot p_T(b)(1 - \cos(\cancel{E}_\phi, p_\phi(b)))}, \quad (4.3)$$

where  $p_T(b)$  is the momentum of the leading  $b$  – jet and  $\cancel{E}_\phi$  and  $p_\phi(b)$  is the  $\phi$  component of the missing energy and  $b$  – jet, respectively. This will be used to distinguish between our low and high mass search regions, see Section 4.3.1.

#### 4.1.7 Initial-state Radiation

Initial-state radiation (ISR) may be clustered into one of the large- $R$  jets clustered with a distance parameter,  $\Delta R = 0.8$ . We use the larger radius jets to be sensitive to ISR with gluon splitting, when a jet radiates a gluon that pair produces two quarks. The ISR jet is identified as being the hardest of the large- $R$  jets with  $p_T > 200$  GeV which fails the loose b-tagging working point and is not identified as a top or W. This is a good parameter for jets that a neither tagged as  $t$  or  $W$  is the low  $\Delta m$  region of our search.

#### 4.1.8 Electron and Muon Identification

There are two sets of selection criteria used in the analysis for electrons and muons. The set of criteria used to efficiently reject events with an isolated electron is done with a "Veto" tag. An electron with a Veto id must pass the following cuts:

- $|\Delta\eta| < 0.007(0.01), |\Delta\phi| < 0.8(0.7)$

- $\sigma_{i\eta i\eta} < 0.01(0.03)$
- $H/E < 0.15(N/A)$
- PF isolation/ $p_T$ (cone $\Delta R = 0.3$ )  $< 0.15(0.15)$
- $|d_0| < 0.04(0.04)$ ,  $|d_z| < 0.2(0.2)$

for the barrel and endcap regions of the detector, where  $H/E$  is the ratio of hadronic energy over electromagnetic energy. This veto ID is chosen such that the search region is most likely to be devoid of electrons, since it has a 95% efficiency [15].

We use the loose muon definition recommended by the Muon POG for the purposes of the muon veto [16]. A loose muon is identified as a Particle Flow (PF) [17] muon and can be either a global muon or an arbitrated tracker muon. Only candidates with transverse (longitudinal) impact parameter  $|d_0| < 0.2$  cm ( $|d_z| < 0.5$ cm,) with respect to the primary vertex, are considered. The electron and muon IDs are used in the definition of the Lost Lepton background which will be expanded upon further in Section 5.3.

#### 4.1.9 Tau Identification

The Tau ID has been studied extensively in tests which looked into the custom MVA [18, 19] similar to the one used in Ref. [20], a cut-based IsoTrack method, and Tau POG MVA method of identifying hadronically decaying taus. The methods which provide the best improvement to the efficiency of identifying taus with a small fake rate is the combination of IsoTrack and Tau POG MVA. With the inclusion of the combined method for identifying hadronically decaying taus, the veto percentage is  $\approx 29.0\%(7.2\%)$  with a efficiency of the veto of  $\approx 49.1\%(22.6\%)$  for SM background (signal), see Appendix. A.

For the IsoTrack method we require the following:

- $p_T \geq 5(10) GeV$ ,  $\text{iso} \leq 0.2(0.1)$  for electrons and muons(pions)
- $m_T(\text{isoTrack}, \cancel{E}_T) < 100 GeV$

where  $m_T(\text{isoTrack}, \cancel{E}_T)$  is the transverse mass between the isotrack and  $\cancel{E}_T$ . For the TauPOG method we require:

- $p_T \geq 20 GeV$ ,  $|\eta| < 2.4$
- idDecayMode, a booleon to identify hadronically decaying taus
- Medium working point.

With the inclusion of the separate electron/muon IDs and the combined IsoTrack + TauPOG IDs we have a method to efficiently veto leptons from our search region.

## 4.2 Samples

The primary dataset used for this analysis is the MET dataset. It contains events triggered by the HLT paths HLT\\_PFMETx\\_PFMHTx\\_IDTight and HLT\\_PFMETNoMux\\_PFMHTNoMux\\_IDTight where  $x = 100, 110, 120, 130$ , and  $140$ . The logical OR of these triggers is used to select the search sample. For studies of single- and dilepton control regions, we use the SingleMuon, SingleElectron, DoubleMuon, and DoubleEG datasets. The JetHT dataset is also used for studies of  $W$ /top-tagging. The SinglePhoton dataset is used to define a control region with a selected photon that is used together with  $Z \rightarrow ll$  samples for the prediction of the SM background originating from  $Z \rightarrow \nu\nu$  events. Table 4.1 lists all datasets together with the specific HLT paths of the triggers that were used for the selection of events. In cases

where there are inefficiencies due to the use of isolated triggers, a suite of triggers is used to recover efficiency wherever possible. The datasets correspond to the full Run 2 dataset are: “Run2016B”, “Run2016C”, “Run2016D”, “Run2016E”, “Run2016F”, “Run2016G”, “Run2016H”, “Run2017B”, “Run2017C”, “Run2017D”, “Run2017E”, “Run2017F”, “Run2018A”, “Run2018B”, “Run2018C”, and “Run2018D” acquisition eras with a total luminosity of  $136.7 \text{ fb}^{-1}$ , Table 4.1.

Primary dataset	HLT path
Search sample	
MET	HLT_PFMET100_PFMHT100_IDTight OR HLT_PFMETNoMu100_PFMHTNoMu100_IDTight OR HLT_PFMET110_PFMHT110_IDTight OR HLT_PFMETNoMu110_PFMHTNoMu110_IDTight OR HLT_PFMET120_PFMHT120_IDTight OR HLT_PFMETNoMu120_PFMHTNoMu120_IDTight OR HLT_PFMET130_PFMHT130_IDTight OR HLT_PFMETNoMu130_PFMHTNoMu130_IDTight OR HLT_PFMET140_PFMHT140_IDTight OR HLT_PFMETNoMu140_PFMHTNoMu140_IDTight OR HLT_PFMET100_PFMHT100_IDTight_PFHT60 OR HLT_PFMETNoMu100_PFMHTNoMu100_IDTight_PFHT60 OR HLT_PFMET110_PFMHT110_IDTight_PFHT60 OR HLT_PFMETNoMu110_PFMHTNoMu110_IDTight_PFHT60 OR HLT_PFMET120_PFMHT120_IDTight_PFHT60 OR HLT_PFMETNoMu120_PFMHTNoMu120_IDTight_PFHT60 OR HLT_PFMET130_PFMHT130_IDTight_PFHT60 OR HLT_PFMETNoMu130_PFMHTNoMu130_IDTight_PFHT60 OR HLT_PFMET140_PFMHT140_IDTight_PFHT60 OR HLT_PFMETNoMu140_PFMHTNoMu140_IDTight_PFHT60
Single-lepton control sample	
SingleMuon	HLT_IsoMu20 OR HLT_IsoTkMu20 OR HLT_IsoMu22 OR HLT_IsoTkMu22 OR HLT_IsoMu24 OR HLT_IsoTkMu24 OR HLT_IsoMu27 OR HLT_IsoTkMu27 OR HLT_IsoMu22_eta2p1 OR HLT_IsoMu24_eta2p1 OR HLT_IsoTkMu22 OR HLT_IsoTkMu24 OR HLT_Mu50 OR HLT_Mu55 OR
SingleElectron	HLT_Ele105_CaloDVT_GsfTrkIdT OR HLT_Ele115_CaloDVT_GsfTrkIdT OR HLT_Ele135_CaloDVT_GsfTrkIdT OR HLT_Ele145_CaloDVT_GsfTrkIdT OR HLT_Ele25_eta2p1_WP75t_Gsf OR HLT_Ele20_eta2p1_WP80loose_Gsf OR HLT_Ele27_eta2p1_WP80loose_Gsf OR HLT_Ele27_WP75t_Gsf OR HLT_Ele35_WP75t_Gsf OR HLT_Ele20_WP80loose_Gsf OR HLT_Ele45_WP80loose_Gsf OR Ele23_Ele12_CaloDL_TrackDL_IsoVL_OH_Ele23_Ele12_CaloDL_TrackDL_IsoVL_DZ OR DoubleEle33_CaloDL_GsfTrkIdVL_OR_DoubleEle33_CaloDL_GsfTrkIdVL_MW_OR_DoubleEle25_CaloDL_MW_OR_DoubleEle33_CaloDL_MW
MET	HLT_PFMET110_PFMHT110_IDTight OR HLT_PFMETNoMu110_PFMHTNoMu110_IDTight HLT_PFMET120_PFMHT120_IDTight OR HLT_PFMETNoMu120_PFMHTNoMu120_IDTight
JetHT DoubleEG	HLT_CaloJet500_NojetID HLT_ECALHT800
Dilepton control sample	
DoubleMuon	(all eras) kHLT_Mu30_TkMu11 (Before era H) HLT_Mu17_TrkIsoVVL_Mu8_TrkIsoVVL_OR HLT_Mu17_TrkIsoVVL_TkMu8_TrkIsoVVL (Era H) HLT_Mu17_TrkIsoVVL_Mu8_TrkIsoVVL_DZ_OR HLT_Mu17_TrkIsoVVL_TkMu8_TrkIsoVVL_DZ (Era H) HLT_TkMu17_TrkIsoVVL_TkMu8_TrkIsoVVL_DZ HLT_Mu50 OR HLT_TkMu50 HLT_Ele23_Ele12_CaloDL_IsoVL_DZ OR HLT_DoubleEle33_CaloDL_GsfTrkIdVL_MW
SingleMuon DoubleEG SingleElectron	HLT_Ele115_CaloDVT_GsfTrkIdT
Photon control sample	
SinglePhoton	HLT_Photon175 OR HLT_Photon200

Table 4.1 : Primary datasets used for the analysis and the HLT paths of the corresponding triggers. Datasets from Run2016 are “ReReco” legacy datasets from the 17Jul2018 re-reconstruction, Run2017 is from 31Mar2018 re-reconstruction, and Run2018 Run “A” to “C” are re-reconstruction while Run “D” is promptreco.

The simulated samples used in this analysis, all of which are listed in Table 4.2 and 4.3, were produced as part of the “Summer16”, “Fall17”, and “Autumn18” Monte Carlo production campaign for Run 2 in the “NanoAOD” data format.

Process	Generator	Dataset	Cross section [pb]
SM processes			
$t\bar{t}, 1\ell$	MADGRAPH	/TTJets_SingleLeptFromT_TuneCUETP8M1_13TeV-madgraphMLM-pythia8/<proc>	182.18
	MADGRAPH	/TTJets_SingleLeptFromTbar_TuneCUETP8M1_13TeV-madgraphMLM-pythia8/<proc>	182.18
	MADGRAPH	/TTJets_DiLept_TuneCUETP8M1_13TeV-madgraphMLM-pythia8/<proc>	87.31
$t\bar{t}, H_T$	MADGRAPH	/TTJets_HT-600to800_TuneCUETP8M1_13TeV-madgraphMLM-pythia8/<proc>	2.76
	MADGRAPH	/TTJets_HT-800to1200_TuneCUETP8M1_13TeV-madgraphMLM-pythia8/<proc>	1.1156
	MADGRAPH	/TTJets_HT-1200to2500_TuneCUETP8M1_13TeV-madgraphMLM-pythia8/<proc>	0.19775
	MADGRAPH	/TTJets_HT-2500toInf_TuneCUETP8M1_13TeV-madgraphMLM-pythia8/<proc>	0.00239
$t\bar{t}Z$	AMCATNLO	/TTZToLLNuNu_M-10_TuneCUETP8M1_13TeV-amcatnlo-pythia8/<proc>	0.2529
	AMCATNLO	/TTZToQQ_TuneCUETP8M1_13TeV-amcatnlo-pythia8/<proc>	0.5297
$t\bar{Z}q$	AMCATNLO	/tZq_ll_4f_13TeV-amcatnlo-pythia8_TuneCUETP8M1/<proc>	0.0758
$t\bar{W}$	MADGRAPH	/ST_tWl_5f_LO_13TeV-MadGraph-pythia8/<proc>	0.01104
	MADGRAPH	/ST_tWnumu_5f_LO_13TeV-MadGraph-pythia8/<proc>	0.02122
$t\bar{t}W$	AMCATNLO	/TTWJetsToLNu_TuneCUETP8M1_13TeV-amcatnloFXFX-madspin-pythia8/<proc>	0.2043
	AMCATNLO	/TTWJetsToQQ_TuneCUETP8M1_13TeV-amcatnloFXFX-madspin-pythia8/<proc>	0.4062
$t\bar{W}$	POWHEG	/ST_tW_top_5f_NoFullyHadronicDecays_13TeV-powheg_TuneCUETP8M1/<proc>	16.295
	POWHEG	/ST_tW_top_5f_inclusiveDecays_13TeV-powheg-pythia8_TuneCUETP8M1/<proc>	35.85
	POWHEG	/ST_tW_antitop_5f_NoFullyHadronicDecays_13TeV-powheg_TuneCUETP8M1/<proc>	16.295
	POWHEG	/ST_tW_antitop_5f_inclusiveDecays_13TeV-powheg-pythia8_TuneCUETP8M1/<proc>	35.85
$t\bar{W}, t\text{-channel}$	AMCATNLO	/ST_t-channel_top_4f_inclusiveDecays_13TeV-powhegV2-madspin-pythia8_TuneCUETP8M1/<proc>	136.065
	AMCATNLO	/ST_t-channel_antitop_4f_inclusiveDecays_13TeV-powhegV2-madspin-pythia8_TuneCUETP8M1/<proc>	80.97
$t\bar{W}, s\text{-channel}$	AMCATNLO	/ST_s-channel_4f_inclusiveDecays_13TeV-amcatnlo-pythia8_TuneCUETP8M1/<proc>	3.362
$W+jets$	MADGRAPH, HT bins	/WJetsToLNu_HT-70to100_TuneCUETP8M1_13TeV-madgraphMLM-pythia8/<proc>	1353
		/WJetsToLNu_HT-100To200_TuneCUETP8M1_13TeV-madgraphMLM-pythia8/<proc>	1345
		/WJetsToLNu_HT-200To400_TuneCUETP8M1_13TeV-madgraphMLM-pythia8/<proc>	359.7
		/WJetsToLNu_HT-400To600_TuneCUETP8M1_13TeV-madgraphMLM-pythia8/<proc>	48.91
		/WJetsToLNu_HT-600To800_TuneCUETP8M1_13TeV-madgraphMLM-pythia8/<proc>	12.05
		/WJetsToLNu_HT-800To1200_TuneCUETP8M1_13TeV-madgraphMLM-pythia8/<proc>	5.501
		/WJetsToLNu_HT-1200To2500_TuneCUETP8M1_13TeV-madgraphMLM-pythia8/<proc>	1.329
		/WJetsToLNu_HT-2500ToInf_TuneCUETP8M1_13TeV-madgraphMLM-pythia8/<proc>	0.03216
$Z \rightarrow \nu\nu$	MADGRAPH, HT bins	/ZJetsToNuNu_HT-100To200_13TeV-madgraph/<proc>	280.35
		/ZJetsToNuNu_HT-200To400_13TeV-madgraph/<proc>	77.67
		/ZJetsToNuNu_HT-400To600_13TeV-madgraph/<proc>	10.73
		/ZJetsToNuNu_HT-600To800_13TeV-madgraph/<proc>	2.559
		/ZJetsToNuNu_HT-800To1200_13TeV-madgraph/<proc>	1.1796
		/ZJetsToNuNu_HT-1200To2500_13TeV-madgraph/<proc>	0.28833
		/ZJetsToNuNu_HT-2500ToInf_13TeV-madgraph/<proc>	0.006945
QCD	MADGRAPH, HT bins	/QCD_HT100to200_TuneCUETP8M1_13TeV-madgraphMLM-pythia8/<proc>	27990000
		/QCD_HT200to300_TuneCUETP8M1_13TeV-madgraphMLM-pythia8/<proc>	1712000
		/QCD_HT300to500_TuneCUETP8M1_13TeV-madgraphMLM-pythia8/<proc>	347700
		/QCD_HT500to700_TuneCUETP8M1_13TeV-madgraphMLM-pythia8/<proc>	32100
		/QCD_HT700to1000_TuneCUETP8M1_13TeV-madgraphMLM-pythia8/<proc>	6831
		/QCD_HT1000to1500_TuneCUETP8M1_13TeV-madgraphMLM-pythia8/<proc>	1207
		/QCD_HT1500to2000_TuneCUETP8M1_13TeV-madgraphMLM-pythia8/<proc>	119.9
		/QCD_HT2000toInf_TuneCUETP8M1_13TeV-madgraphMLM-pythia8/<proc>	25.24
$gg+jets$	MADGRAPH, HT bins	/GJets_HT-100To200_TuneCUETP8M1_13TeV-madgraphMLM-pythia8/<proc>	5391.0
		/GJets_HT-200To400_TuneCUETP8M1_13TeV-madgraphMLM-pythia8/<proc>	1168.0
		/GJets_HT-400To600_TuneCUETP8M1_13TeV-madgraphMLM-pythia8/<proc>	132.5
		/GJets_HT-600ToInf_TuneCUETP8M1_13TeV-madgraphMLM-pythia8/<proc>	44.05
$t\bar{t}gg+jets$	AMCATNLO	/TTGJets_TuneCUETP8M1_13TeV-amcatnloFXFX-madspin-pythia8/<proc>	3.697
$DY+jets$	MADGRAPH, HT bins	/DYJetsToLL_M-50_HT-70to100_TuneCUETP8M1_13TeV-madgraphMLM-pythia8/<proc>	169.9
		/DYJetsToLL_M-50_HT-100to200_TuneCUETP8M1_13TeV-madgraphMLM-pythia8/<proc>	147.4
		/DYJetsToLL_M-50_HT-200to400_TuneCUETP8M1_13TeV-madgraphMLM-pythia8/<proc>	40.99
		/DYJetsToLL_M-50_HT-400to600_TuneCUETP8M1_13TeV-madgraphMLM-pythia8/<proc>	5.678
		/DYJetsToLL_M-50_HT-600to800_TuneCUETP8M1_13TeV-madgraphMLM-pythia8/<proc>	1.367
		/DYJetsToLL_M-50_HT-800to1200_TuneCUETP8M1_13TeV-madgraphMLM-pythia8/<proc>	0.6304
		/DYJetsToLL_M-50_HT-1200to2500_TuneCUETP8M1_13TeV-madgraphMLM-pythia8/<proc>	0.1514
		/DYJetsToLL_M-50_HT-2500toInf_TuneCUETP8M1_13TeV-madgraphMLM-pythia8/<proc>	0.003565
$WW$	POWHEG	/WWTo2L2Nu_13TeV-powheg/<proc>	12.178
	POWHEG	/WWToLNuQQ_13TeV-powheg/<proc>	49.997
	POWHEG	/WWTo4Q_13TeV-powheg/<proc>	51.723
$WZ$	AMCATNLO	/WZTo1L1Nu2Q_13TeV_amcatnloFXFX_madspin_pythia8/<proc>	10.71
	POWHEG	/WZTo3LNu_13TeV_TuneCUETP8M1_13TeV-powheg-pythia8/<proc>	4.42965
	AMCATNLO	/WZTo2L2Q_13TeV_amcatnloFXFX_madspin_pythia8/<proc>	5.595
	AMCATNLO	/WZTo1L3Nu_13TeV_amcatnloFXFX_madspin_pythia8/<proc>	3.033
$ZZ$	AMCATNLO	/ZZTo2Q2Nu_13TeV_amcatnloFXFX_madspin_pythia8/<proc>	4.033
	AMCATNLO	/ZZTo2L2Q_13TeV_amcatnloFXFX_madspin_pythia8/<proc>	3.22
	POWHEG	/ZZTo2L2Nu_13TeV_powheg_pythia8/<proc>	0.564
	POWHEG	/ZZTo4L_13TeV_powheg_pythia8/<proc>	1.212
	AMCATNLO	/ZZTo4Q_13TeV_amcatnloFXFX_madspin_pythia8/<proc>	6.912

Table 4.2 : Simulated event samples used for this analysis and the corresponding theoretical cross sections for the processes indicated. For some samples produced at leading order (LO), an additional multiplicative  $k$ -factor is applied to the LO total cross section to account for the difference with the next-to-leading order (NLO) cross section. Note that <proc> stands for the string “RunIISummer16MiniAODv3”, “RunIIFall17MiniAODv2”, and “RunIIAutumn18MiniAOD” for samples produced with the full detector simulation.

Process	Generator	Dataset		Cross section [pb]
Signal samples				
T1tttt, FullSim	MADGRAPH	/SMS-T1tttt_mGluino-2000_mLSP-100_TuneCUETP8M1_13TeV-madgraphMLM-pythia8/<proc>		0.000101
	MADGRAPH	/SMS-T1tttt_mGluino-1200_mLSP-800_TuneCUETP8M1_13TeV-madgraphMLM-pythia8/<proc>		0.0955
	MADGRAPH	/SMS-T1tttt_mGluino-1500_mLSP-100_TuneCUETP8M1_13TeV-madgraphMLM-pythia8/<proc>		0.0157
T2tt, FastSim	MADGRAPH	/SMS-T2tt_mStop-150to250_TuneCUETP8M1_13TeV-madgraphMLM-pythia8/<proc>		1.0
	MADGRAPH	/SMS-T2tt_mStop-250to350_TuneCUETP8M1_13TeV-madgraphMLM-pythia8/<fast_proc>		1.0
	MADGRAPH	/SMS-T2tt_mStop-350to400_TuneCUETP8M1_13TeV-madgraphMLM-pythia8/<fast_proc>		1.0
	MADGRAPH	/SMS-T2tt_mStop-400to1200_TuneCUETP8M1_13TeV-madgraphMLM-pythia8/<fast_proc>		1.0
	MADGRAPH	/SMS-T2tt_mStop-1200to2000_TuneCUETP8M1_13TeV-madgraphMLM-pythia8/<fast_proc>		1.0
T2tt, FullSim	MADGRAPH	/SMS-T2tt_mStop-225_mLSP-50_TuneCUETP8M1_13TeV-madgraphMLM-pythia8/<proc>		42.0
	MADGRAPH	/SMS-T2tt_mStop-250_mLSP-150_TuneCUETP8M1_13TeV-madgraphMLM-pythia8/<proc>		24.8
	MADGRAPH	/SMS-T2tt_mStop-250_mLSP-50_TuneCUETP8M1_13TeV-madgraphMLM-pythia8/<proc>		24.8
	MADGRAPH	/SMS-T2tt_mStop-300_mLSP-150_TuneCUETP8M1_13TeV-madgraphMLM-pythia8/<proc>		10.0
	MADGRAPH	/SMS-T2tt_mStop-325_mLSP-150_TuneCUETP8M1_13TeV-madgraphMLM-pythia8/<proc>		6.57
	MADGRAPH	/SMS-T2tt_mStop-425_mLSP-325_TuneCUETP8M1_13TeV-madgraphMLM-pythia8/<proc>		1.54
	MADGRAPH	/SMS-T2tt_mStop-500_mLSP-325_TuneCUETP8M1_13TeV-madgraphMLM-pythia8/<proc>		0.609
	MADGRAPH	/SMS-T2tt_mStop-650_mLSP-350_TuneCUETP8M1_13TeV-madgraphMLM-pythia8/<proc>		0.125
	MADGRAPH	/SMS-T2tt_mStop-850_mLSP-100_TuneCUETP8M1_13TeV-madgraphMLM-pythia8/<proc>		0.0216
T2fb, FastSim	MADGRAPH	/SMS-T2tb_dM-10to80_genHT-160_genMET-80_nWMin-0p1_TuneCUETP8M1_13TeV-madgraphMLM-pythia8/<fast_proc>		21.59-0.02833
T2cc, FastSim	MADGRAPH	/SMS-T2cc_genHT-160_genMET-80_TuneCUETP8M1_13TeV-madgraphMLM-pythia8/<fast_proc>		249.4-0.02833
T2bw, FastSim	MADGRAPH	/SMS-T2bw_TuneCUETP8M1_13TeV-madgraphMLM-pythia8/<fast_proc>		64.50-0.001598
T2tb, FastSim	MADGRAPH	/SMS-T2tb_TuneCUETP8M1_13TeV-madgraphMLM-pythia8/<fast_proc>		64.50-0.003074

Table 4.3 : Simulated event samples used for this analysis and the corresponding theoretical cross sections for the processes indicated. For some samples produced at leading order (LO), an additional multiplicative  $k$ -factor is applied to the LO total cross section to account for the difference with the next-to-leading order (NLO) cross section. Note that <proc> stands for the string “RunIISummer16MiniAODv3”, “RunIIFall17MiniAODv2”, and “RunIIAutumn18MiniAOD” for samples produced with the full detector simulation.

#### 4.2.1 Filters

The following filters, recommended by the JetMET POG, are applied to 2016, 2017, and 2018 eras:

- goodVertices
- HBHENoiseFilter
- HBHENoiseIsoFilter
- EcalDeadCellTriggerPrimitiveFilter
- BadPFMuonFilter
- GlobalSuperTightHalo2016Filter

- eeBadScFilter

There is an addition ecalBadCalibFilter for 2017 and 2018 eras only.

### 4.3 Baseline Selection

Following the same methods as above, we have a loose pre-selection which is referred to as the baseline selection. This will place a selection on jets and  $\cancel{E}_T$  which is used to eliminate a large fraction of background events. We define the baseline selection as:

- $N_{e,(\mu)} = 0, (p_T \geq 5 \text{ GeV}, |\eta| < 2.5(2.4), \text{miniISO} < 0.1(0.2))$
- $N_{isoTrk} = 0, (p_T \geq 5(10) \text{ GeV}, \text{ISO} < 0.2(0.1) \text{ for electron/muons(pions)})$
- $N_{tauPOG} = 0, (p_T \geq 20 \text{ GeV}, |\eta| < 2.4), \text{medium working point}$
- $N_j \geq 2, (p_T \geq 30 \text{ GeV}, |\eta| < 2.4)$
- $\cancel{E}_T \geq 250 \text{ GeV}, \text{to reach the plateau of the trigger efficiency}$
- $H_T \geq 300 \text{ GeV}$
- HEM Veto for part of 2018 data:  $-3 \leq \eta \leq -1.4, -1.57 \leq \phi \leq -0.87$

In Addition to this, we allow for two separate sets of additional selections to apply to the low and high  $\Delta m$  search regions to further reduce background. The high  $\Delta m$  baseline selection includes the baseline selection and additionally,

- $N_j \geq 5, (p_T \geq 30 \text{ GeV}, |\eta| < 2.4)$
- $N_b \geq 1, (p_T \geq 20 \text{ GeV}, |\eta| < 2.4), \text{medium DeepCSV working point}$

- $\text{Min}[|\Delta\phi(\cancel{E}_T, j_1)|, |\Delta\phi(\cancel{E}_T, j_2)|, |\Delta\phi(\cancel{E}_T, j_3)|, |\Delta\phi(\cancel{E}_T, j_4)|] \equiv \Delta\phi_{1234} \geq 0.5$ , where  $j_1, j_2, j_3, j_4$  are the four leading jets in  $p_T$ . This requirement is to reduce the QCD multijet background.

Next, the low  $\Delta m$  baseline selection has the following addition selections,

- $N_t = 0, N_W = 0, N_{res} = 0$ , where  $N_t$  and  $N_W$  are the number of merged tops and  $W$ 's, respectively, and  $N_{res}$  is the number of resolved tops
- An ISR jet as defined in Sec. 4.1.7 with  $p_T(\text{ISR}) \geq 200 \text{ GeV}, |\eta| < 2.4, |\Delta\phi(j_{ISR}, \cancel{E}_T)| \geq 2$ .
- $\cancel{E}_T/\sqrt{H_T} \equiv S_{\cancel{E}_T} \geq 10$ , where  $H_T$  is calculated as the scalar sum of the  $p_T$  of jets with  $p_T \geq 30 \text{ GeV}$  and  $|\eta| < 2.4$ .
- $|\Delta\phi(j_1, \cancel{E}_T)| \geq 0.5, |\Delta\phi(j_{2,3}, \cancel{E}_T)| \geq 0.15$ , where  $j_1, j_2, j_3$  are the three leading jets in  $p_T$ .

### 4.3.1 Search Regions

After applying the baseline selection criteria, we categorize events in the search sample into exclusive search regions that exploit the kinematic properties of different signal topologies.

For the search regions that mainly target high  $\Delta m$  signal models, we define two event categories in  $M_T(b_{1,2}, \cancel{E}_T)$ , see Section 4.3, a variable defined as

$$M_T(b_{1,2}, \cancel{E}_T) \equiv \begin{cases} m_T(b, \cancel{E}_T), N_b = 1 \\ \text{Min}[m_T(b_1, \cancel{E}_T), m_T(b_2, \cancel{E}_T)], N_b \geq 2 \end{cases} \quad (4.4)$$

where  $b_1, b_2$  are the two selected b-tagged jets with the highest values of the DeepCSV discriminator. In  $t\bar{t}$  events where one of the  $W$  bosons undergoes a leptonic decay

and the lepton is missed causes  $\cancel{E}_T$ . The transverse mass of  $\cancel{E}_T$  and the b-quark from the same top decay as the missed lepton has a kinematic endpoint at the mass of the top-quark. We therefore define two event categories:  $M_T(b_{1,2}, \cancel{E}_T) > 175\text{ GeV}$  and  $< 175\text{ GeV}$ , see fig. 4.4. In the low- $M_T(b_{1,2}, \cancel{E}_T)$  category, to target signal models with moderate values of  $\Delta m$ , we define search regions by requiring  $N_j \geq 7$  and  $N_{res} \geq 1$  to benefit from potential ISR in signal events while suppressing the SM background. Events are then subdivided according to the number of b-tagged jets ( $N_b = 1, = 2, \geq 3$ ) and different  $\cancel{E}_T$  thresholds. The same subdivision is performed for events in the high- $M_T(b_{1,2}, \cancel{E}_T)$  category with  $N_j \geq 7$ , but containing no top- or W-tagged candidates. We then target signal models with sufficiently boosted top quarks or W bosons by defining categories in the high- $M_T(b_{1,2}, \cancel{E}_T)$  region that require the presence of at least one top- or W-tagged candidate. These categories do not have any further  $N_j$  requirement beyond that of the high  $\Delta m$  baseline selection, and are further subdivided according to  $N_b, \cancel{E}_T, H_T$  and the number of each kind of top- and W-tagged candidate. Table 4.5 summarizes the definitions of all 130 disjoint search regions targeting high  $\Delta m$  signal models.

Events originating from low  $\Delta m$  signal models are likely to have lower values of  $M_T(b_{1,2}, \cancel{E}_T)$ . We therefore only use the low- $M_T(b_{1,2}, \cancel{E}_T)$  category to define search regions targeting these signal models. These search regions are further defined by the number of b-tagged jets, the number of identified secondary vertices ( $N_{SV}$ ), the ISR jet  $p_T(p_T(b))$ , and  $\cancel{E}_T$ . Events in the  $N_b = 0$  category, which targets very compressed signal models, are further subdivided according to  $N_j$ . Only events with very high ISR  $p_T(> 500\text{ GeV})$  are selected in this category, which is also categorized by the presence or absence of soft b-tagged secondary vertices. Events in the  $N_b = 1$  category are further characterized according to the  $p_T$  of the b-tagged jet into two sub-categories, while those in the  $N_b \geq 2$  are subdivided based on  $p_T(b_{12})$  into three

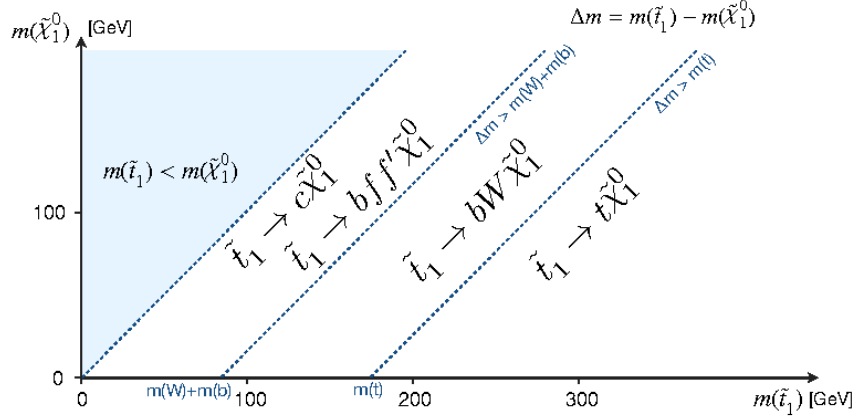


Figure 4.4 : Mass parameter space for different decay modes of the top squark.

sub-categories, in order to take advantage of the softer b jet  $p_T$  spectrum expected in signal events compared to the SM background. Orthogonality to the high  $\Delta m$  event categories is achieved mostly by the  $M_T(b_{1,2}, \cancel{E}_T)$  categorization. Table 4.4 summarizes the definitions of the 53 disjoint search regions targeting low  $\Delta m$  signal models. The numbers are based on simulation and correspond to an integrated luminosity of  $136.7 \text{ fb}^{-1}$ .

Table 4.4 : Summary of the 53 disjoint search regions that mainly target low  $\Delta m$  signal models. The low  $\Delta m$  baseline selection is again  $N_j \geq 2$ ,  $\cancel{E}_T > 250$  GeV,  $N_t = N_W = N_{res} = 0$ ,  $N_b \geq 0$ ,  $M_T(b_{1,2}, \cancel{E}_T) < 175$  GeV (when applicable),  $|\Delta\phi(j_1, \cancel{E}_T)| > 0.5$ ,  $|\Delta\phi(j_{2,3}, \cancel{E}_T)| > 0.15$ ,  $p_T(ISR) > 200$  GeV,  $|\eta(ISR)| < 2.4$ ,  $|\Delta\phi(j_{ISR}, \cancel{E}_T)| > 2$ , and  $S_{\cancel{E}_T} > 10$ .

$N_j$	$N_b$	$N_{SV}$	$p_T(ISR)$ [GeV]	$p_T(b)$ [GeV]	$\cancel{E}_T$ [GeV]
2 – 5 $\geq 6$	0	0	$> 500$	-	450 – 550, 550 – 650, 650 – 750, $> 750$
		0			450 – 550, 550 – 650, 650 – 750, $> 750$
		$\geq 1$			450 – 550, 550 – 650, 650 – 750, $> 750$
		$\geq 1$			450 – 550, 550 – 650, 650 – 750, $> 750$
$\geq 2$	1	0	300 – 500	20 – 40	300 – 400, 400 – 500, 500 – 600, $> 600$
		0	300 – 500	40 – 70	300 – 400, 400 – 500, 500 – 600, $> 600$
		0	$> 500$	20 – 40	450 – 550, 550 – 650, 650 – 750, $> 750$
		0	$> 500$	40 – 70	450 – 550, 550 – 650, 650 – 750, $> 750$
		$\geq 1$	$> 300$	20 – 40	300 – 400, 400 – 500, $> 500$
$\geq 2$ $\geq 2$ $\geq 7$ $\geq 2$ $\geq 2$ $\geq 7$	$\geq 2$	$\geq 0$	300 – 500	40 – 80	300 – 400, 400 – 500, $> 500$
			300 – 500	80 – 140	300 – 400, 400 – 500, $> 500$
			300 – 500	$> 140$	300 – 400, 400 – 500, $> 500$
			$> 500$	40 – 80	450 – 550, 550 – 650, $> 650$
			$> 500$	80 – 140	450 – 550, 550 – 650, $> 650$
			$> 300$	$> 140$	450 – 550, 550 – 650, $> 650$

Table 4.5 : Summary of the 130 disjoint search regions that mainly target high  $\Delta m$  signal models. The high  $\Delta m$  baseline selection is again  $N_j \geq 5$ ,  $\cancel{E}_T > 250 \text{ GeV}$ ,  $N_b \geq 1$ , and  $\Delta\phi_{1234} > 0.5$ .

$M_T(b_{1,2}, \cancel{E}_T) < 175 \text{ GeV}$						
$N_j$	$N_b$	$N_t$	$N_W$	$N_{res}$	$H_T [\text{GeV}]$	$\cancel{E}_T [\text{GeV}]$
$\geq 7$	$1, \geq 2$	$\geq 0$	$\geq 0$	$\geq 1$	$\geq 300$	$250 - 300, 300 - 400, 400 - 500, \geq 500$
$M_T(b_{1,2}, \cancel{E}_T) \geq 175 \text{ GeV}$						
$N_j$	$N_b$	$N_t$	$N_W$	$N_{res}$	$H_T [\text{GeV}]$	$\cancel{E}_T [\text{GeV}]$
$\geq 5$	$1, \geq 2$	$0$	$0$	$0$	$\geq 1000$	$250 - 350, 350 - 450, 450 - 550, \geq 550$
$\geq 5$	1	$\geq 1$	0	0	$300 - 1000, 1000 - 1500, \geq 1500$	$250 - 550, 550 - 650, \geq 650$
		0	$\geq 1$	0	$300 - 1300, \geq 1300$	$250 - 350, 350 - 450, \geq 450$
		0	0	$\geq 1$	$300 - 1000, 1000 - 1500, \geq 1500$	$250 - 350, 350 - 450, 450 - 550, 550 - 650, \geq 650$
		$\geq 1$	$\geq 1$	0	$\geq 300$	$250 - 550, \geq 550$
		$\geq 1$	0	$\geq 1$	$\geq 300$	$250 - 550, \geq 550$
		0	$\geq 1$	$\geq 1$	$\geq 300$	$250 - 550, \geq 550$
		1	0	0	$300 - 1000, 1000 - 1500, \geq 1500$	$250 - 550, 550 - 650, \geq 650$
$\geq 5$	2	0	1	0	$300 - 1300, \geq 1300$	$250 - 350, 350 - 450, \geq 450$
		0	0	1	$300 - 1000, 1000 - 1500, \geq 1500$	$250 - 350, 350 - 450, 450 - 550, 550 - 650, \geq 650$
		1	1	0	$\geq 300$	$250 - 550, \geq 550$
		1	0	1	$300 - 1300, \geq 1300$	$250 - 350, 350 - 450, \geq 450$
		0	1	1	$\geq 300$	$250 - 550, \geq 550$
		2	0	0	$\geq 300$	$250 - 450, \geq 450$
		0	2	0	$\geq 300$	$\geq 250$
		0	0	2	$300 - 1300, \geq 1300$	$250 - 450, \geq 450$
		$N_t + N_W + N_{res} \geq 3$			$\geq 300$	$\geq 250$
		1	0	0	$300 - 1000, 1000 - 1500, \geq 1500$	$250 - 350, 350 - 550, \geq 550$
$\geq 5$	$\geq 3$	0	1	0	$\geq 300$	$250 - 350, 350 - 550, \geq 550$
		0	0	1	$300 - 1000, 1000 - 1500, \geq 1500$	$250 - 350, 350 - 550, \geq 550$
		1	1	0	$\geq 300$	$\geq 250$
		1	0	1	$\geq 300$	$250 - 350, \geq 350$
		0	1	1	$\geq 300$	$\geq 250$
		2	0	0	$\geq 300$	$\geq 250$
		0	2	0	$\geq 300$	$\geq 250$
		0	0	2	$\geq 300$	$250 - 350, \geq 350$
		$N_t + N_W + N_{res} \geq 3$			$\geq 300$	$\geq 250$

## Chapter 5

# Top Squark Production and Backgrounds

We have now motivated that the top squark,  $\tilde{t}_1$ , could be the lightest squark, see Sec. 2.3.4. This allows us to possibly produce them at CMS. In Sec. 4.3, we have designed a search that will look for events with large amounts of  $\cancel{E}_T$  and  $N_j$ . These events are being targeted in separate low  $\Delta m$  and high  $\Delta m$  search regions. For all of these we are interested in comparing the data and background in each search or control region. We will look at the production and decay modes of various  $\tilde{t}_1$  interactions and the estimation of the SM background of each region.

### 5.1 Production and Decay Modes

To produce the top squark all we need is the collision of two proton-proton beams. It is shown as a black circle in the Fig. 5.2 and 5.1. This is meant to represent many processes that can make a top squark. The main processes are gluon fusion, when two gluons fuse into a single gluon which then decays into a top and anti-top squark pair, or annihilation, where two quarks annihilate to a gluon propagator which thus decays into two top squarks.

The main decay mode of the top squark is  $\tilde{t}_1 \rightarrow t + \tilde{\chi}_1^0$  and  $\tilde{t}_1 \rightarrow b + \tilde{\chi}^\pm$ , Fig. 5.1. The top quark most likely decays as,  $t \rightarrow bW^+$ , while the  $b$  quark will decay to either a  $c$  or an  $u$  quark in its decay chain with an additional  $W$  boson. The  $\tilde{\chi}_1^0$  is proposed to be a stable dark matter candidate while the  $\tilde{\chi}^\pm$  could decay as,  $\tilde{\chi}^\pm \rightarrow \tilde{\chi}_1^0 W$ . Next,

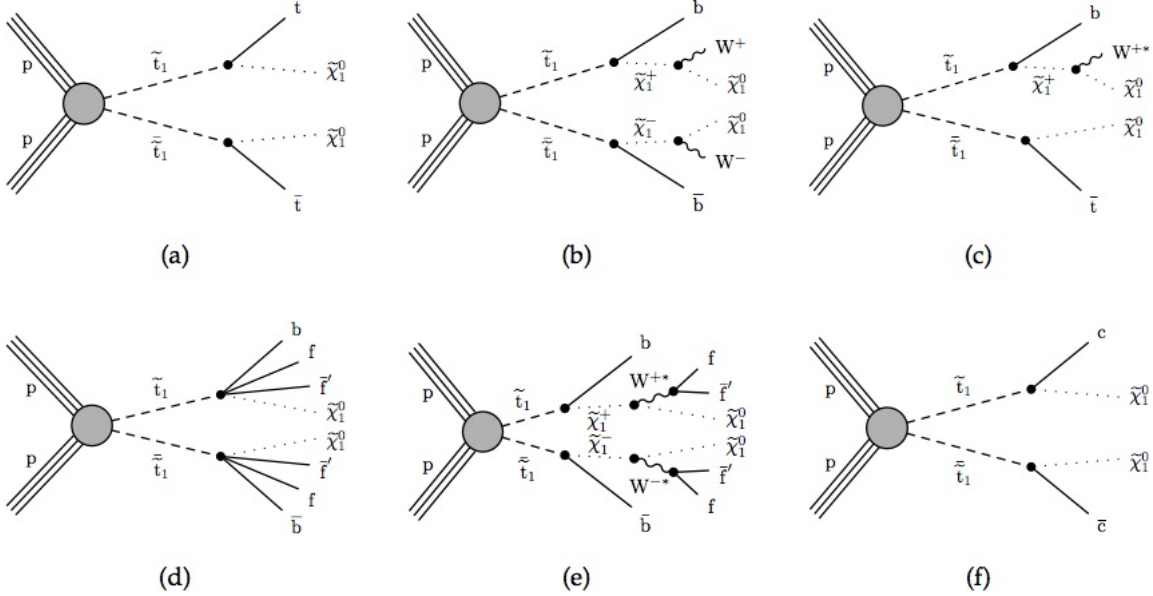


Figure 5.1 : Feynman diagrams for the direct  $\tilde{t}_1$  production in SUSY. The allowed decay modes are (a) T2tt, (b) T2bW, (c) T2tb, (d,e) T2ff'd, and (f) T2cc.

a four body decay is allowed for,  $\tilde{t}_1 \rightarrow bff'\tilde{\chi}_1^0$ , see Fig. 5.1(d,e). The final direct  $\tilde{t}_1$  production we are interested in is the  $\tilde{t}_1 \rightarrow c\tilde{\chi}_1^0$ , see Fig. 5.1(f). To be as inclusive as possible, we are also including indirect top squark production as see in Fig. 5.2. GET A CONCISE DESCRIPTION OF THE INDIRECT DIAGRAMS. We see that the  $\tilde{t}_1$  will decay to multiple jets,  $N_j$ , and missing transverse energy,  $\cancel{E}_T$ . Now we are going to try to estimate the SM background that could be in each of our search region bins.

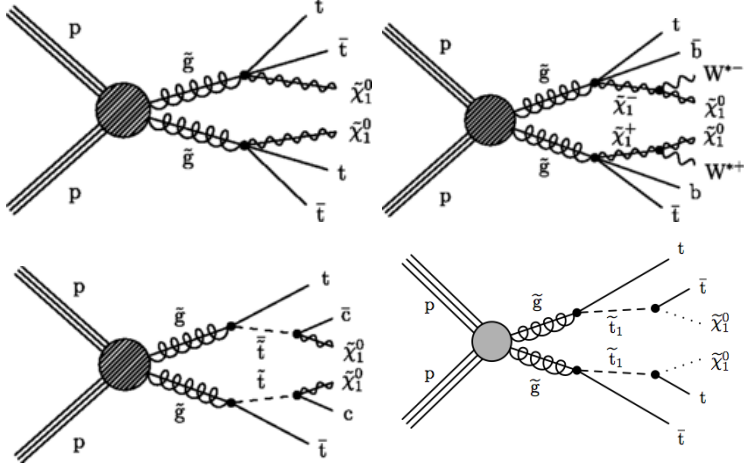


Figure 5.2 : Feynman diagrams for the indirect  $\tilde{t}_1$  production in SUSY. The allowed decay modes are T1tttt (top left), T1ttbb (top right), T5ttcc (bottom left), and T5tttt (bottom right).

## 5.2 Standard Model Background

The standard model background for the top squark search is defined by a large  $\cancel{E}_T$  and a multiple jets. There are a couple types of SM background that can be misinterpreted as our signal. The most likely background is that which causes many tops (or heavy particles) and missing energy. Events in the SM like  $t\bar{t}$  and  $W+jets$  will have many jets produced and  $\cancel{E}_T$  due to a missed lepton and neutrino. The production of heavy particles like  $Z \rightarrow \nu\nu$  will give multiple jets and  $\cancel{E}_T$  from the neutrinos being missed by the detector. QCD events often produce events with multiple jets, due to acceptances in the detector the jets can sometimes be mis-measured which can cause large  $\cancel{E}_T$ . There are also various processes that are quite rare which are quite rare but still need to be accounted for.

### 5.3 Lost Lepton

The contribution from the  $t\bar{t}$  and  $W + \text{jets}$  processes arises from leptonic decays of the  $W$  boson, where the charged lepton is outside the kinematic acceptance of CMS or evades identification by the dedicated lepton vetoes. Large  $\cancel{E}_T$  can be generated by the associated neutrino and the lepton that is not reconstructed, allowing such events to enter the search regions. This background is collectively referred to as the "Lost Lepton" (LL) background. Contributions arising from  $tW$ ,  $t\bar{t}W$  and single-top processes also enter into this category, but with much smaller importance.

Studies in simulation indicate that the event kinematics for different lepton flavors are similar enough to allow us to estimate them collectively from a single control sample in data that has event characteristics similar to those of the search sample. Because of this, we use the single-lepton control sample to estimate the LL background, using the method described in detail in Ref. [21]. The single-lepton sample consists of events that have one lepton satisfying the lepton-veto criteria. In order to suppress potential signal contamination, we require  $M_T(l, \cancel{E}_T) < 100 \text{ GeV}$ . The requirement of low  $M_T(l, \cancel{E}_T)$  also ensures orthogonality to the search regions used in direct top squark production in the single-lepton or double-lepton final state, making it possible to statistically combine the results of the two searches. The selection applied to the single-lepton control sample follows the same selection on the search variables as in the zero-lepton selection with the exception of classification according to the number of top and  $W$ -tagged candidates.

#### 5.3.1 Combining All Run 2 Eras

Firstly, for this analysis we are interested in the possibility in combining the yields of each era into one estimation. This is initially done by looking at the  $\cancel{E}_T$

distributions in each era. Since the LL estimation is done with the transfer factor method, a good confirmation would be the comparison of the transfer factor in each SR for each era.

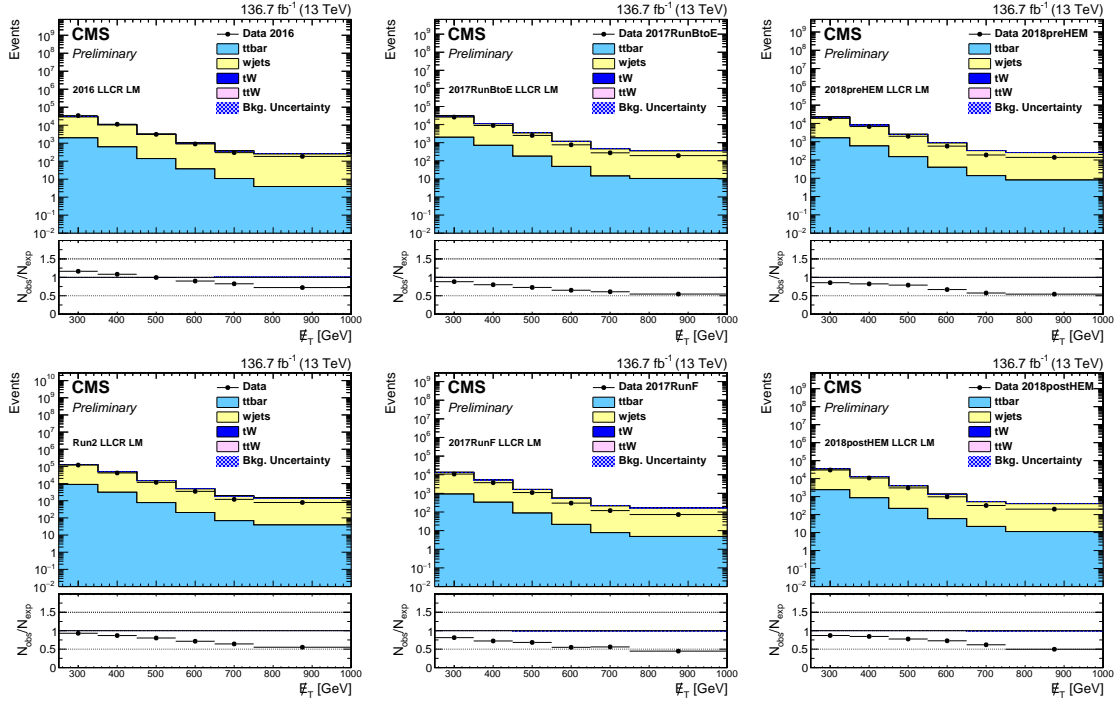


Figure 5.3 : Comparison of the Data and MC in the 1Lep CR for each era: Run2016, Run2017BtoE, Run2017F, Run2018preHEM, Run2018PostHEM, and the combination of all eras in the Low  $\Delta m$  region. Each era has a good agreement between Data and MC.

### 5.3.2 Transfer Factors

The LL estimation in each search region is based upon the event count in data in the corresponding control region in the single-lepton sample. The count is extrapolated to the search region to obtain a prediction by means of a transfer factor

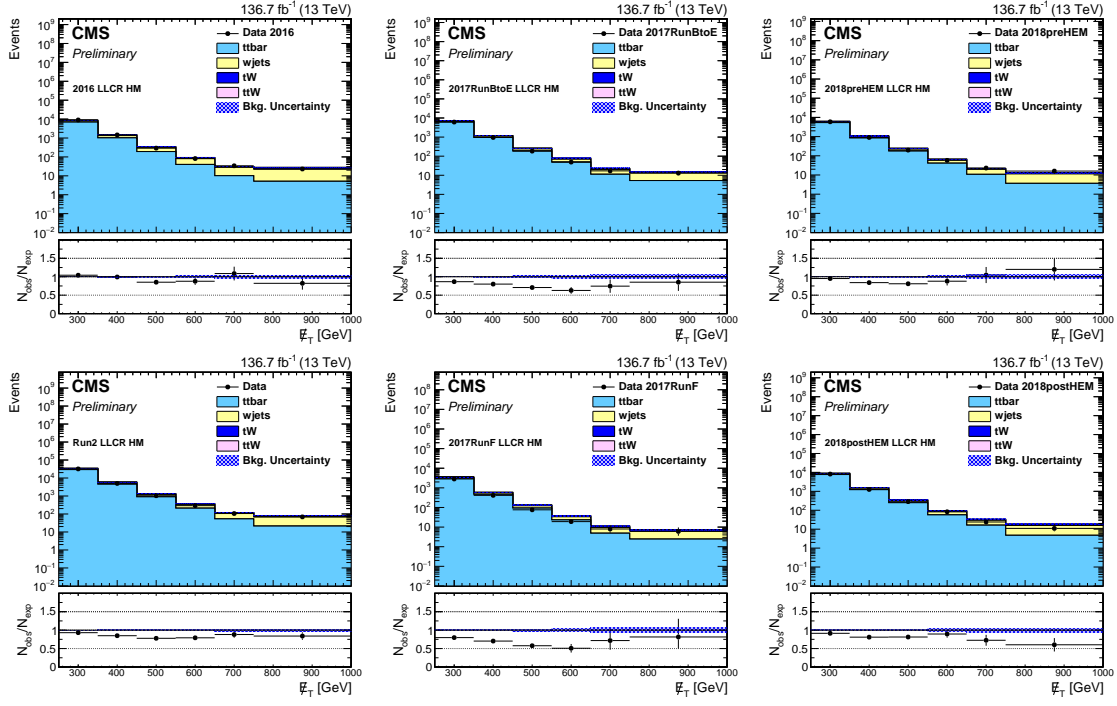


Figure 5.4 : Comparison of the Data and MC in the 1Lep CR for each era: Run2016, Run2017BtoE, Run2017F, Run2018preHEM, Run2018PostHEM, and the combination of all eras in the High  $\Delta m$  region. Each era has a good agreement between Data and MC.

obtained from simulation as follows:

$$N_{pred}^{LL} = TF_{LL} \cdot N_{data}(1l). \quad (5.1)$$

This allows us to have the same selection for the single-lepton control sample and the zero-lepton sample. The only exception is the number of top and W-tagged candidates. The LL estimation is dependent on the yield of data in the corresponding CR and the TF calculated by the single-lepton sample. The transfer factor is defined

as,

$$TF_{LL} = \frac{N_{MC}(0l)}{N_{MC}(1l)}, \quad (5.2)$$

where  $N_{MC}(1l)$  is the event count observed in the corresponding CR and  $N_{MC}(0l)$  use the event count in the corresponding SR.

The main motivation behind this approach is to increase the statistical precision of the background estimation. The performance of the  $t$  and  $W$  taggers has been studied in data and MC samples and a reasonably good agreement is observed allowing us to proceed with this approach. Data-to-MC scale factors are extracted and applied to MC to account for residual differences of the tagging performance in data. Detailed studies comparing the performance of the  $t$  and  $W$  taggers in data and MC [20].

The control regions utilized to predict the LL background are displayed in Fig. 5.7 to ???. The figures 5.7 to 5.8 display the control regions specific to the low  $\Delta m$  selection, where the regions are binned following the search region definition. Figures 5.9 to ??? display the control regions dedicated for the high  $\Delta m$  selection. Due to the nature of the background estimation method applied in the high  $\Delta m$  search, control regions are utilized for the prediction of multiple search regions.

Tables 5.1 to 5.4 summarize the yields in data observed in the single-lepton sample, the derived transfer factor, and the resulting LL predictions for the low  $\Delta m$  and high  $\Delta m$  search regions respectively. The transfer factors in the high  $\Delta m$  region actually account for two levels of extrapolation. The CR for the high  $\Delta m$  is loose such that, there is no binning in tops or  $W$  tagging. We then extrapolate to the SR with the inclusion of the top and  $W$  tags, along with scale factors, to estimate the

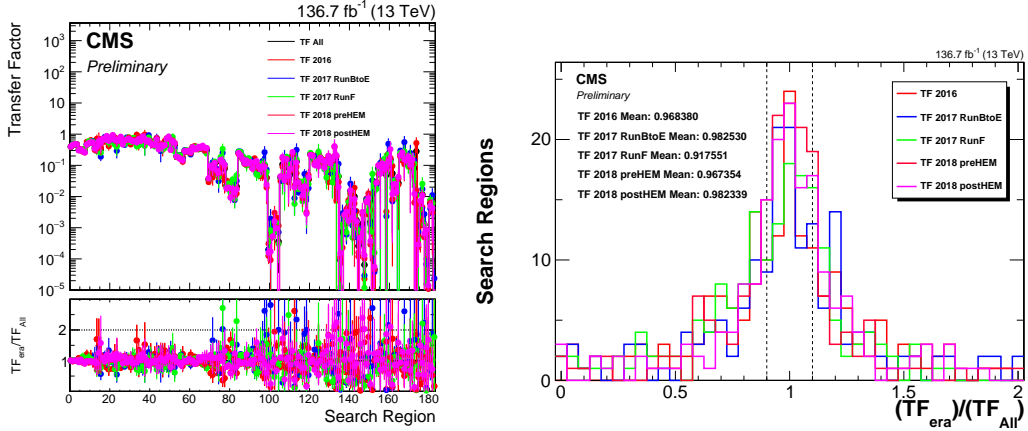


Figure 5.5 : Comparisons of the transfer factors for each era of MC in the low and high  $\Delta m$  regions. The values are shown in their separate bins on the left plot and in a combined form on the right. The mean for each is also shown.

LL background in the region:

$$\begin{aligned} TF_{LL} &= TF_{LL}^{CR-SR} \times TF_{LL}^{SR-extrap} \\ &= \frac{N_{MC}(0l)(N_j, N_b, \not{E}_T)}{N_{MC}(1l)(N_j, N_b, \not{E}_T)} \times \frac{N_{MC}(0l)(N_j, N_b, \not{E}_T, N_t, N_{res}, N_W)}{N_{MC}(0l)(N_j, N_b, \not{E}_T)}. \end{aligned} \quad (5.3)$$

We now want to consider how the transfer factor for each era relates to the total transfer factor. In Fig. 5.5 and 5.6, we see the comparison the the total  $TF$  for each era of the data and simulation. These are all in quite good agreement, but we see a large peak near zero. Once we alter the comparison for the  $TF$  for the CR-to-SR and the SR-to-Extrapolation. We see a much better agreement when we do not include the cuts on top/W tagging. These are improved because of the better statistics in the region.

Now that we have confirmed that the LL background is valid to be combined to be

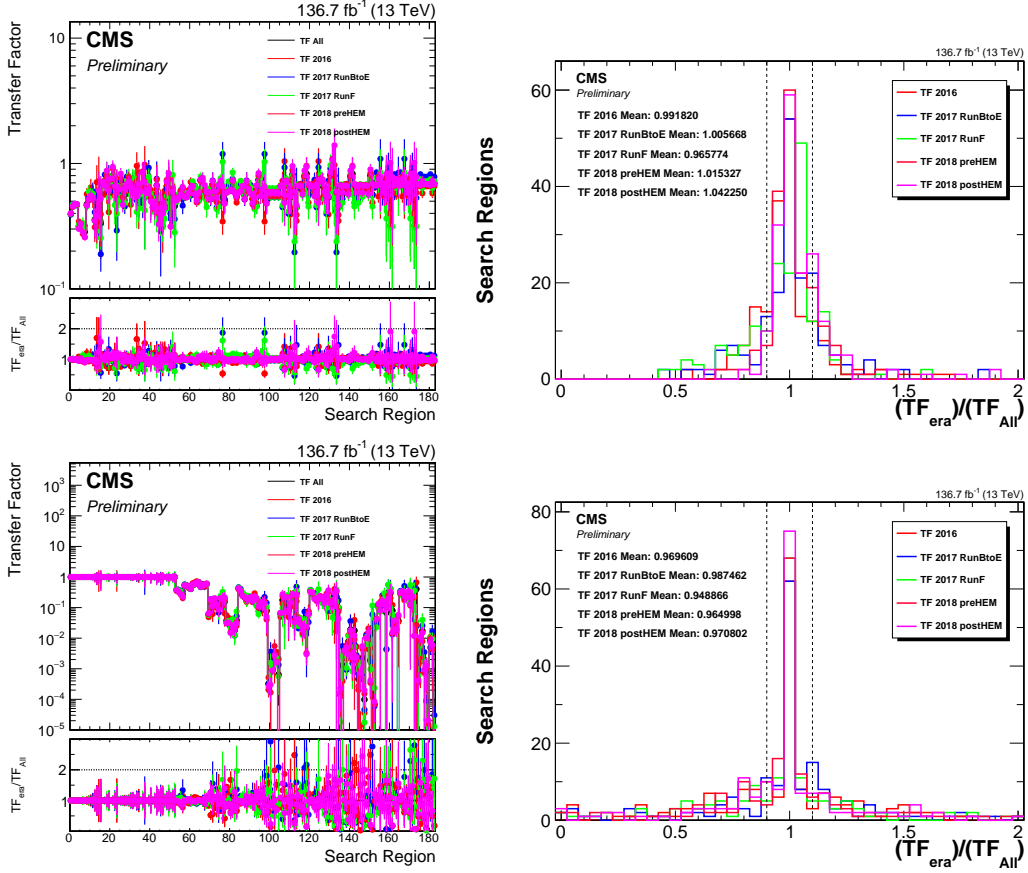


Figure 5.6 : Comparisons of the transfer factors, separated into the CR-to-SR (top) and SR-to-extrapolation (bottom), for each era of MC in the low and high  $\Delta m$  regions. The values are shown in their separate bins on the left plot and in a combined form on the right. The mean for each is also shown.

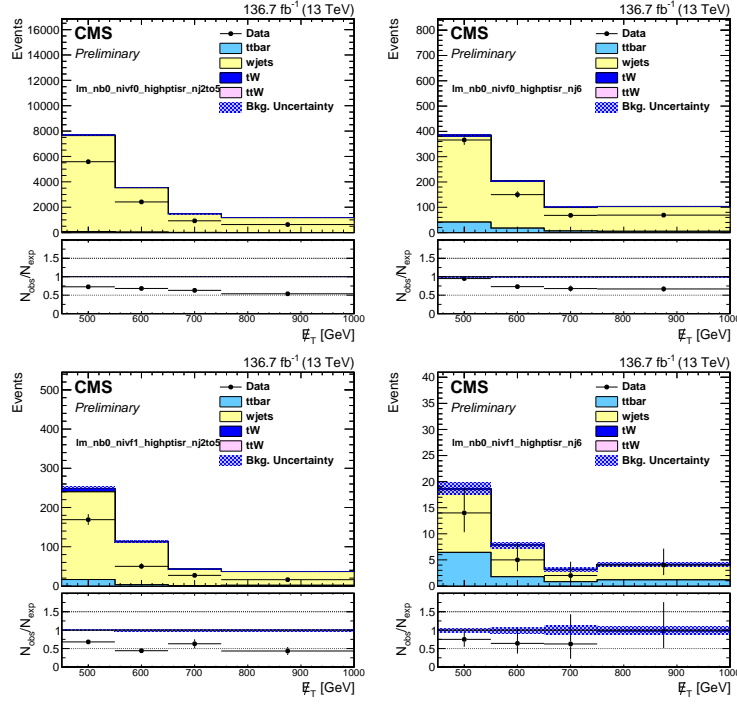


Figure 5.7 : Comparison of the  $\cancel{E}_T$  distribution in the single-lepton sample after applying the low  $\Delta m$  baseline selection in the  $N_b = 0$  region. Data and simulation are represented by the black points and stacked histograms, respectively. The error bars on the ratio of observed data to simulation correspond to the data statistical uncertainty and the shaded blue band represents the statistical uncertainty on the simulation. These regions are included with the search regions in the simultaneous fit for the signal extraction in order to estimate the LL contribution.

combined for all the eras. The transfer factors and control region comparisons confirm that each era can be combined in the final estimation. Now with the combinations of each era for the LL back ground, we can consider the combination of the other background estimations.

Search Region	$\not{E}_T$ [GeV]	$N_{\text{data}}(II)$	$TF_{LL}$	$N_{\text{pred}}^{\text{LL}}$
low $\Delta m$ , $N_b = 0$ , $N_{SV} = 0$ , $p_T(\text{ISR}) \geq 500 \text{ GeV}$ , $2 \leq N_j \leq 5$				
0	450–550	5585	0.396±0.003	2212.80±34.21
1	550–650	2415	0.459±0.004	1108.97±24.16
2	650–750	927	0.474±0.004	439.19±14.87
3	$\geq 750$	632	0.470±0.004	296.80±12.13
low $\Delta m$ , $N_b = 0$ , $N_{SV} = 0$ , $p_T(\text{ISR}) \geq 500 \text{ GeV}$ , $N_j \geq 6$				
4	450–550	366	0.317±0.006	115.86±6.49
5	550–650	150	0.319±0.009	47.78±4.14
6	650–750	68	0.294±0.011	20.00±2.53
7	$\geq 750$	69	0.285±0.008	19.69±2.44
low $\Delta m$ , $N_b = 0$ , $N_{SV} \geq 1$ , $p_T(\text{ISR}) \geq 500 \text{ GeV}$ , $2 \leq N_j \leq 5$				
8	450–550	169	0.473±0.019	79.87±6.94
9	550–650	50	0.533±0.022	26.63±3.92
10	650–750	27	0.562±0.028	15.18±3.02
11	$\geq 750$	16	0.558±0.035	8.93±2.30
low $\Delta m$ , $N_b = 0$ , $N_{SV} \geq 1$ , $p_T(\text{ISR}) \geq 500 \text{ GeV}$ , $N_j \geq 6$				
12	450–550	14	0.357±0.042	4.99±1.46
13	550–650	5	0.418±0.069	2.09±1.00
14	650–750	2	0.486±0.085	0.97±0.71
15	$\geq 750$	4	0.332±0.076	1.33±0.73
low $\Delta m$ , $N_b = 1$ , $N_{SV} = 0$ , $M_T(b_{1,2}, \not{E}_T) < 175 \text{ GeV}$ , $300 \leq p_T(\text{ISR}) < 500 \text{ GeV}$ , $p_T(b) < 40 \text{ GeV}$				
16	300–400	1923	0.654±0.014	1258.07±38.72
17	400–500	317	0.685±0.030	217.02±15.45
18	500–600	32	0.738±0.062	23.60±4.62
19	$\geq 600$	6	0.568±0.066	3.41±1.45
low $\Delta m$ , $N_b = 1$ , $N_{SV} = 0$ , $M_T(b_{1,2}, \not{E}_T) < 175 \text{ GeV}$ , $p_T(\text{ISR}) \geq 500 \text{ GeV}$ , $p_T(b) < 40 \text{ GeV}$				
20	300–400	1062	0.727±0.018	771.93±30.49
21	400–500	133	0.801±0.047	106.55±11.12
22	500–600	12	0.642±0.077	7.70±2.41
23	$\geq 600$	6	0.533±0.115	3.20±1.48
low $\Delta m$ , $N_b = 1$ , $N_{SV} = 0$ , $M_T(b_{1,2}, \not{E}_T) < 175 \text{ GeV}$ , $p_T(\text{ISR}) \geq 500 \text{ GeV}$ , $40 < p_T(b) < 70 \text{ GeV}$				
24	450–550	140	0.571±0.026	79.90±7.69
25	550–650	43	0.721±0.038	31.00±5.00
26	650–750	13	0.508±0.031	6.61±1.88
27	$\geq 750$	15	0.560±0.034	8.40±2.23
low $\Delta m$ , $N_b = 1$ , $N_{SV} = 0$ , $M_T(b_{1,2}, \not{E}_T) < 175 \text{ GeV}$ , $p_T(\text{ISR}) \geq 500 \text{ GeV}$ , $40 < p_T(b) < 70 \text{ GeV}$				
28	450–550	100	0.702±0.040	70.23±8.09
29	550–650	22	0.727±0.045	15.99±3.55
30	650–750	11	0.596±0.053	6.56±2.06
31	$\geq 750$	5	0.645±0.065	3.23±1.48
low $\Delta m$ , $N_b = 1$ , $N_{SV} \geq 1$ , $M_T(b_{1,2}, \not{E}_T) < 175 \text{ GeV}$ , $p_T(b) < 40 \text{ GeV}$				
32	300–400	111	0.645±0.046	71.55±8.47
33	400–500	24	0.577±0.067	13.85±3.25
34	$\geq 500$	14	0.624±0.071	8.74±2.54
low $\Delta m$ , $N_b \geq 2$ , $M_T(b_{1,2}, \not{E}_T) < 175 \text{ GeV}$ , $300 \leq p_T(\text{ISR}) < 500 \text{ GeV}$ , $p_T(b_{12}) < 80 \text{ GeV}$				
35	300–400	247	0.590±0.026	145.70±11.29
36	400–500	36	0.695±0.068	25.02±4.83
37	$\geq 500$	8	0.641±0.154	5.13±2.19
low $\Delta m$ , $N_b \geq 2$ , $M_T(b_{1,2}, \not{E}_T) < 175 \text{ GeV}$ , $300 \leq p_T(\text{ISR}) < 500 \text{ GeV}$ , $80 < p_T(b_{12}) < 140 \text{ GeV}$				
38	300–400	607	0.572±0.015	347.33±16.63
39	400–500	105	0.722±0.045	75.78±8.80
40	$\geq 500$	17	0.540±0.081	9.19±2.62
low $\Delta m$ , $N_b \geq 2$ , $M_T(b_{1,2}, \not{E}_T) < 175 \text{ GeV}$ , $300 \leq p_T(\text{ISR}) < 500 \text{ GeV}$ , $p_T(b_{12}) \geq 140 \text{ GeV}$ , $N_j \geq 7$				
41	300–400	124	0.483±0.023	59.88±6.06
42	400–500	26	0.465±0.041	12.09±2.60
43	$\geq 500$	7	0.669±0.116	4.68±1.95
low $\Delta m$ , $N_b \geq 2$ , $M_T(b_{1,2}, \not{E}_T) < 175 \text{ GeV}$ , $p_T(\text{ISR}) \geq 500 \text{ GeV}$ , $p_T(b_{12}) < 80 \text{ GeV}$				
44	450–550	19	0.404±0.050	7.67±2.00
45	550–650	7	0.407±0.078	2.85±1.21
46	$\geq 650$	2	0.400±0.066	0.80±0.58
low $\Delta m$ , $N_b \geq 2$ , $M_T(b_{1,2}, \not{E}_T) < 175 \text{ GeV}$ , $p_T(\text{ISR}) \geq 500 \text{ GeV}$ , $80 < p_T(b_{12}) < 140 \text{ GeV}$				
47	450–550	58	0.455±0.034	26.41±3.99
48	550–650	16	0.657±0.073	10.51±2.88
49	$\geq 650$	6	0.732±0.105	4.39±1.90
low $\Delta m$ , $N_b \geq 2$ , $M_T(b_{1,2}, \not{E}_T) < 175 \text{ GeV}$ , $p_T(\text{ISR}) \geq 500 \text{ GeV}$ , $p_T(b_{12}) \geq 140 \text{ GeV}$ , $N_j \geq 7$				
50	450–550	37	0.398±0.038	14.74±2.79
51	550–650	12	0.572±0.072	6.87±2.16
52	$\geq 650$	3	0.457±0.076	1.37±0.82

Table 5.1 : The LL estimate in the various low  $\Delta m$  search regions, bins 0 to 53, using the 136.7  $\text{fb}^{-1}$  dataset.

Search Region	$\cancel{E}_T$ [GeV]	$N_{\text{data}}(1)$	$TF_{LL}$	$TF_{LL}^{\text{CR,SR}}$	$TF_{LL}^{\text{SR-extrap}}$	$N_{\text{pred}}^{\text{LL}}$
high $\Delta m$ , $N_b = 1$ , $M_T(b_{1,2}, \cancel{E}_T) < 175$ GeV, $N_j \geq 7$ , $N_{\text{res}} \geq 1$						
53	250–300	1151	0.196±0.004	0.519	0.378	225.43±8.24
54	300–400	697	0.187±0.005	0.550	0.340	130.35±6.21
55	400–500	129	0.180±0.011	0.577	0.313	23.26±2.53
56	≥ 500	43	0.157±0.016	0.598	0.263	6.77±1.25
high $\Delta m$ , $N_b \geq 2$ , $M_T(b_{1,2}, \cancel{E}_T) < 175$ GeV, $N_j \geq 7$ , $N_{\text{res}} \geq 1$						
57	250–300	2250	0.292±0.004	0.539	0.542	657.73±16.12
58	300–400	1256	0.286±0.005	0.548	0.522	359.11±11.69
59	400–500	236	0.278±0.010	0.582	0.478	65.56±4.92
60	≥ 500	99	0.259±0.017	0.625	0.415	25.67±3.06
high $\Delta m$ , $N_b = 1$ , $M_T(b_{1,2}, \cancel{E}_T) \geq 175$ GeV, $N_t = 0$ , $N_{\text{res}} = 0$ , $N_W = 0$ , $H_T \geq 1000$						
61	250–350	570	0.383±0.007	0.657	0.583	218.28±10.01
62	350–450	233	0.369±0.011	0.614	0.602	86.03±6.16
63	450–550	102	0.362±0.015	0.544	0.666	36.97±3.96
64	≥ 550	109	0.352±0.013	0.531	0.663	38.39±3.93
high $\Delta m$ , $N_b \geq 2$ , $M_T(b_{1,2}, \cancel{E}_T) \geq 175$ GeV, $N_t = 0$ , $N_{\text{res}} = 0$ , $N_W = 0$ , $H_T \geq 1000$						
65	250–350	186	0.359±0.013	0.738	0.486	66.78±5.49
66	350–450	57	0.379±0.021	0.675	0.561	21.58±3.11
67	450–550	23	0.334±0.027	0.616	0.542	7.69±1.72
68	≥ 550	32	0.317±0.025	0.537	0.590	10.14±1.97
high $\Delta m$ , $N_b = 1$ , $M_T(b_{1,2}, \cancel{E}_T) \geq 175$ GeV, $N_t \geq 1$ , $N_{\text{res}} = 0$ , $N_W = 0$ , $H_T < 1000$						
69	250–550	11329	0.035±0.001	0.601	0.058	397.77±7.71
70	550–650	87	0.081±0.010	0.553	0.147	7.07±1.14
71	≥ 650	29	0.075±0.015	0.684	0.110	2.18±0.59
high $\Delta m$ , $N_b = 1$ , $M_T(b_{1,2}, \cancel{E}_T) \geq 175$ GeV, $N_t \geq 1$ , $N_{\text{res}} = 0$ , $N_W = 0$ , $1000 \leq H_T < 1500$						
72	250–550	739	0.111±0.004	0.621	0.179	81.90±4.07
73	550–650	36	0.063±0.011	0.507	0.125	2.27±0.55
74	≥ 650	42	0.053±0.011	0.539	0.098	2.23±0.56
high $\Delta m$ , $N_b = 1$ , $M_T(b_{1,2}, \cancel{E}_T) \geq 175$ GeV, $N_t \geq 1$ , $N_{\text{res}} = 0$ , $N_W = 0$ , $H_T \geq 1500$						
75	250–550	166	0.131±0.008	0.690	0.190	21.70±2.19
76	550–650	8	0.124±0.030	0.637	0.195	0.99±0.43
77	≥ 650	23	0.079±0.019	0.506	0.156	1.81±0.57
high $\Delta m$ , $N_b = 1$ , $M_T(b_{1,2}, \cancel{E}_T) \geq 175$ GeV, $N_t = 0$ , $N_{\text{res}} = 0$ , $N_W \geq 1$ , $H_T < 1300$						
78	250–350	9720	0.023±0.000	0.594	0.038	220.56±5.06
79	350–450	1773	0.023±0.001	0.638	0.036	40.40±2.18
80	≥ 450	586	0.015±0.001	0.612	0.025	9.07±0.94
high $\Delta m$ , $N_b = 1$ , $M_T(b_{1,2}, \cancel{E}_T) \geq 175$ GeV, $N_t = 0$ , $N_{\text{res}} = 0$ , $N_W \geq 1$ , $H_T \geq 1300$						
81	250–350	206	0.023±0.003	0.718	0.032	4.67±0.68
82	350–450	87	0.011±0.002	0.607	0.018	0.94±0.22
83	≥ 450	87	0.021±0.004	0.545	0.038	1.82±0.37
high $\Delta m$ , $N_b = 1$ , $M_T(b_{1,2}, \cancel{E}_T) \geq 175$ GeV, $N_t = 0$ , $N_{\text{res}} \geq 1$ , $N_W = 0$ , $H_T < 1000$						
84	250–350	9356	0.253±0.002	0.592	0.427	2362.92±30.67
85	350–450	1627	0.227±0.004	0.640	0.355	369.27±11.50
86	450–550	346	0.169±0.007	0.652	0.259	58.49±4.01
87	550–650	87	0.123±0.011	0.553	0.223	10.73±1.49
88	≥ 650	29	0.118±0.017	0.684	0.173	3.44±0.80
high $\Delta m$ , $N_b = 1$ , $M_T(b_{1,2}, \cancel{E}_T) \geq 175$ GeV, $N_t = 0$ , $N_{\text{res}} \geq 1$ , $N_W = 0$ , $1000 \leq H_T < 1500$						
89	250–350	470	0.126±0.005	0.639	0.198	59.43±3.64
90	350–450	187	0.128±0.008	0.619	0.207	23.93±2.35
91	450–550	82	0.089±0.009	0.520	0.171	7.28±1.11
92	550–650	36	0.121±0.016	0.507	0.239	4.36±0.93
93	≥ 650	42	0.086±0.011	0.539	0.160	3.61±0.73

Table 5.2 : The LL estimate in the various high  $\Delta m$  search regions, bins 53–93, using the 136.7  $\text{fb}^{-1}$  dataset.

Search Region	$\cancel{E}_T$ [GeV]	$N_{\text{data}}(ll)$	$TF_{LL}$	$TF_{LL}^{\text{CR-SR}}$	$TF_{LL}^{\text{SR-extrap}}$	$N_{\text{pred}}^{\text{LL}}$
high $\Delta m$ , $N_b = 1$ , $M_T(b_{1,2}, \cancel{E}_T) \geq 175$ GeV, $N_t = 0$ , $N_{\text{res}} \geq 1$ , $N_W = 0$ , $H_T \geq 1500$						
94	250–350	100	0.075±0.008	0.744	0.100	7.46±1.06
95	350–450	46	0.069±0.011	0.589	0.118	3.19±0.68
96	450–550	20	0.087±0.017	0.649	0.135	1.75±0.52
97	550–650	8	0.101±0.029	0.637	0.158	0.80±0.37
98	$\geq 650$	23	0.040±0.011	0.506	0.079	0.92±0.31
high $\Delta m$ , $N_b = 1$ , $M_T(b_{1,2}, \cancel{E}_T) \geq 175$ GeV, $N_t \geq 1$ , $N_{\text{res}} = 0$ , $N_W \geq 1$						
99	250–550	12234	0.000±0.000	0.604	0.000	2.42±0.44
100	$\geq 550$	225	0.001±0.000	0.557	0.001	0.16±0.10
high $\Delta m$ , $N_b = 1$ , $M_T(b_{1,2}, \cancel{E}_T) \geq 175$ GeV, $N_t \geq 1$ , $N_{\text{res}} \geq 1$ , $N_W = 0$						
101	250–550	12234	0.001±0.000	0.604	0.001	6.76±0.80
102	$\geq 550$	225	0.002±0.001	0.557	0.003	0.35±0.13
high $\Delta m$ , $N_b = 1$ , $M_T(b_{1,2}, \cancel{E}_T) \geq 175$ GeV, $N_t = 0$ , $N_{\text{res}} \geq 1$ , $N_W \geq 1$						
103	250–550	12234	0.001±0.000	0.604	0.002	17.29±1.17
104	$\geq 550$	225	0.000±0.000	0.557	0.001	0.08±0.07
high $\Delta m$ , $N_b = 2$ , $M_T(b_{1,2}, \cancel{E}_T) \geq 175$ GeV, $N_t = 1$ , $N_{\text{res}} = 0$ , $N_W = 0$ , $H_T < 1000$						
105	250–550	2055	0.040±0.001	0.650	0.062	82.37±3.55
106	550–650	15	0.108±0.022	0.614	0.176	1.62±0.53
107	$\geq 650$	7	0.084±0.030	0.737	0.115	0.59±0.31
high $\Delta m$ , $N_b = 2$ , $M_T(b_{1,2}, \cancel{E}_T) \geq 175$ GeV, $N_t = 1$ , $N_{\text{res}} = 0$ , $N_W = 0$ , $1000 \leq H_T < 1500$						
108	250–550	151	0.149±0.009	0.710	0.210	22.56±2.25
109	550–650	7	0.042±0.016	0.521	0.080	0.29±0.15
110	$\geq 650$	13	0.089±0.028	0.539	0.165	1.16±0.48
high $\Delta m$ , $N_b = 2$ , $M_T(b_{1,2}, \cancel{E}_T) \geq 175$ GeV, $N_t = 1$ , $N_{\text{res}} = 0$ , $N_W = 0$ , $H_T \geq 1500$						
111	250–550	45	0.202±0.022	0.819	0.246	9.07±1.67
112	550–650	3	0.052±0.035	0.418	0.126	0.16±0.14
113	$\geq 650$	5	0.134±0.044	0.446	0.301	0.67±0.37
high $\Delta m$ , $N_b = 2$ , $M_T(b_{1,2}, \cancel{E}_T) \geq 175$ GeV, $N_t = 0$ , $N_{\text{res}} = 0$ , $N_W = 1$ , $H_T < 1300$						
114	250–350	1742	0.025±0.001	0.657	0.038	43.11±2.60
115	350–450	340	0.023±0.002	0.656	0.036	7.96±0.92
116	$\geq 450$	121	0.014±0.003	0.601	0.023	1.71±0.40
high $\Delta m$ , $N_b = 2$ , $M_T(b_{1,2}, \cancel{E}_T) \geq 175$ GeV, $N_t = 0$ , $N_{\text{res}} = 0$ , $N_W = 1$ , $H_T \geq 1300$						
117	250–350	52	0.028±0.006	0.793	0.036	1.47±0.38
118	350–450	21	0.017±0.008	0.828	0.021	0.36±0.19
119	$\geq 450$	25	0.035±0.011	0.566	0.062	0.87±0.33
high $\Delta m$ , $N_b = 2$ , $M_T(b_{1,2}, \cancel{E}_T) \geq 175$ GeV, $N_t = 0$ , $N_{\text{res}} = 1$ , $N_W = 0$ , $H_T < 1000$						
120	250–350	1661	0.225±0.004	0.651	0.346	373.86±11.68
121	350–450	317	0.196±0.009	0.659	0.297	62.06±4.44
122	450–550	77	0.147±0.014	0.605	0.243	11.32±1.69
123	550–650	15	0.143±0.026	0.614	0.234	2.15±0.68
124	$\geq 650$	7	0.173±0.048	0.737	0.235	1.21±0.57
high $\Delta m$ , $N_b = 2$ , $M_T(b_{1,2}, \cancel{E}_T) \geq 175$ GeV, $N_t = 0$ , $N_{\text{res}} = 1$ , $N_W = 0$ , $H_T < 1500$						
125	250–350	105	0.171±0.011	0.752	0.227	17.91±2.12
126	350–450	30	0.119±0.014	0.663	0.180	3.57±0.78
127	450–550	16	0.102±0.018	0.590	0.172	1.63±0.49
128	550–650	7	0.104±0.026	0.521	0.199	0.73±0.33
129	$\geq 650$	13	0.110±0.028	0.539	0.204	1.43±0.54
high $\Delta m$ , $N_b = 2$ , $M_T(b_{1,2}, \cancel{E}_T) \geq 175$ GeV, $N_t = 0$ , $N_{\text{res}} = 1$ , $N_W = 0$ , $H_T \geq 1500$						
130	250–350	28	0.125±0.020	0.812	0.154	3.49±0.87
131	350–450	14	0.090±0.024	0.844	0.106	1.26±0.48
132	450–550	3	0.194±0.064	0.800	0.243	0.58±0.39
133	550–650	3	0.094±0.052	0.418	0.225	0.28±0.23
134	$\geq 650$	5	0.044±0.020	0.446	0.099	0.22±0.14

Table 5.3 : The LL estimate in the various high  $\Delta m$  search regions, bins 94–134, using the  $136.7 \text{ fb}^{-1}$  dataset.

Search Region	$\cancel{E}_T$ [GeV]	$N_{\text{data}}(1l)$	$TF_{LL}$	$TF_{LL}^{\text{CR-SR}}$	$TF_{LL}^{\text{SR-extrap}}$	$N_{\text{pred}}^{\text{LL}}$
high $\Delta m$ , $N_b = 2$ , $M_T(b_{1,2}, \cancel{E}_T) \geq 175$ GeV, $N_t = 1$ , $N_{\text{res}} = 0$ , $N_W = 1$						
135	250–550	2251	0.000±0.000	0.659	0.000	0.21±0.09
136	$\geq 550$	50	0.001±0.001	0.566	0.001	0.04±0.03
high $\Delta m$ , $N_b = 2$ , $M_T(b_{1,2}, \cancel{E}_T) \geq 175$ GeV, $N_t = 1$ , $N_{\text{res}} = 1$ , $N_W = 0$ , $H_T < 1300$						
137	250–350	1742	0.003±0.000	0.657	0.004	4.39±0.66
138	350–450	340	0.002±0.001	0.656	0.003	0.72±0.22
139	$\geq 450$	121	0.005±0.001	0.601	0.008	0.57±0.19
high $\Delta m$ , $N_b = 2$ , $M_T(b_{1,2}, \cancel{E}_T) \geq 175$ GeV, $N_t = 1$ , $N_{\text{res}} = 1$ , $N_W = 0$ , $H_T \geq 1300$						
140	250–350	52	0.015±0.005	0.793	0.019	0.79±0.29
141	350–450	21	0.002±0.001	0.828	0.002	0.04±0.02
142	$\geq 450$	25	0.010±0.005	0.566	0.018	0.25±0.13
high $\Delta m$ , $N_b = 2$ , $M_T(b_{1,2}, \cancel{E}_T) \geq 175$ GeV, $N_t = 0$ , $N_{\text{res}} = 1$ , $N_W = 1$						
143	250–550	2251	0.002±0.000	0.659	0.003	3.93±0.59
144	$\geq 550$	50	0.000±0.000	0.566	0.000	0.01±0.01
high $\Delta m$ , $N_b = 2$ , $M_T(b_{1,2}, \cancel{E}_T) \geq 175$ GeV, $N_t = 2$ , $N_{\text{res}} = 0$ , $N_W = 0$						
145	250–450	2155	0.000±0.000	0.662	0.000	0.66±0.23
146	$\geq 450$	146	0.001±0.001	0.596	0.002	0.20±0.13
high $\Delta m$ , $N_b = 2$ , $M_T(b_{1,2}, \cancel{E}_T) \geq 175$ GeV, $N_t = 0$ , $N_{\text{res}} = 0$ , $N_W = 2$						
147	$\geq 250$	2301	0.000±0.000	0.657	0.000	0.15±0.06
high $\Delta m$ , $N_b = 2$ , $M_T(b_{1,2}, \cancel{E}_T) \geq 175$ GeV, $N_t = 0$ , $N_{\text{res}} = 2$ , $N_W = 0$ , $H_T < 1300$						
148	250–450	2082	0.008±0.001	0.656	0.012	15.82±1.28
149	$\geq 450$	121	0.007±0.002	0.601	0.012	0.86±0.26
high $\Delta m$ , $N_b = 2$ , $M_T(b_{1,2}, \cancel{E}_T) \geq 175$ GeV, $N_t = 0$ , $N_{\text{res}} = 2$ , $N_W = 0$ , $H_T \geq 1300$						
150	250–450	73	0.002±0.001	0.803	0.002	0.11±0.08
151	$\geq 450$	25	0.012±0.006	0.566	0.022	0.31±0.16
high $\Delta m$ , $N_b = 2$ , $M_T(b_{1,2}, \cancel{E}_T) \geq 175$ GeV, $(N_t + N_{\text{res}} + N_W) \geq 3$						
152	$\geq 250$	2301	0.000±0.000	0.657	0.000	0.10±0.05
high $\Delta m$ , $N_b \geq 3$ , $M_T(b_{1,2}, \cancel{E}_T) \geq 175$ GeV, $N_t = 1$ , $N_{\text{res}} = 0$ , $N_W = 0$ , $H_T < 1000$						
153	250–350	373	0.027±0.003	0.715	0.037	9.94±1.15
154	350–550	93	0.080±0.010	0.682	0.117	7.43±1.19
155	$\geq 550$	8	0.077±0.033	0.737	0.104	0.62±0.34
high $\Delta m$ , $N_b \geq 3$ , $M_T(b_{1,2}, \cancel{E}_T) \geq 175$ GeV, $N_t = 1$ , $N_{\text{res}} = 0$ , $N_W = 0$ , $1000 \leq H_T < 1500$						
156	250–350	41	0.112±0.017	0.645	0.174	4.60±1.01
157	350–550	13	0.099±0.020	0.603	0.165	1.29±0.44
158	$\geq 550$	1	0.050±0.037	0.735	0.068	0.05±0.06
high $\Delta m$ , $N_b \geq 3$ , $M_T(b_{1,2}, \cancel{E}_T) \geq 175$ GeV, $N_t = 1$ , $N_{\text{res}} = 0$ , $N_W = 0$ , $H_T \geq 1500$						
159	250–350	12	0.227±0.052	0.722	0.314	2.72±1.01
160	350–550	4	0.156±0.060	0.532	0.294	0.63±0.39
161	$\geq 550$	3	0.055±0.049	0.697	0.079	0.17±0.18
high $\Delta m$ , $N_b \geq 3$ , $M_T(b_{1,2}, \cancel{E}_T) \geq 175$ GeV, $N_t = 0$ , $N_{\text{res}} = 0$ , $N_W = 1$						
162	250–350	426	0.029±0.003	0.708	0.041	12.41±1.31
163	350–550	110	0.017±0.003	0.659	0.026	1.85±0.41
164	$\geq 550$	12	0.027±0.013	0.730	0.037	0.32±0.18
high $\Delta m$ , $N_b \geq 3$ , $M_T(b_{1,2}, \cancel{E}_T) \geq 175$ GeV, $N_t = 0$ , $N_{\text{res}} = 1$ , $N_W = 0$ , $H_T < 1000$						
165	250–350	373	0.222±0.009	0.715	0.310	82.74±5.40
166	350–550	93	0.201±0.017	0.682	0.295	18.73±2.52
167	$\geq 550$	8	0.213±0.067	0.737	0.289	1.70±0.81
high $\Delta m$ , $N_b \geq 3$ , $M_T(b_{1,2}, \cancel{E}_T) \geq 175$ GeV, $N_t = 0$ , $N_{\text{res}} = 1$ , $N_W = 0$ , $1000 \leq H_T < 1500$						
168	250–350	41	0.162±0.020	0.645	0.251	6.65±1.33
169	350–550	13	0.152±0.025	0.603	0.252	1.98±0.63
170	$\geq 550$	1	0.152±0.057	0.735	0.207	0.15±0.16
high $\Delta m$ , $N_b \geq 3$ , $M_T(b_{1,2}, \cancel{E}_T) \geq 175$ GeV, $N_t = 0$ , $N_{\text{res}} = 1$ , $N_W = 0$ , $H_T \geq 1500$						
171	250–350	12	0.114±0.035	0.722	0.158	1.37±0.57
172	350–550	4	0.084±0.032	0.532	0.157	0.33±0.21
173	$\geq 550$	3	0.281±0.132	0.697	0.402	0.84±0.63
high $\Delta m$ , $N_b \geq 3$ , $M_T(b_{1,2}, \cancel{E}_T) \geq 175$ GeV, $N_t = 1$ , $N_{\text{res}} = 0$ , $N_W = 1$						
174	$\geq 250$	548	0.001±0.000	0.697	0.001	0.29±0.13
high $\Delta m$ , $N_b \geq 3$ , $M_T(b_{1,2}, \cancel{E}_T) \geq 175$ GeV, $N_t = 1$ , $N_{\text{res}} = 1$ , $N_W = 0$						
175	250–350	426	0.005±0.001	0.708	0.007	2.09±0.47
176	$\geq 350$	122	0.012±0.003	0.666	0.017	1.41±0.37
high $\Delta m$ , $N_b \geq 3$ , $M_T(b_{1,2}, \cancel{E}_T) \geq 175$ GeV, $N_t = 0$ , $N_{\text{res}} = 1$ , $N_W = 1$						
177	$\geq 250$	548	0.001±0.000	0.697	0.002	0.67±0.25
high $\Delta m$ , $N_b \geq 3$ , $M_T(b_{1,2}, \cancel{E}_T) \geq 175$ GeV, $N_t = 2$ , $N_{\text{res}} = 0$ , $N_W = 0$						
178	$\geq 250$	548	0.001±0.000	0.697	0.001	0.32±0.16
high $\Delta m$ , $N_b \geq 3$ , $M_T(b_{1,2}, \cancel{E}_T) \geq 175$ GeV, $N_t = 0$ , $N_{\text{res}} = 0$ , $N_W = 2$						
179	$\geq 250$	548	0.000±0.000	0.697	0.000	0.00±0.00
high $\Delta m$ , $N_b \geq 3$ , $M_T(b_{1,2}, \cancel{E}_T) \geq 175$ GeV, $N_t = 0$ , $N_{\text{res}} = 2$ , $N_W = 0$						
180	250–350	426	0.006±0.001	0.708	0.008	2.55±0.48
181	$\geq 350$	122	0.006±0.002	0.666	0.009	0.72±0.25
high $\Delta m$ , $N_b \geq 3$ , $M_T(b_{1,2}, \cancel{E}_T) \geq 175$ GeV, $(N_t + N_{\text{res}} + N_W) \geq 3$						
182	$\geq 250$	548	0.000±0.000	0.697	0.000	0.00±0.00

Table 5.4 : The LL estimate in the various high  $\Delta m$  search regions, 135–182, using the 136.7  $\text{fb}^{-1}$  dataset.

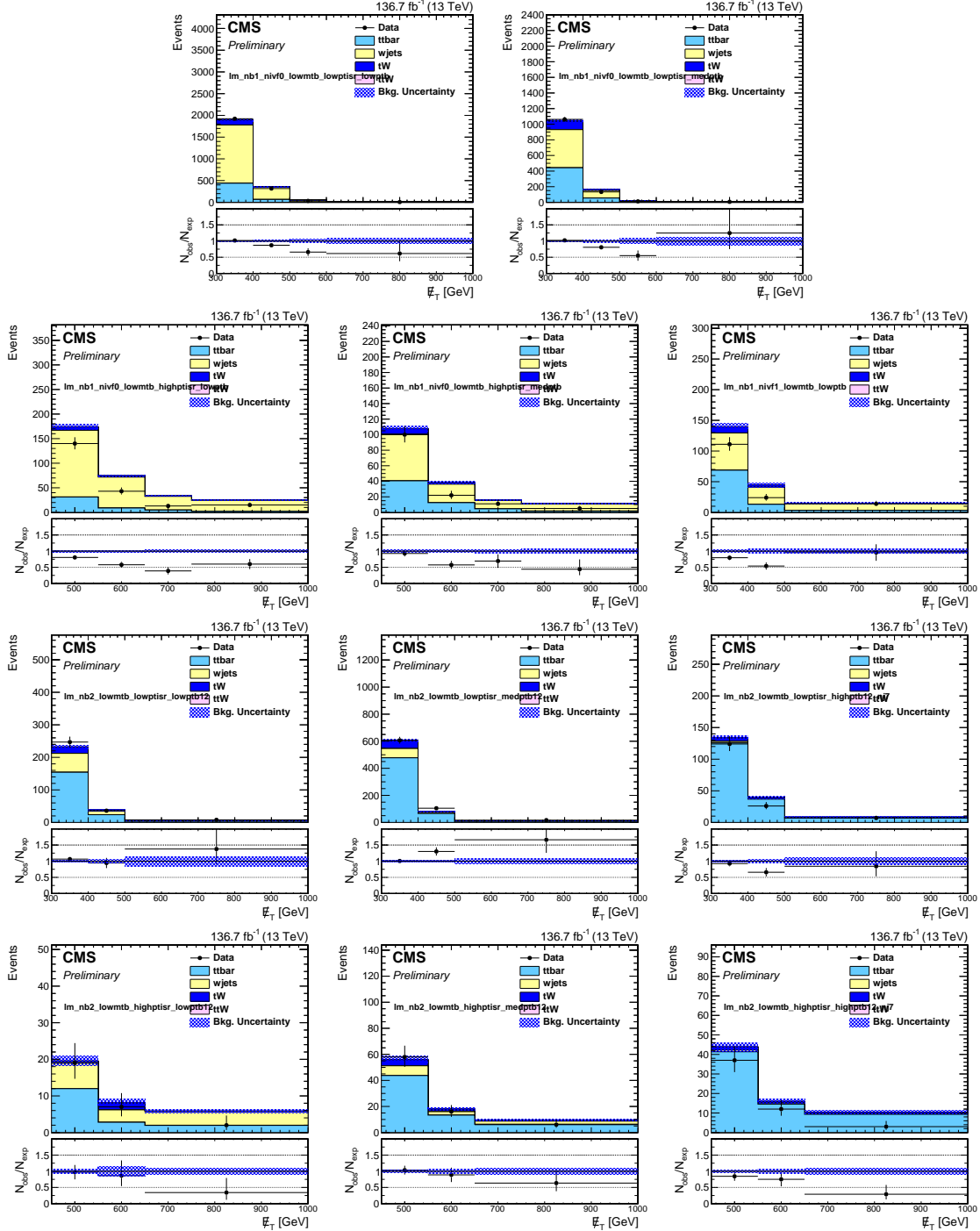


Figure 5.8 : Comparison of the  $\cancel{E}_T$  distribution in the single-lepton sample after applying the low  $\Delta m$  baseline selection. Two top rows: Events with  $N_b = 1$ ; Two bottom rows: Events with  $N_b \geq 2$ ; Data and simulation are represented by the black points and stacked histograms, respectively. The error bars on the ratio of observed data to simulation correspond to the data statistical uncertainty and the shaded blue band represents the statistical uncertainty on the simulation. These regions are included with the search regions in the simultaneous fit for the signal extraction in order to estimate the LL contribution.

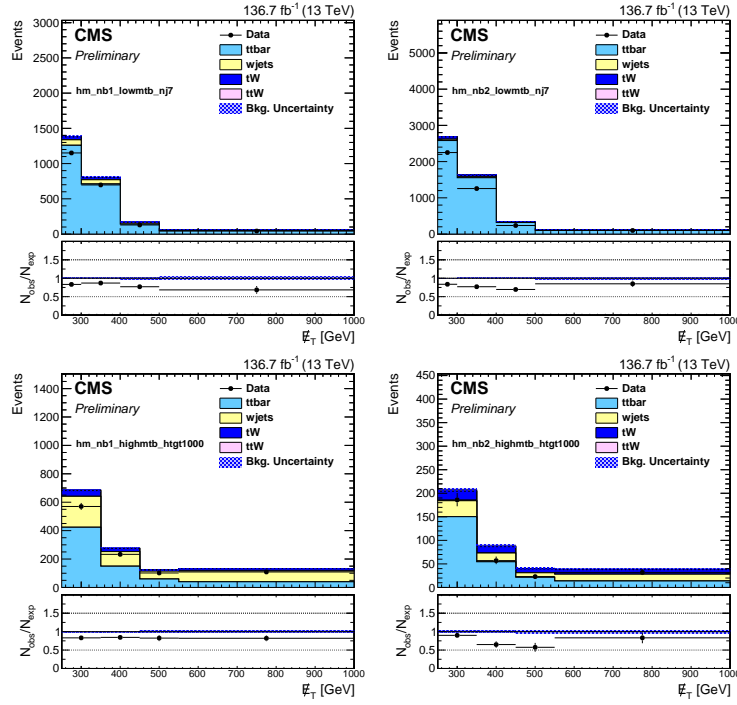


Figure 5.9 : Comparison of the  $\cancel{E}_T$  distribution in the single-lepton sample after applying the high  $\Delta m$  baseline selection in the  $M_T(b_{1,2}, \cancel{E}_T) < 175$  GeV and  $N_t = 0$ ,  $N_{res} = 0$ , and  $N_W = 0$  region. Data and simulation are represented by the black points and stacked histograms, respectively. The error bars on the ratio of observed data to simulation correspond to the data statistical uncertainty and the shaded blue band represents the statistical uncertainty on the simulation. These regions are included with the search regions in the simultaneous fit for the signal extraction in order to estimate the LL contribution.

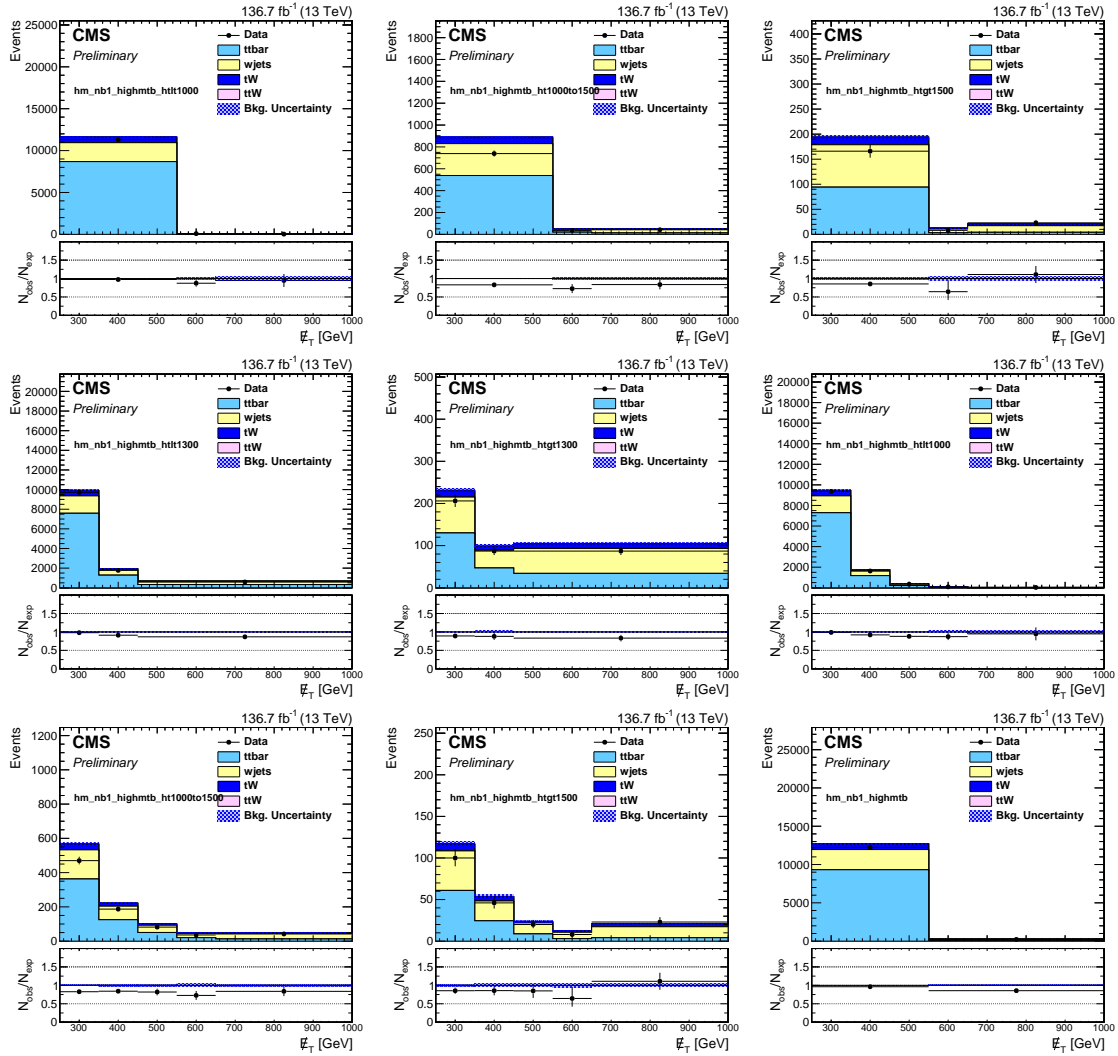


Figure 5.10 : Comparison of the  $\cancel{E}_T$  distribution in the single-lepton sample after applying the high  $\Delta m$  baseline selection in the  $N_b = 1$  region where there are  $\geq 1$  heavy object tags. Data and simulation are represented by the black points and stacked histograms, respectively. The error bars on the ratio of observed data to simulation correspond to the data statistical uncertainty and the shaded blue band represents the statistical uncertainty on the simulation. These regions are included with the search regions in the simultaneous fit for the signal extraction in order to estimate the LL contribution.

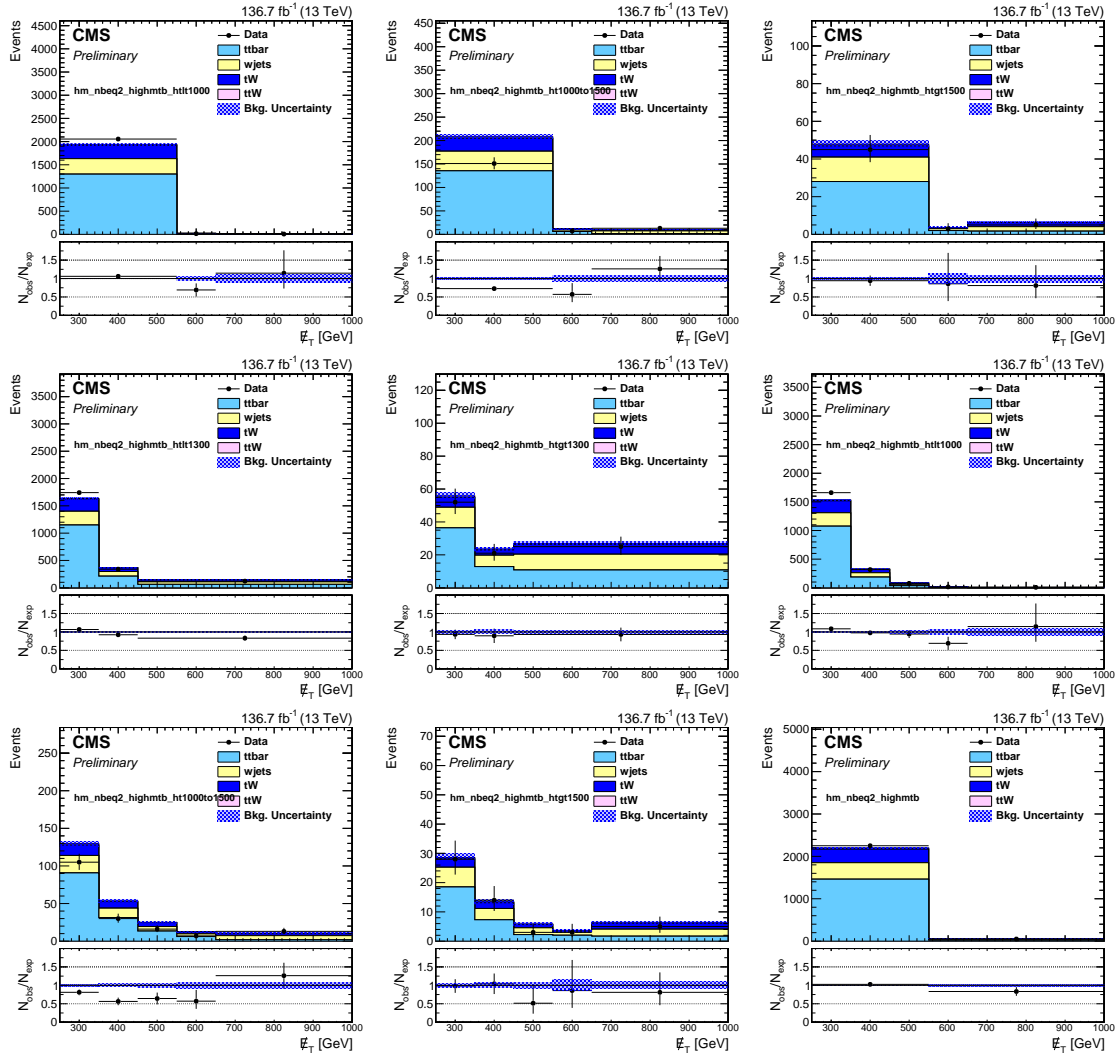


Figure 5.11 : Comparison of the  $\cancel{E}_T$  distribution in the single-lepton sample after applying the high  $\Delta m$  baseline selection in the  $N_b = 2$  and  $N_t = 1$ ,  $N_{res} = 1$ , or  $N_W = 1$  regions. Data and simulation are represented by the black points and stacked histograms, respectively. The error bars on the ratio of observed data to simulation correspond to the data statistical uncertainty and the shaded blue band represents the statistical uncertainty on the simulation. These regions are included with the search regions in the simultaneous fit for the signal extraction in order to estimate the LL contribution.

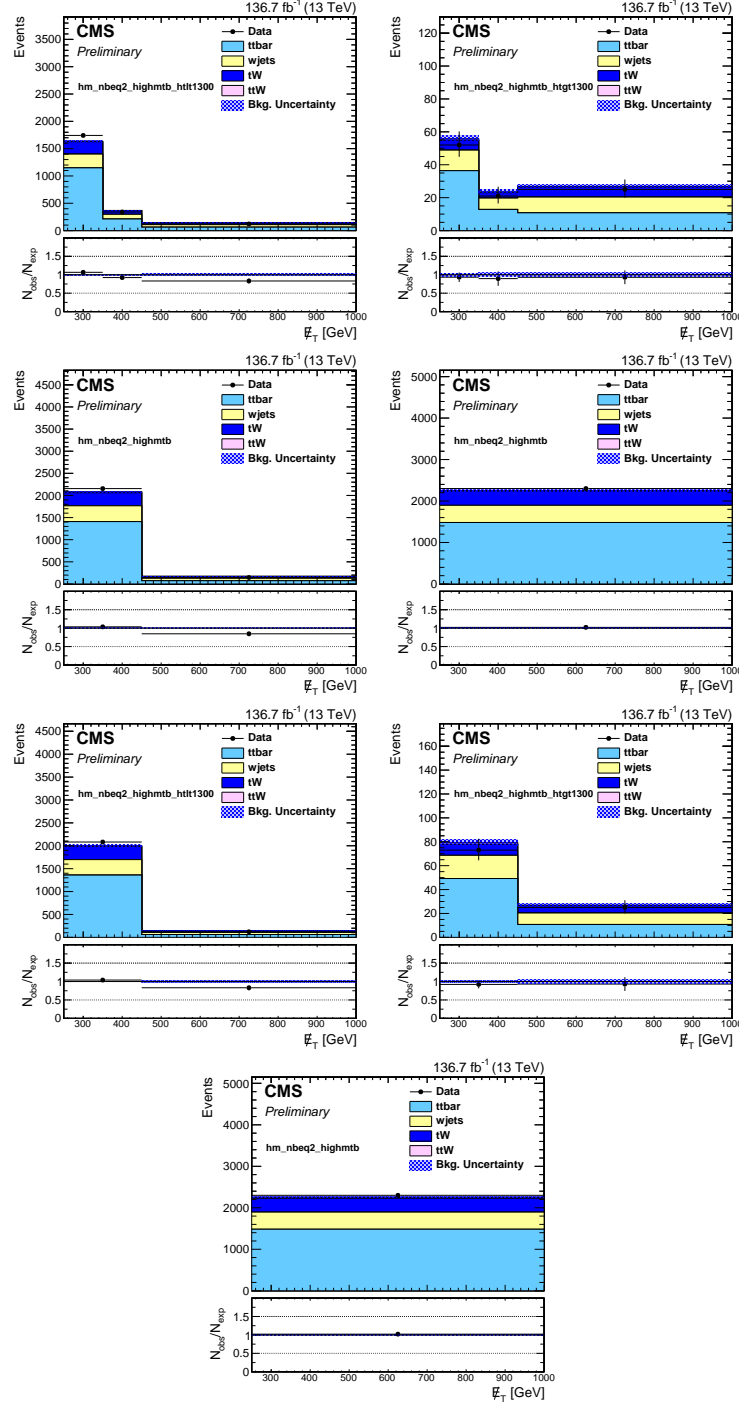


Figure 5.12 : Comparison of the  $\cancel{E}_T$  distribution in the single-lepton sample after applying the high  $\Delta m$  baseline selection in the  $N_b = 2$  and  $N_t = 2, N_{res} = 2$ , or  $N_W = 2$  region. Data and simulation are represented by the black points and stacked histograms, respectively. The error bars on the ratio of observed data to simulation correspond to the data statistical uncertainty and the shaded blue band represents the statistical uncertainty on the simulation. These regions are included with the search regions in the simultaneous fit for the signal extraction in order to estimate the LL contribution.

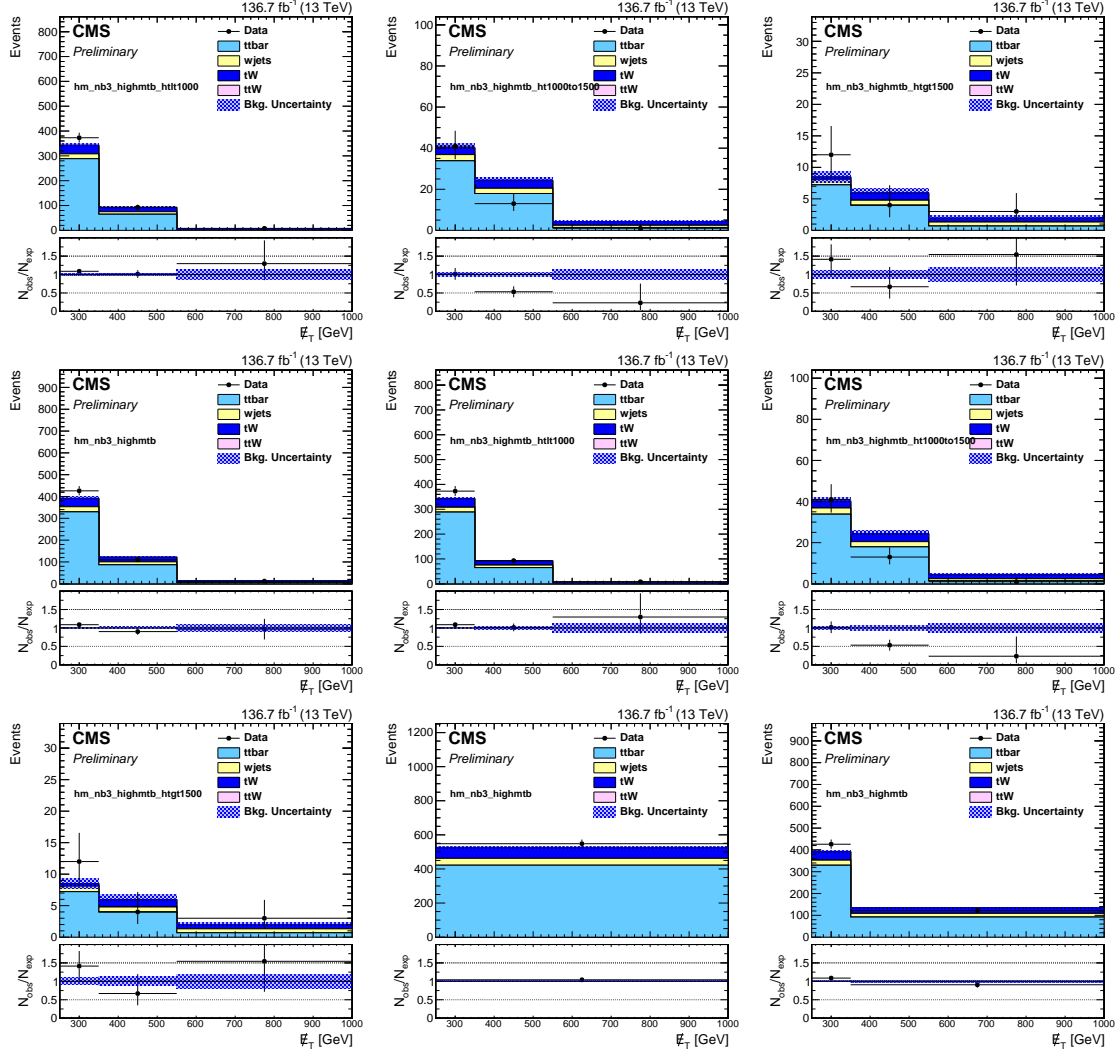


Figure 5.13 : Comparison of the  $\cancel{E}_T$  distribution in the single-lepton sample after applying the high  $\Delta m$  baseline selection in the  $N_b \geq 3$  and  $N_t = 1, N_{\text{res}} = 1$ , or  $N_W = 1$  region. Data and simulation are represented by the black points and stacked histograms, respectively. The error bars on the ratio of observed data to simulation correspond to the data statistical uncertainty and the shaded blue band represents the statistical uncertainty on the simulation. These regions are included with the search regions in the simultaneous fit for the signal extraction in order to estimate the LL contribution.

## 5.4 Z Boson Decay to Neutrinos

An important source of background for the zero-lepton search is from events in which a  $Z$  boson, produced in association with jets, decays to neutrinos that result in a significant amount of missing energy in the event. Two methods are traditionally used to estimate the  $Z \rightarrow \nu\nu$  background. The first method makes use of a sample dominated by  $Z \rightarrow ll + \text{jets}$  events. This approach comes with the advantage of very similar kinematics (after correcting for the difference in acceptance between charged lepton pairs and pairs of neutrinos), but is statistically limited, especially in the tight search regions used in SUSY searches. The second method utilizes a  $\gamma + \text{jets}$  sample. The  $\gamma + \text{jets}$  process has a factor of 5 or more larger cross section than the  $Z \rightarrow ll + \text{jets}$  process, and has similar leading order Feynman diagrams to  $Z + \text{jets}$  events. However, there are two main differences between the two processes that must be taken into account, namely, different quark-boson couplings and the fact that the  $Z$  boson is very massive. Both of these effects become less important with higher boson  $p_T$ , which is the kinematic region we are probing with this search. The  $\cancel{E}_T$  of the  $\gamma + \text{jets}$  process is calculated after removing the photon from the event to mimic the  $Z \rightarrow \nu\nu$  process.

Based on the above, we use a hybrid method to estimate the  $Z \rightarrow \nu\nu$  background that makes use of both the  $\gamma + \text{jets}$  and the  $Z \rightarrow ll + \text{jets}$  processes. The photon and the dilepton system are removed from the events before calculating  $\cancel{E}_T$  and other kinematic variables related to  $\cancel{E}_T$ , and the modified  $\cancel{E}_T$  is denoted by  $\cancel{E}_T^\gamma$  and  $\cancel{E}_T^{ll}$  for  $\gamma + \text{jets}$  and the  $Z \rightarrow ll + \text{jets}$  processes, respectively. We utilize the  $Z \rightarrow ll + \text{jets}$  sample to measure the normalization of the  $Z \rightarrow \nu\nu$  process in different ranges of  $N_b$  and  $N_{SV}$ , and we take advantage of the much higher statistics of the  $\gamma + \text{jets}$  sample to extract shape corrections. As discussed in Sec. 5.3, the good agreement

we observe between data and simulation in the Lost Lepton background leads us to integrate the control regions used in the estimation of the  $Z \rightarrow \nu\nu$  background in the number of  $t$  and  $W$  tags to increase the statistical power of the prediction. We then extrapolate into tagged regions using simulation, corrected with the appropriate  $t$  and  $W$  tagging data-to-simulation scale factors.

The prediction of the  $Z \rightarrow \nu\nu$  background is given by:

$$N_{pred}^{Z \rightarrow \nu\nu} = N_{MC}^{Z \rightarrow \nu\nu} \cdot R_Z \cdot S_\gamma \quad (5.4)$$

Znunu: production of a Z boson that decays into two neutrinos which are then missed by the detector. Can have jets from other quarks/gluons in the interaction

## 5.5 Quantum Chromodynamic Events

Simulation predicts negligible levels of QCD contamination in the various search regions. However, the QCD multijet simulation has limited statistics and there are uncertainties related to the description of physics in the simulation, particularly for the rare scenarios that would lead to a multijet event passing all of the final search region selection criteria. For these reasons, it is necessary to perform a data-driven QCD background estimation. We follow an approach similar to those described for other SM backgrounds, first using a QCD-enhanced region to validate the simulation, then extrapolating the event count in the control region to a prediction in the search region.

$\cancel{E}_T$  is generated in QCD events through either jet  $p_T$  mis-measurement or semileptonic heavy flavor decay and for the purposes of this section both sources of  $\cancel{E}_T$  will be generally referred to as "mis-measurement". This leads to the characteristic of  $\cancel{E}_T$  being aligned to one of the leading jets, which motivates including a veto on

such events in the baseline selection. On the other hand, inverting and tightening the  $\Delta\phi_{1234} \geq 0.5$  selection from the high  $\Delta m$  region, or the  $|\Delta\phi(j_1, \cancel{E}_T)| \geq 0.5$ ,  $|\Delta\phi(j_{2,3}, \cancel{E}_T)| \geq 0.15$  selection from the low  $\Delta m$  region, to  $\Delta\phi_{123} < 0.1$  for both the high and low  $\Delta m$  regions result in regions with fairly pure samples of QCD events. The QCD search regions yields are estimated with data yields in a series of control regions with this modified baseline selection after subtracting the contamination of non-QCD processes. The control region yields are related to search region yields with the following simulation transfer factors:

$$TF_{QCD} = \frac{N_{MC}^{QCD}(SR)}{N_{MC}^{QCD}(\Delta\phi_{123} < 0.1)} \quad (5.5)$$

where  $N_{MC}^{QCD}(SR)$  are the expected QCD yields from simulation for the signal regions, ( $\Delta\phi_{1234} \geq 0.5$  for high  $\Delta m$  and  $|\Delta\phi(j_1, \cancel{E}_T)| \geq 0.5$ ,  $|\Delta\phi(j_{2,3}, \cancel{E}_T)| \geq 0.15$  for low  $\Delta m$ ) and  $N_{MC}^{QCD}(\Delta\phi_{123} < 0.1)$  is the expected QCD yield from simulation for the control region. The QCD estimate,  $N_{pred}^{QCD}$ , is defined as:

$$N_{pred}^{QCD} = TF_{QCD} \cdot (N_{data} - N_{MC}^{non-QCD}), \quad (5.6)$$

where  $N_{data}$  is the number of events in the  $\Delta\phi_{123} < 0.1$  control sample described above, and  $N_{MC}^{non-QCD}$  is the number of non-QCD events in this sample as estimated by the background predictions.

For the estimation of the QCd contribution in the high  $\Delta m$  search regions, the QCD control regions match the selection in the corresponding search regions except from the selection on  $N_t$ ,  $N_W$ , and  $N_{res}$ . Binning the control regions in these dimensions has the advantage of measureming the efficiency of each variable directly in data. The  $t$  and  $W$  tags improves significantly the statistical power of the esti-

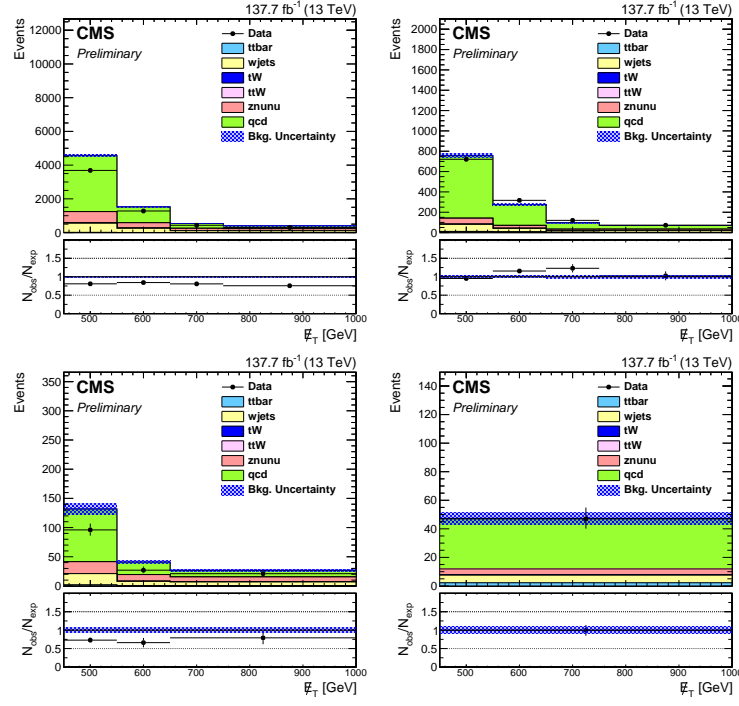


Figure 5.14 : Comparison of the  $\cancel{E}_T$  distribution in the QCD multijet sample after applying the low  $\Delta m$  baseline selection in the  $N_b = 0$  region. Data and simulation are represented by the black points and stacked histograms, respectively. The error bars on the ratio of observed data to simulation correspond to the data statistical uncertainty and the shaded blue band represents the statistical uncertainty on the simulation. These regions are included with the search regions in the simultaneous fit for the signal extraction in order to estimate the QCD contribution.

mate. The lepton vetoes are not applied when calculating  $TF_{QCD}$ , only on  $N_{data}$  and  $N_{MC}^{non-QCD}$ . The fake rates are then estimated directly from data.

A similar approach is utilized for the estimation of the QCD contribution in the low  $\Delta m$  search regions. The QCD control regions are binned in the same variables and ranges as of the search regions, but the QCD purity is low for the low  $\Delta m$  control regions with one or more b-tags (the high  $\Delta m$  control regions are integrated

with respect to top and  $W$ -tags and therefore have sufficient statistics in spite of the number of b-tags). Except for a normalization factor, the MC is generally consistent with data as function of  $\cancel{E}_T$  for each of the control regions. Therefore, these low  $\Delta m$  control region  $\cancel{E}_T$  bins are combined in order to increase the precision of the prediction in these search region bins. A systematic uncertainty on this integration is obtained by comparing the MC  $\cancel{E}_T$  shape to the data shape for the two  $N_b = 0$  control regions in which no integration is applied. For each control region, the data to MC ratio for each  $\cancel{E}_T$  bin is compared to the fully integrated ratio. The maximum difference, 51% is the systematic uncertainty.

QCD events fail the  $\Delta\phi_{1234} \geq 0.5$  or  $|\Delta\phi(j_1, \cancel{E}_T)| \geq 0.5$ ,  $|\Delta\phi(j_{2,3}, \cancel{E}_T)| \geq 0.15$  selection cuts, for the high and low  $\Delta m$  regions respectively, and enter the search region due to a leading jet undergoing such severe mis-measurement that it is reconstructed as one of the sub-leading jets. Mis-measurement is parameterized by the jet response, defined as:

$$r_{jet} = \frac{(p_T)_{reco}}{(p_T)_{gen}}. \quad (5.7)$$

A much larger proportion of events in the search region than the control region are in the tail of the  $r_{jet}$  distribution, which means that this method relies on the correct modeling of  $r_{jet}$  in simulation. Therefore, a  $r_{jet}$  correction and uncertainty is extracted from data using the method described in Ref. [1]. The correction is derived with the pseudo jet response ( $r_{pseudo,jet}$ ) distribution, applying the QCD control region selection except for the number of jets and b-tagging requirements. We divide this region into two, in the case of the jet aligned to  $\cancel{E}_T$  passing the medium b-tag requirement and in the case of it not passing the light b-tag requirement. The corrections range between  $0.81 \pm 0.12$  and  $0.83 \pm 0.08$  in the case of jets originating from b-quarks and between  $1.04 \pm 0.04$  and  $1.82 \pm 0.15$  for all other jets as can be

seen in Table .

The statistical uncertainty on  $TF_{QCD}$  is reduced by increasing the effective luminosity of the QCD multijet sample with a method referring to as "local smearing." The method relies on the parametrization of  $r_{jet}$ , which is only dependent on jet properties.

### 5.5.0.1 QCD Local Smearing

The local smearing methods for QCD use a parameterization of the reconstructed(reco) jet. The reco jet is used when defining the jet response, see Eqn. 5.7. The analysis of the jet response spans many order of magnitude and is binned in  $p_T$  and jet flavor, see Fig. 5.21 and 5.22.

### 5.5.0.2 QCD Corrections

Figures ? and ? show the  $\cancel{E}_T$  distribution in data and simulation in the QCD control regions for the high  $\Delta m$  and lowd  $\Delta m$  selections, respectively. The stacked plot labeled "Non-QCD bkg" is the distribution of the non-QCD events as predicted with the estimation methods detailed in this note. The other stacked plot, labeled "Smeared QCD MC" is the smeared QCD simulation yield after applying the  $r_{jet}$  corrections. The other two lines show a combination of the predicted non-QCD SM yields and one of two scenarios. "Without  $r_{jet}$  corr" is the smeared QCD simulation without the  $r_{jet}$  correction and "With orig. QCD MC" is the standard QCD simulation without this correction. There are three important trends in this figure. The first is the purity of the control regions, which gives confidence in using them to predict QCD yields. The second is that the "Without  $r_{jet}$  corr" estimation is nearly equivalent to "With orig. QCD MC" in the regions where there are enough

statistics to have a meaningful comparison. This improves our confidence in the use of the smeared QCD simulation. Finally, the  $r_{jet}$  correction improves the agreement between data simulation, which is a useful validation of this correction. Due to the nature of the background estimation method applied in the high  $\Delta m$  search, control regions are utilized for the prediction of multiple search regions.

Tables ? and ? summarize the yields in data, the derived transfer factors, and the resulting QCD predictions for the high  $\Delta m$  and low  $\Delta m$  search regions respectively. The transfer factors in the high  $\Delta m$  region actually account for two levels of extrapolation, i.e., the extrapolation from the control regions to the search regions without the requirement of top and W tags, and the extrapolation in top and W tags in the search regions after correcting the top- and W-tagging efficiencies:

$$\begin{aligned} TF_{QCD} &= TF_{QCD}^{CR-SR} \times TF_{QCD}^{SR-extrap} \\ &= \frac{N_{MC}(SR)(N_j, N_b, \not{E}_T)}{N_{MC}(\Delta\phi_{123} < 0.1)(N_j, N_b, \not{E}_T)} \times \frac{N_{MC}(SR)(N_j, N_b, \not{E}_T, N_t, N_{res}, N_W)}{N_{MC}(SR)(N_j, N_b, \not{E}_T)} \end{aligned} \quad (5.8)$$

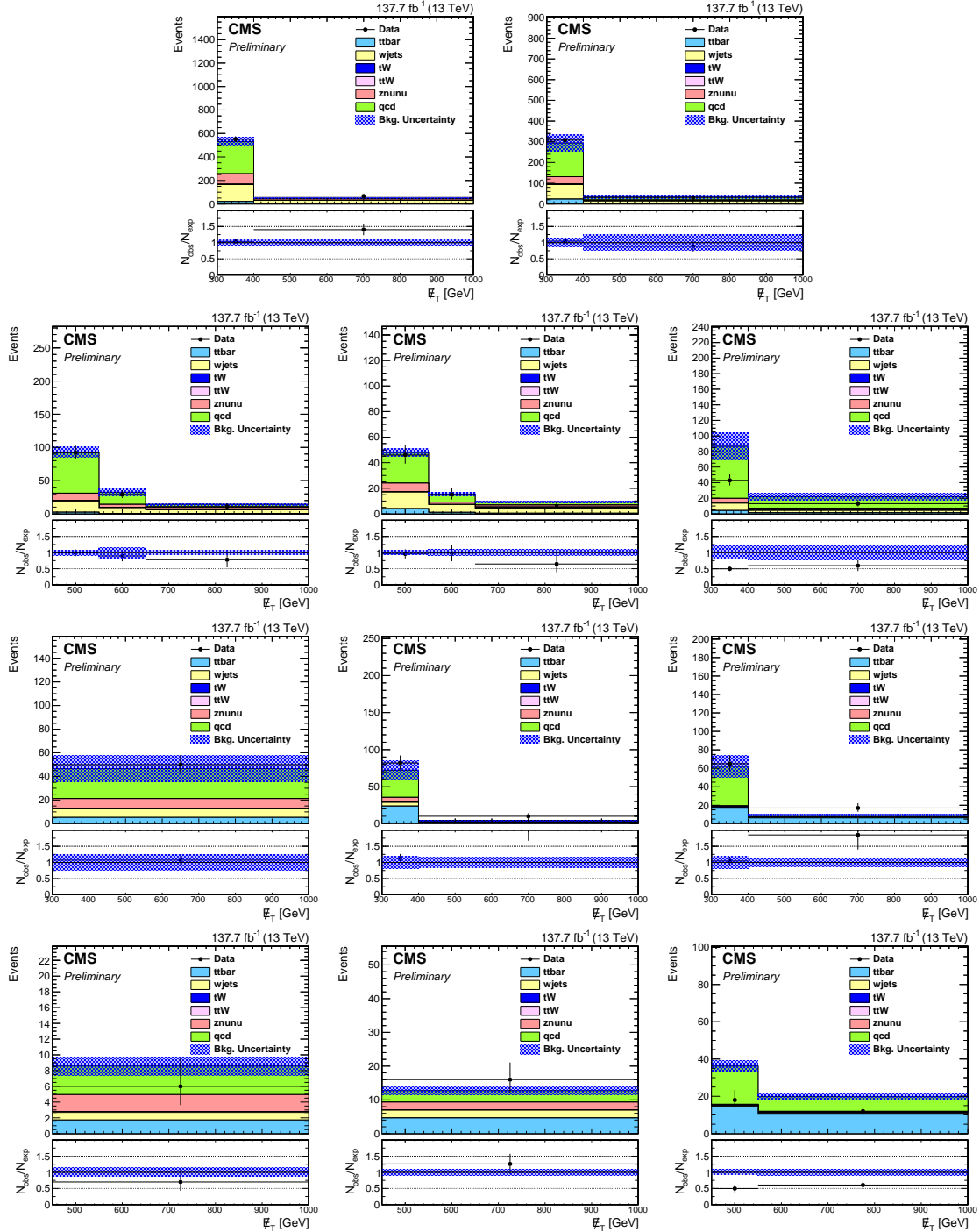


Figure 5.15 : Comparison of the  $\cancel{E}_T$  distribution in the QCD multijet sample after applying the low  $\Delta m$  baseline selection. Two top rows: Events with  $N_b = 1$ ; Two bottom rows: Events with  $N_b \geq 2$ ; Data and simulation are represented by the black points and stacked histograms, respectively. The error bars on the ratio of observed data to simulation correspond to the data statistical uncertainty and the shaded blue band represents the statistical uncertainty on the simulation. These regions are included with the search regions in the simultaneous fit for the signal extraction in order to estimate the QCD contribution.

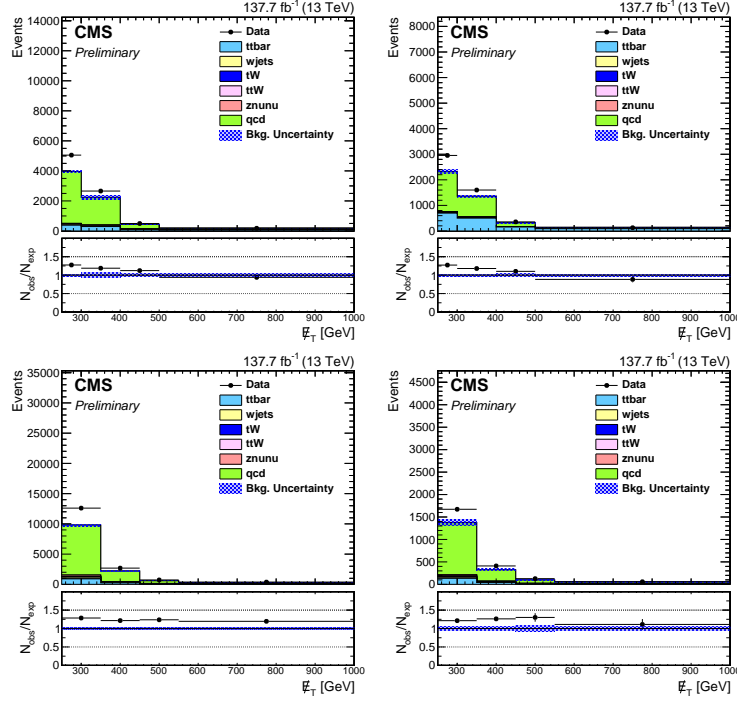


Figure 5.16 : Comparison of the  $\cancel{E}_T$  distribution in the QCD multijet sample after applying the high  $\Delta m$  baseline selection in the  $M_T(b_{1,2}, \cancel{E}_T) < 175 \text{ GeV}$  and  $N_t = 0, N_{res} = 0$ , and  $N_W = 0$  region. Data and simulation are represented by the black points and stacked histograms, respectively. The error bars on the ratio of observed data to simulation correspond to the data statistical uncertainty and the shaded blue band represents the statistical uncertainty on the simulation. These regions are included with the search regions in the simultaneous fit for the signal extraction in order to estimate the QCD contribution.

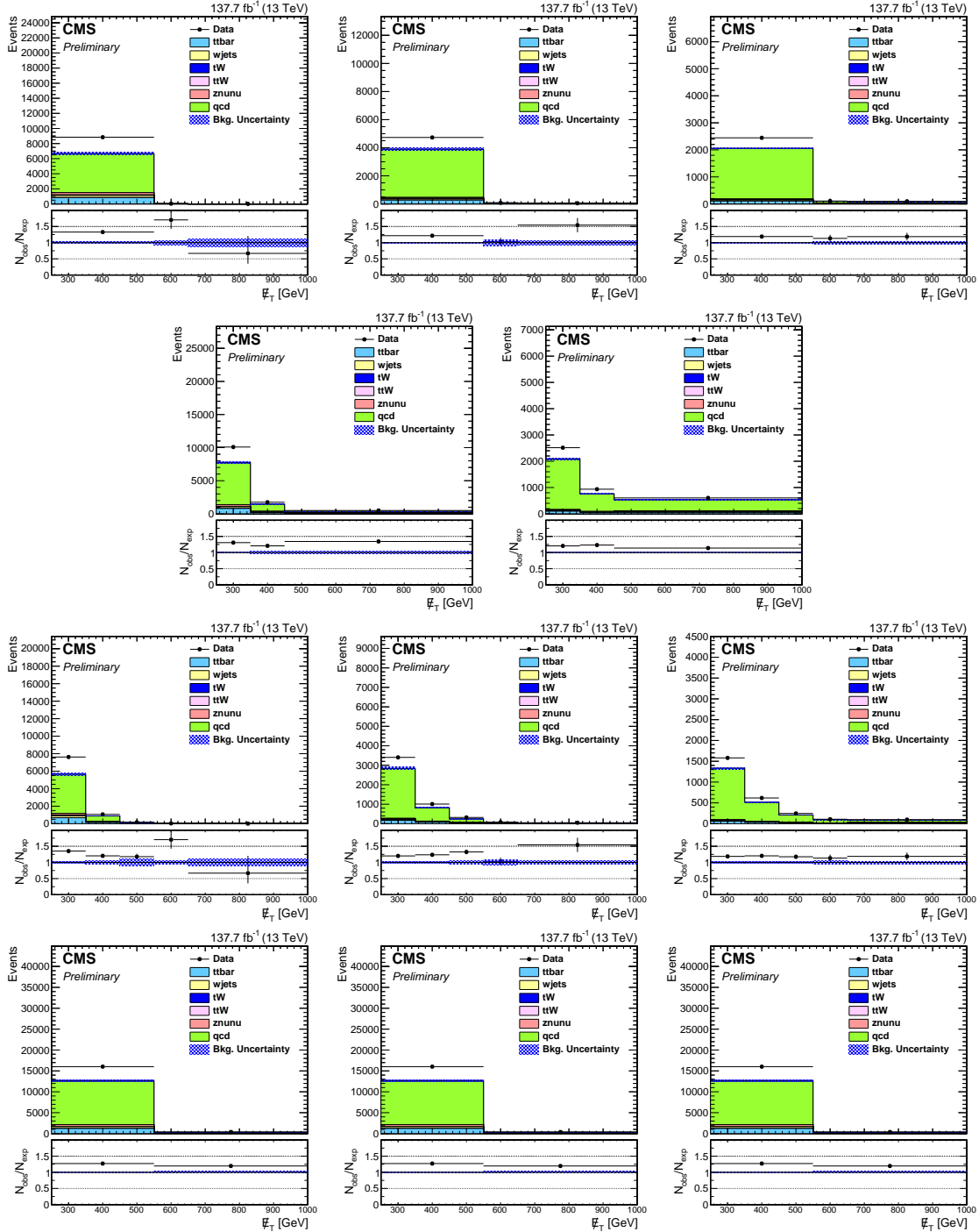


Figure 5.17 : Comparison of the  $\cancel{E}_T$  distribution in the QCD multijet sample after applying the high  $\Delta m$  baseline selection in the  $N_b = 1$  region where there are  $\geq 1$  heavy object tags. Data and simulation are represented by the black points and stacked histograms, respectively. The error bars on the ratio of observed data to simulation correspond to the data statistical uncertainty and the shaded blue band represents the statistical uncertainty on the simulation. These regions are included with the search regions in the simultaneous fit for the signal extraction in order to estimate the QCD contribution.

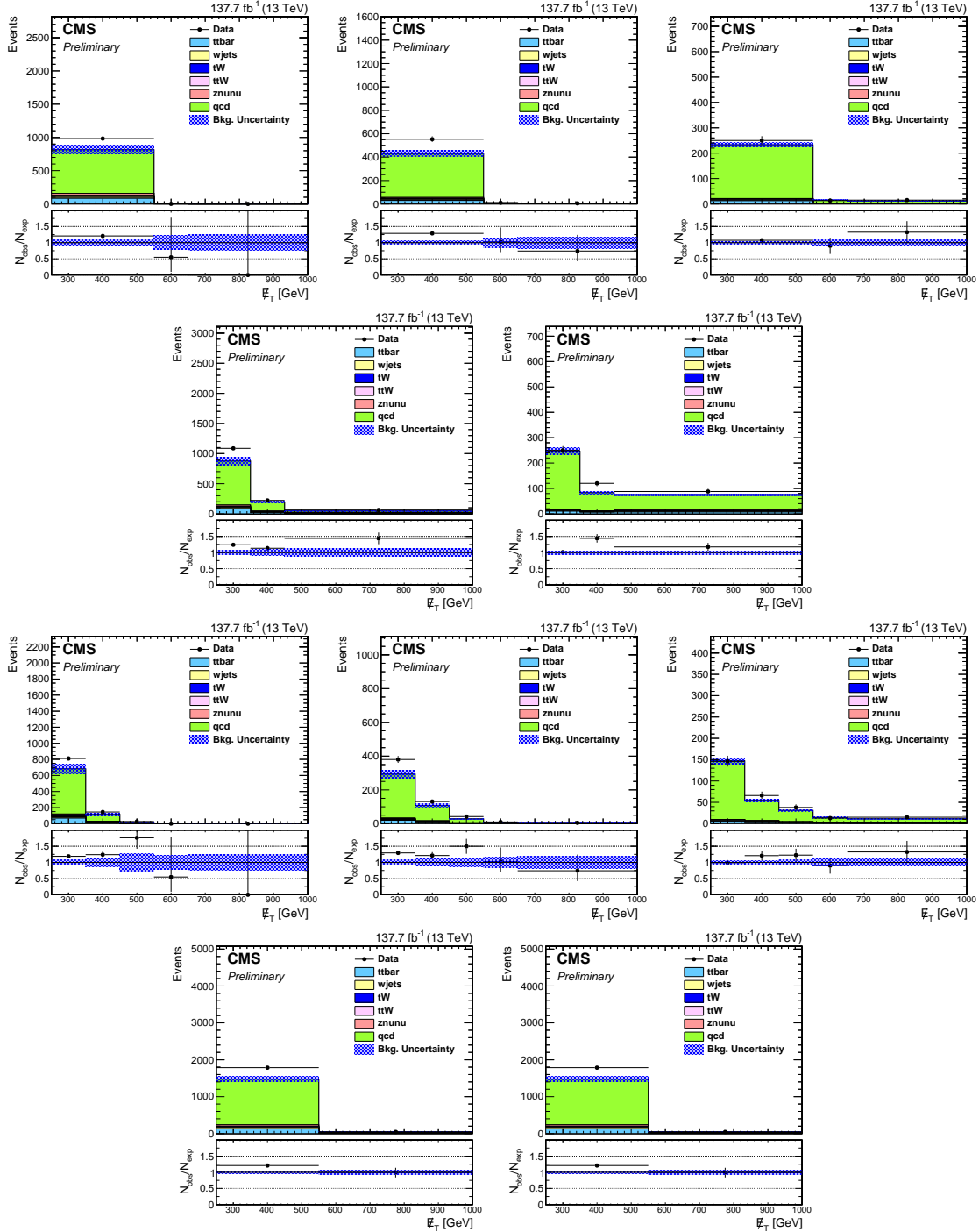


Figure 5.18 : Comparison of the  $\cancel{E}_T$  distribution in the QCD multijet sample after applying the high  $\Delta m$  baseline selection in the  $N_b = 2$  and  $N_t = 1, N_{res} = 1$ , or  $N_W = 1$  regions. Data and simulation are represented by the black points and stacked histograms, respectively. The error bars on the ratio of observed data to simulation correspond to the data statistical uncertainty and the shaded blue band represents the statistical uncertainty on the simulation. These regions are included with the search regions in the simultaneous fit for the signal extraction in order to estimate the QCD contribution.

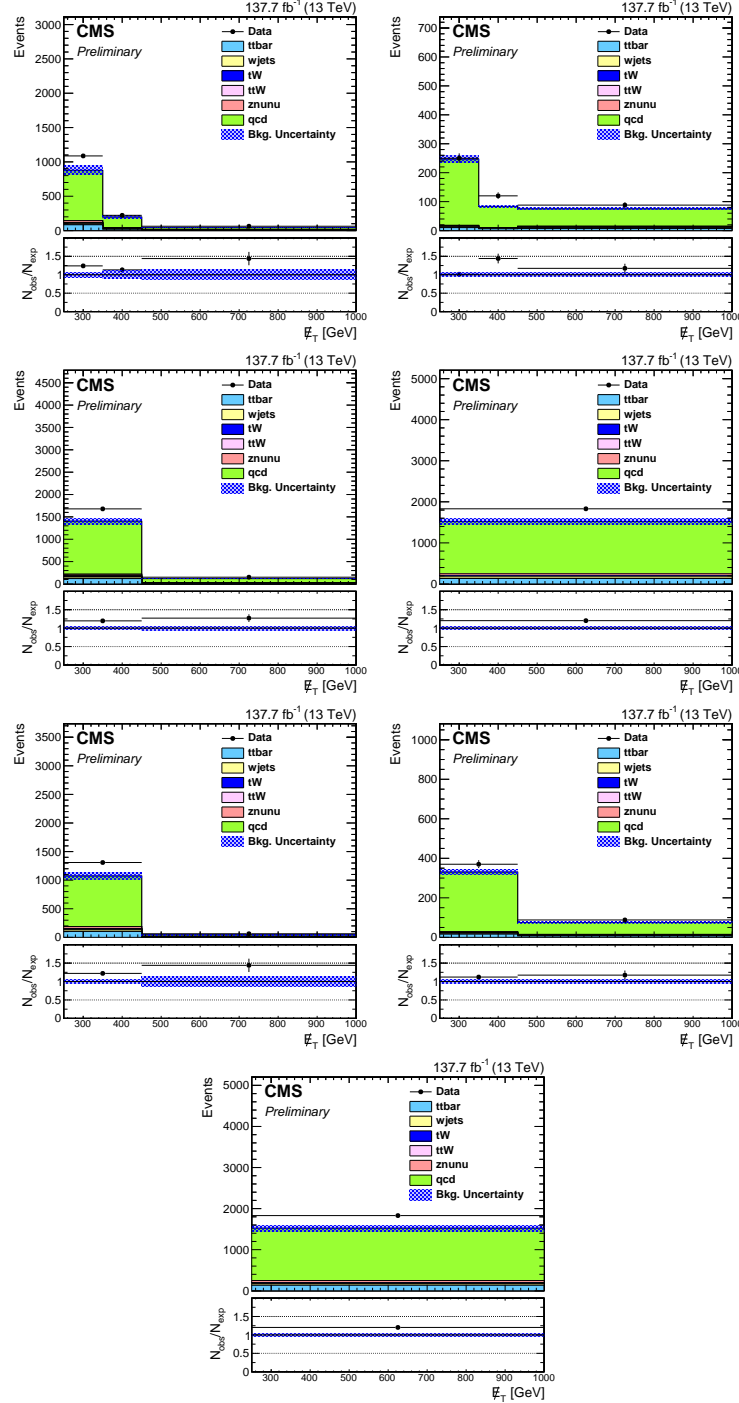


Figure 5.19 : Comparison of the  $\cancel{E}_T$  distribution in the QCD multijet sample after applying the high  $\Delta m$  baseline selection in the  $N_b = 2$  and  $N_t = 2, N_{res} = 2$ , or  $N_W = 2$  region. Data and simulation are represented by the black points and stacked histograms, respectively. The error bars on the ratio of observed data to simulation correspond to the data statistical uncertainty and the shaded blue band represents the statistical uncertainty on the simulation. These regions are included with the search regions in the simultaneous fit for the signal extraction in order to estimate the QCD contribution.

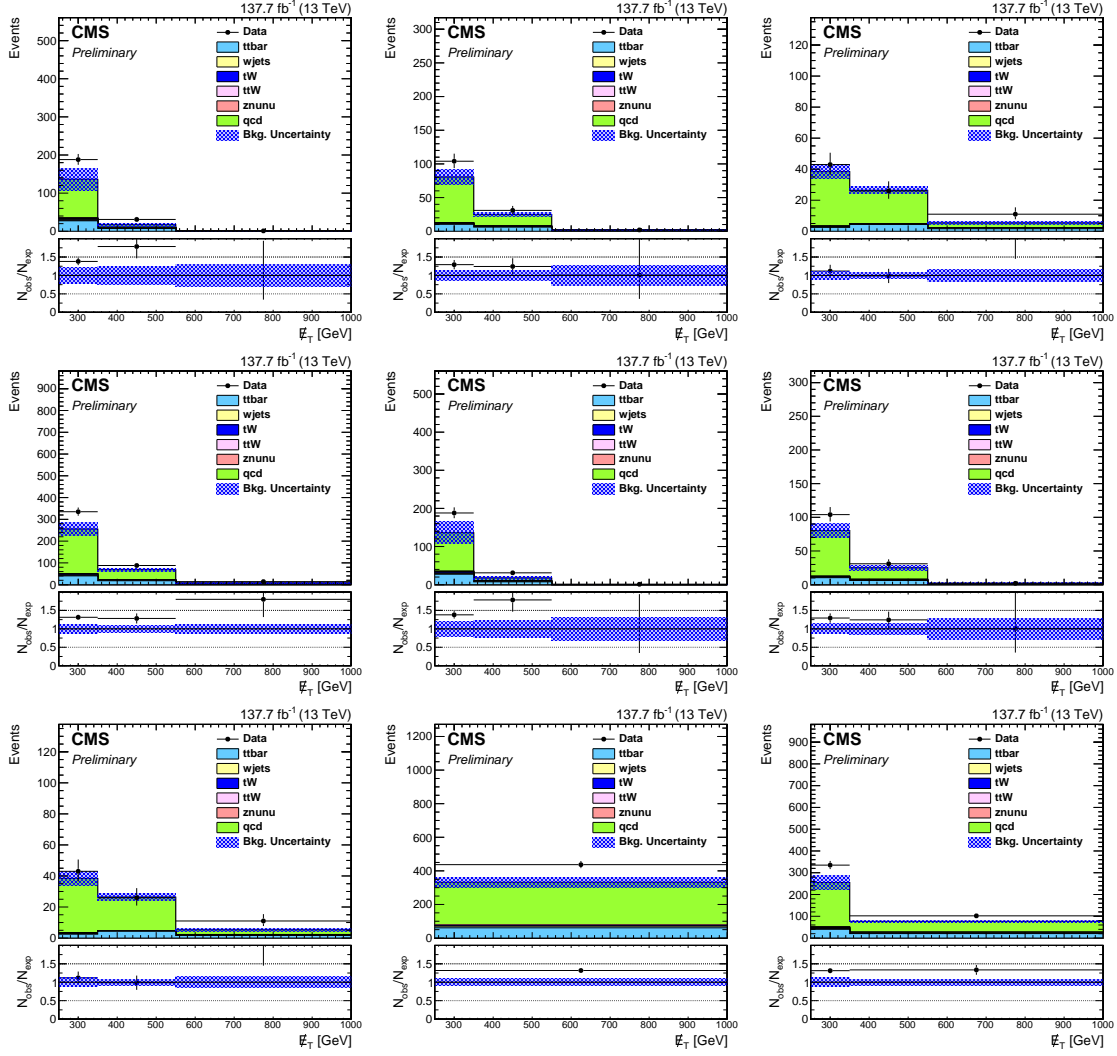


Figure 5.20 : Comparison of the  $\vec{E}_T$  distribution in the QCD multijet sample after applying the high  $\Delta m$  baseline selection in the  $N_b \geq 3$  and  $N_t = 1, N_{res} = 1$ , or  $N_W = 1$  region. Data and simulation are represented by the black points and stacked histograms, respectively. The error bars on the ratio of observed data to simulation correspond to the data statistical uncertainty and the shaded blue band represents the statistical uncertainty on the simulation. These regions are included with the search regions in the simultaneous fit for the signal extraction in order to estimate the QCD contribution.

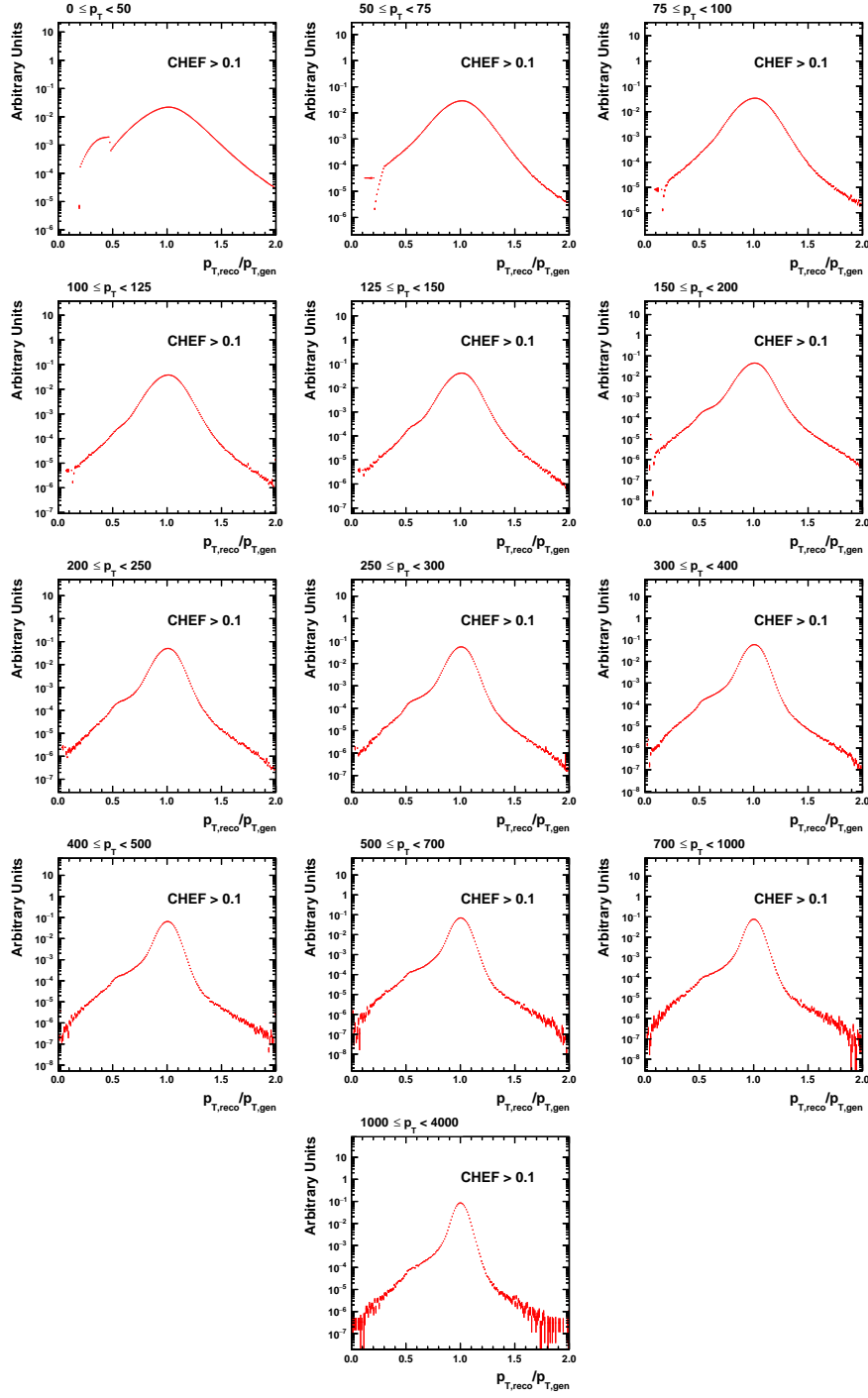


Figure 5.21 : Jet response for light tagged jets in the 2016 QCD simulation . Separated into multiple  $p_T$  bins.

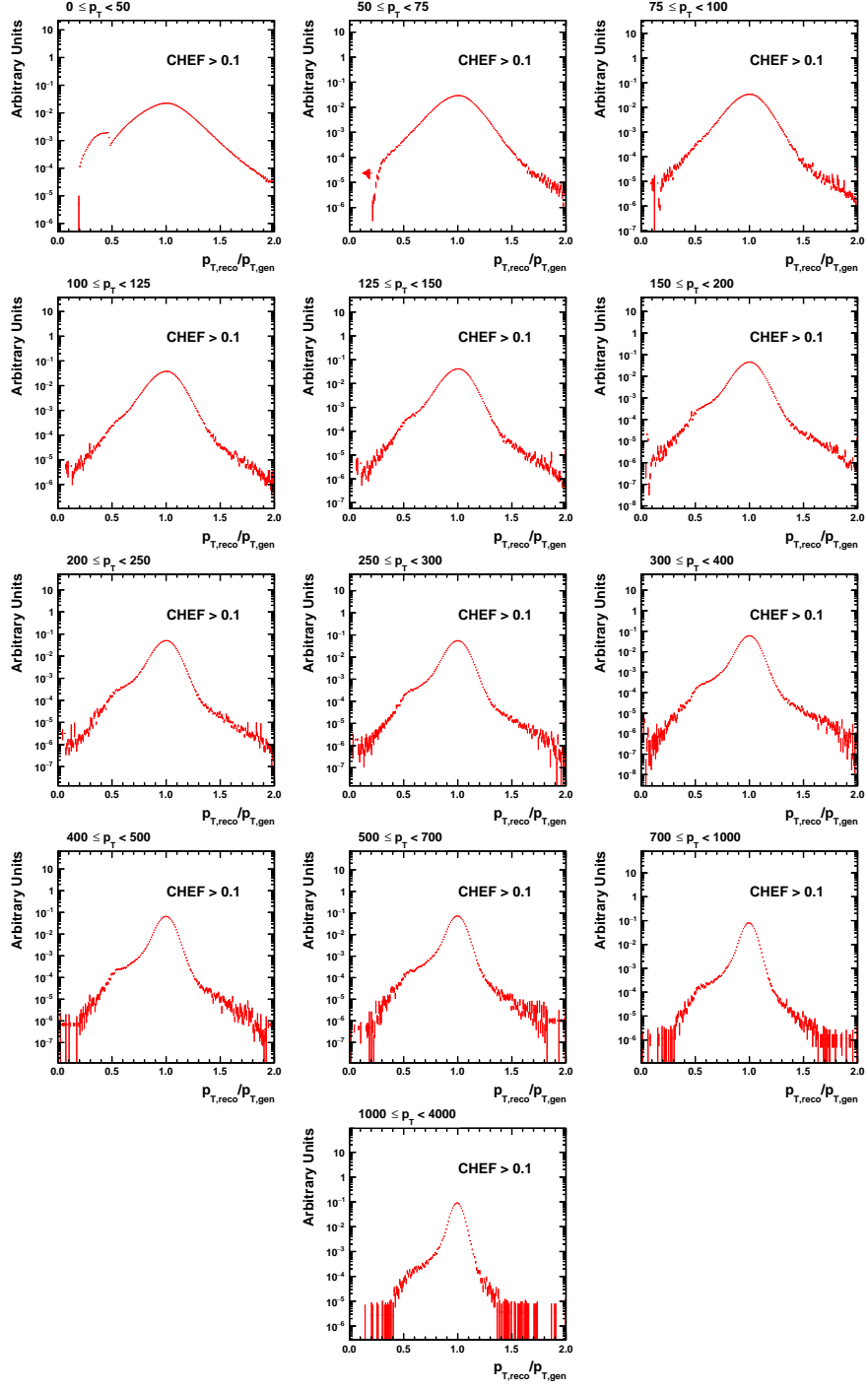


Figure 5.22 : Jet response for  $b$  tagged jets in the 2016 QCD simulation . Separated into multiple  $p_T$  bins.

## 5.6 Rare Interactions

The contributions of diboson (WW, WZ, and ZZ) processes are relatively small compared to the other backgrounds, and mainly affect the search regions targeting low  $\Delta m$  signal models. The prediction of the diboson background is obtained directly from simulation, and an uncertainty of 50% is assigned on the cross section.

The contribution of the ttZ background is also generally very small due to the rarity of this process. However, in search regions that require the presence of more than one top- or W-tagged candidates, this process can constitute a significant fraction of the total SM background due to the strong suppression of the other SM processes. In order to validate the prediction of this background, we define a three-lepton control sample, selected using single-lepton triggers, which requires the presence of exactly three electrons or muons satisfying  $p_T > 40$  GeV for the leading lepton,  $p_T > 20$  GeV for the second and third leptons, and no additional lepton with  $p_T > 10$  GeV. We further require at least five jets, at least two of which are b-tagged. A Z boson mass window of 81-101 GeV is placed on the invariant mass of the same-flavor dilepton  $p_T$  of this lepton pair is further required to be at least 100 GeV, in order to probe a kinematic region close to the one relevant for the analysis. Figure ? shows the reconstructed Z boson  $p_T$  distribution observed in this sample. We use the region outside the Z boson mass window (the  $\cancel{E}_T$  distribution in this region is also shown in Fig. ?) to simultaneously constrain the  $t\bar{t}$ background consisting of dilepton  $t\bar{t}$ events with an additional lepton originating from semi-leptonic b-hadron decay or from a misidentified jet, and obtain a scale factor of  $1.10 \pm 0.26$  for the ttZ-like processes in this sample, where the uncertainty is dominated by the statistical uncertainty in the data sample. We therefore apply an uncertainty of 24% to the normalization of the ttZ background in the analysis. In order to check the extrapolation from the lower

Z- $p_T$  region of this control sample to the search sample, we evaluate the ttZ scale factor in bins of reconstructed Z boson  $p_T$  as far as statistics permit. The  $p_T$ -binned scale factors are found to be consistent with the inclusive scale factor evaluated for  $p_T(Z) > 100$  GeV (Fig. sldkjf). Additional experimental and theoretical uncertainties related to PDF and factorization/renormalization scale variations are also assigned. Figure ? shows the number of top- and W-tagged events observed in the ttZ control sample.

## Chapter 6

# Uncertainties and Estimation

We now have a robust method for the prediction of SM background for our search for the top squark. Along with a prediction for each of the backgrounds, we need to include the systematics uncertainties for our methods. Once we incorporate them we can confirm that our methods are correct by looking at the validation regions. Finally, we can then compare the final comparisons of data-to-simulation in our SR, which will allow us to set limits on the top squark mass.

### 6.1 Systematic Uncertainties

We will look at the various categories of systematic uncertainties that can affect the analysis.

- **Statistical uncertainty of control regions in data:** The dominant uncertainty in data-driven background prediction methods is generally the result of limited statistics of the control regions that are used to derive the background estimate for the signal regions.
- **Statistical uncertainty of simulated samples:** In some cases, the uncertainties on transfer factors derived from simulation also have a significant statistical component due to limited statistics in the simulated samples.
- **Uncertainties related to extrapolation from control to signal regions:**

Each data-driven background estimation method relies on an extrapolation from a control region to the signal region. This leads to uncertainties specific to each method, related to the nature of the extrapolation. For instance, the LL prediction strategy uses the region with a selected lepton to estimate the background yield in the vetoes region. Appropriate correction factors are applied to both selected and vetoes regions to account for differences in the lepton selection efficiency between data and simulation. The precision of these corrections affects the uncertainty in the background estimation. For the QCD prediction, we rely on an extrapolation from the low  $\Delta\phi_{12}$  region, which is mostly in the core of the jet response distribution, to a region of high values of  $\Delta\phi_{12}$ , which is mostly in the tail of the distribution. We therefore assign an uncertainty in the QCD precision for the potential effects of severe jet mismeasurements in the jet response tails.

- **Uncertainties related to  $b$ -tagging:** Effects related to the  $b$ -tagging are estimated to impact the scale factors up to 3% for top-jets and between 5 to 10% for  $W+jets$ . Uncertainties due to the top- $p_T$  reweighting, pile-up, or matching criteria results to effect smaller than 3% for both top and  $W$  tags.
- **Uncertainties related to the merged top and  $W$ -tagging:** The impact of different effects on the determination of the scale factors are studied. One of the dominant sources is related to the description of the parton showering which results to uncertainties of 5-25% and 8-15%, for top and  $W$  tagging, respectively. Another source of systematics is due to the modeling of the  $t\bar{t}$  topology. The evaluated uncertainties range between 1-3% (1-12%) in top ( $W$ ) tagging.

- **Uncertainties related to the Resolved Top Tagging:** A similar list of the sources of systematic uncertainties is evaluated for the resolved tagger, as in the case of Merged tops. The most important sources stems from the description of the parton showering, which ranges between 8-31%. The modeling of the  $t\bar{t}$  topology can be as high as 4%, whereas potential dependence on the  $b$ -tagging results to uncertainties from 1 to 6%. Uncertainties due to the top- $p_T$  reweighting, pile-up, or matching criteria results to effect smaller than 3%.

## 6.2 Validation

In order to test and validate the background estimation strategy in data, we carry out the background estimation method in a lower  $\cancel{E}_T$  region of the zero-lepton sample that is adjacent to the search sample, "low  $\cancel{E}_T$  validation sample", and check the agreement between data and background prediction. The validation sample has significantly larger statistics than the search sample and is signal-depleted. Apart from the difference in the  $\cancel{E}_T$  selection, the search selection on the other search variables is applied to the validation sample, with an exception of the regions with more than one top- or W-tags, where relaxed selections (i.e. drop selection in  $M_T(b_{1,2}, \cancel{E}_T)$ ) are applied to gain more statistics, see Tables 6.2 and 6.1. Figures 6.1 and 6.2 displays the SM estimate and the observed data in the different validation regions. Statistical uncertainties as well as systematic uncertainties resulting from the top- and W-tagging correction in the background predictions are shown in this plot. The data agrees well with the estimated backgrounds yields within uncertainties.

Now that we have shown that the bins for the low and high  $\Delta m$  match well with data we can move to a full comparison of the data and simulation in the SR. To do this we combine the predictions from the LL,  $Z \rightarrow \nu\nu$ , QCD, and Rare backgrounds.

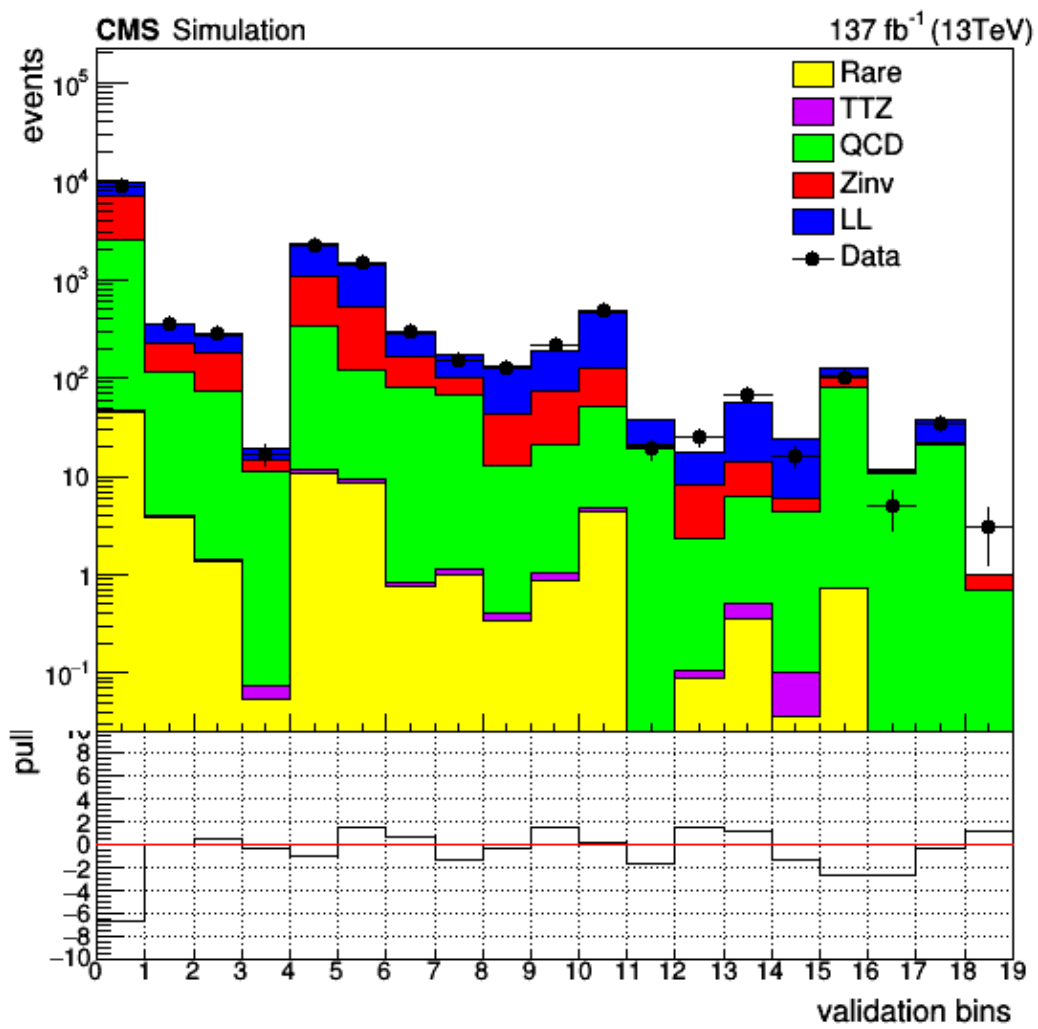


Figure 6.1 : Comparison of the data and SM backgrounds in the Low  $\Delta m$  validation regions.

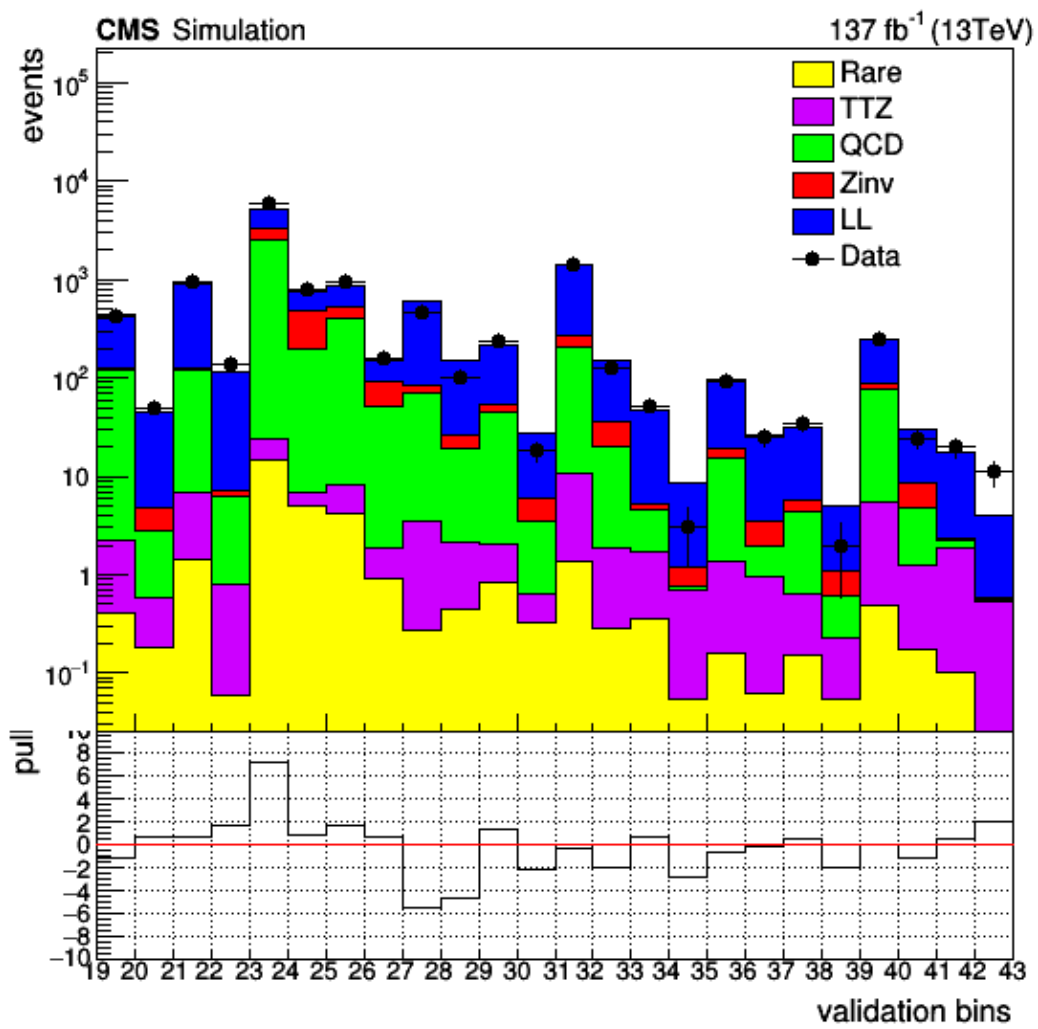


Figure 6.2 : Comparison of the data and SM backgrounds in the High  $\Delta m$  validation regions.

Table 6.1 : Summary of the 19 disjoint validation regions that mainly target low  $\Delta m$  signal models. The low  $\Delta m$  baseline selection is again  $N_j \geq 2$ ,  $\cancel{E}_T > 250$  GeV,  $N_t = N_W = N_{res} = 0$ ,  $N_b \geq 0$ ,  $M_T(b_{1,2}, \cancel{E}_T) < 175$  GeV (when applicable),  $p_T(ISR) > 200$  GeV,  $|\eta(ISR)| < 2.4$ ,  $|\Delta\phi(j_{ISR}, \cancel{E}_T)| > 2$ , and  $S_{\cancel{E}_T} > 10$ .

$N_j$	$N_b$	$N_{SV}$	$p_T(ISR)$ [GeV]	$p_T(b)$ [GeV]	$\cancel{E}_T$ [GeV]	
<hr/>						
2 – 5	0	0	$\geq 500$	-	250 – 400	
$\geq 6$		0			250 – 400	
2 – 5		$\geq 1$			250 – 400	
$\geq 6$		$\geq 1$			250 – 400	
$\geq 2$	1	0	300 – 500	20 – 40	250 – 300	
		0	300 – 500	40 – 70	250 – 300	
		0	$\geq 500$	20 – 40	250 – 400	
		0	$\geq 500$	40 – 70	250 – 400	
		$\geq 1$	$\geq 300$	20 – 40	250 – 300	
		$\geq 2$	300 – 500	40 – 80	250 – 300	
$\geq 2$	$\geq 2$		300 – 500	80 – 140	250 – 300	
			300 – 500	$\geq 140$	250 – 300	
			$\geq 500$	40 – 80	250 – 400	
			$\geq 500$	80 – 140	250 – 400	
			$\geq 300$	$\geq 140$	250 – 400	
<hr/> $0.15 \leq \Delta\phi(j_1, \cancel{E}_T) \leq 0.5,  \Delta\phi(j_{2,3}, \cancel{E}_T)  \geq 0.15$						
$\geq 2$	0	0	$\geq 200$	$\geq 20$	$\geq 250$	
$\geq 2$	0	1	$\geq 200$	$\geq 20$	$\geq 250$	
$\geq 2$	1	0	$\geq 200$	$\geq 20$	$\geq 250$	
$\geq 2$	1	1	$\geq 200$	$\geq 20$	$\geq 250$	

Table 6.2 : Summary of the 25 disjoint validation regions that mainly target high  $\Delta m$  signal models. The high  $\Delta m$  baseline selection is again  $N_j \geq 5$ ,  $\cancel{E}_T > 250 \text{ GeV}$ ,  $N_b \geq 1$ , and  $\neg \Delta\phi_{1234} < 0.5$ .

$M_T(b_{1,2}, \cancel{E}_T) < 175 \text{ GeV}$					
$N_j$	$N_b$	$N_t$	$N_W$	$N_{res}$	$\cancel{E}_T [\text{GeV}]$
$\geq 7$	$1, \geq 2$	$\geq 0$	$\geq 0$	$\geq 1$	$250 - 400, \geq 400$
$M_T(b_{1,2}, \cancel{E}_T) \geq 175 \text{ GeV}$					
$N_j$	$N_b$	$N_t$	$N_W$	$N_{res}$	$\cancel{E}_T [\text{GeV}]$
$\geq 5$	$1, \geq 2$	0	0	0	$250 - 400, \geq 400$
$\geq 5$	1	1	0	0	$250 - 400, \geq 400$
		0	1	0	$250 - 400, \geq 400$
		0	0	1	$250 - 400, \geq 400$
		$N_t + N_W + N_{res} \geq 3$			$\geq 400$
$\geq 5$	2	1	0	0	$250 - 400, \geq 400$
		0	1	0	$250 - 400, \geq 400$
		0	0	1	$250 - 400, \geq 400$
		$N_t + N_W + N_{res} \geq 3$			$\geq 400$

We need to

### 6.3 Combination of Search region

As we have seen, this analysis has quite a large parameter space of interesting mass points. This combined with the number of SR bins and different backgrounds in each bin it is necessary to discuss how we plan of combining all of this to get a final estimation. To do this we use a datacard method to perform the combination and uncertainty calculation for our counting experiment. In Fig. 6.3, we have an example of a single bin from our SR, specifically bin 61 (high  $\Delta m$ ,  $N_b = 1$ ,  $M_T(b_{1,2}, \cancel{E}_T) \geq 175$ ,  $N_t = 0$ ,  $N_{res} = 0$ ,  $N_W = 0$ ,  $H_T \geq 1000$ ,  $250 \leq \cancel{E}_T < 350$ ), for a single signal sample, T2tt(175, 1).

Let go through Fig. 6.3, so that we can understand what is going on. The parameter  $imax$  is the number of final states analyzed in the datacard,  $jmax$  is the number of independent physical processes whose yields are provided minus 1, and  $kmax$  is the number of independent systematic uncertainties. Here we put "\*" and allow the computation to figure that out. Next, we have the number of observed events from data in this particular bin, shown as *observation*, where the bin above it is a unique name. Then, in the five lines following, we have the yields for the different processes included in this bin. The first process denoted as *signal* is the yield from T2tt(175,1), then the other four processes are the SM backgrounds in this bin.

The next major portion of the datacard is the various systematics of the signal and background processes. The most common type of uncertainty is the log-normal which is denoted by *lnN*. For these, the distribution is described by the parameter  $\kappa$ , which is a multiplicative error. A  $+1\sigma$  deviation corresponds to a yield scaled by  $\kappa$  while a  $-1\sigma$  scales the yields by  $\frac{1}{\kappa}$ . If the uncertainties are small the log-normal error can be approximated by a gaussian and we can approximate  $\kappa = 1 + \frac{\delta x}{x}$ , where  $\frac{\delta x}{x}$  is the relative uncertainty of the event yield. Each process has a value for the

```

# Datacard produced by CombineHarvester with git status: analysis-HIG-16-006-freeze-080416-794-g1f6819a-dirty
imax   1 number of bins
jmax   4 number of processes minus 1
kmax   * number of nuisance parameters
-----
shapes * bin_hm_nbl_highmtb_nt0_nrt0_nw0_htgt1000_MET_pt250to350 FAKE
-----
bin      bin_hm_nbl_highmtb_nt0_nrt0_nw0_htgt1000_MET_pt250to350
observation 1.0
-----
bin_hm_nbl_highmtb_nt0_nrt0_nw0_htgt1000_MET_pt250to350 bin_hm_nbl_highmtb_nt0_nrt0_nw0_htgt1000_MET_pt250to350
bin_hm_nbl_highmtb_nt0_nrt0_nw0_htgt1000_MET_pt250to350 bin_hm_nbl_highmtb_nt0_nrt0_nw0_htgt1000_MET_pt250to350
process   signal          ttbarplusw    qcd        ttZ       diboson
process   0               1             2           3           4
rate      19.2229        1             1           0.629462  1.75324
-----
JES          lnN   -     1.02947  1.08322  1.06824  1.18889
PDF_Weight   lnN   -     -         -         1.01581  1.08331
PU_Weight    lnN   -     -         -         1.00636  0.996075
Prefire_Weight lnN   -     -         -         0.995121 0.996809
b            lnN   -     1.02107  1.00304  0.975446 1.05166
eff_e_err    lnN   -     0.986502 1.00072  -         -
eff_mu_err   lnN   -     0.999139 1.00005  -         -
mcstats_diboson_bin_hm_nbl_highmtb_nt0_nrt0_nw0_htgt1000_MET_pt250to350 lnN   -     -         -         -         1.26078
mcstats_qcd_bin_hm_nbl_highmtb_nt0_nrt0_nw0_htgt1000_MET_pt250to350 lnN   -     -         -         1.13129  -
mcstats_signal_bin_hm_nbl_highmtb_nt0_nrt0_nw0_htgt1000_MET_pt250to350 lnN   2     -         -         -         -
mcstats_ttZ_bin_hm_nbl_highmtb_nt0_nrt0_nw0_htgt1000_MET_pt250to350 lnN   -     -         -         1.12687  -
mcstats_ttbarplusw_bin_hm_nbl_highmtb_nt0_nrt0_nw0_htgt1000_MET_pt250to350 lnN   -     1.01297  -         -         -
metres        lnN   -     -         -         1.04496  0.985068
toptag_err   lnN   -     0.987468 0.998075  -         -
trigger_eff  lnN   -     -         -         1.00194  1.0018
ttZ_SF       lnN   -     -         -         1.13675  -
wtag_err     lnN   -     0.996779 0.998697  -         -
R_qcd_bin_hm_nbl_highmtb_nt0_nrt0_nw0_htgt1000_MET_pt250to350 rateParam * qcd   (@0*63.347339+@1*12.244975+@2*68.381006)
R_bin_qcdcr_hm_nbl_highmtb_ht1000to1300_MET_pt250to350,R_bin_qcdcr_hm_nbl_highmtb_ht1300to1500_MET_pt250to350,R_bin_qcdcr_hm_nbl_highmtb_htgt1500_MET_pt250to350
50
R_ttbarplusw_bin_hm_nbl_highmtb_nt0_nrt0_nw0_htgt1000_MET_pt250to350 rateParam * ttbarplusw (@0*211.606354+@1*59.934990+@2*70.115009)
R_bin_lepcr_hm_nbl_highmtb_ht1000to1300_MET_pt250to350,R_bin_lepcr_hm_nbl_highmtb_ht1300to1500_MET_pt250to350,R_bin_lepcr_hm_nbl_highmtb_htgt1500_MET_pt250to350
50

```

Figure 6.3 : An example of the datacard for a single bin of T2tt(175,1) with background and uncertainties.

```

# Datacard produced by CombineHarvester with git status: analysis-HIG-16-006-freeze-080416-794-g1f6819a-dirty
imax   1 number of bins
jmax   1 number of processes minus 1
kmax   * number of nuisance parameters
-----
shapes * bin_lepcr_hm_nbl_highmtb_ht1000to1300_MET_pt250to350 FAKE
-----
bin      bin_lepcr_hm_nbl_highmtb_ht1000to1300_MET_pt250to350
observation 457.0
-----
bin_lepcr_hm_nbl_highmtb_ht1000to1300_MET_pt250to350 bin_lepcr_hm_nbl_highmtb_ht1000to1300_MET_pt250to350
process   signal          ttbarplusw
process   0               1
rate      98.9035        563.306
-----
mcstats_signal_bin_lepcr_hm_nbl_highmtb_ht1000to1300_MET_pt250to350 lnN   1.41043  -
mcstats_ttbarplusw_bin_lepcr_hm_nbl_highmtb_ht1000to1300_MET_pt250to350 lnN   -       1.01187
R_bin_lepcr_hm_nbl_highmtb_ht1000to1300_MET_pt250to350 rateParam * ttbarplusw 1 [0.01,5]

```

Figure 6.4 : An example of the datacard for the LL CR with signal contamination.

```

# Datacard produced by CombineHarvester with git status: analysis-HIG-16-006-freeze-080416-794-g1f6819a-dirty
imax   1 number of bins
jmax   1 number of processes minus 1
kmax   * number of nuisance parameters
-----
shapes * bin_qcdcr_hm_nbl_highmtb_ht1000to1300_MET_pt250to350 FAKE
-----
bin      bin_qcdcr_hm_nbl_highmtb_ht1000to1300_MET_pt250to350
observation 2498.0
-----
bin_qcdcr_hm_nbl_highmtb_ht1000to1300_MET_pt250to350
process          qcd          otherbkgs
process          1             2
rate            1902.07     167.667
-----
mcstats_otherbkgs_bin_qcdcr_hm_nbl_highmtb_ht1000to1300_MET_pt250to350 lnN   -       2
mcstats_qcd_bin_qcdcr_hm_nbl_highmtb_ht1000to1300_MET_pt250to350    lnN   1.03535   -
R_bin_qcdcr_hm_nbl_highmtb_ht1000to1300_MET_pt250to350           rateParam *      qcd      1 [0.01,5]

```

Figure 6.5 : An example of the datacard for the QCD CR.

statistical uncertainty which is a poisson error of  $\sqrt{N}$ . Then each process can have a systematic error that may be correlated to other backgrounds. In each process, we can have a value for the uncertainty or a dash which means that the uncertainty does not contribute to the process.

Finally at the bottom of the datacard we have the rate parameters for the backgrounds that require the extrapolation from units to SR bins. The units are a more basic definition of the SR bins that can be combined with the prediction of each background to give the total background in each SR bin. Since the LL, QCD, and  $Z \rightarrow \nu\nu$  backgrounds use an extrapolation method for the high  $\Delta m$  bins, we have defined 112 CR units and 529 SR units. In the bottom of Fig. 6.3, are the expected rates for the LL, QCD, and  $Z \rightarrow \nu\nu$  that show the combination of three units to give the prediction of each background in the respective bins. The rates from the LL and QCD background can be seen in Fig. 6.4 and 6.5. These are an example a single unit datacard. The calculation for each background from the unit CR is the data observation divided by the SM background in each,  $\frac{N_{data}^{CR}}{(N_{LL}^{CR} + N_{Sig}^{CR})}$  where the LL CR is used as an example. Now to be able to make the estimation of the limit for the

various SUSY processes that we are looking at, we need to combine the datacards for each SR bin for all of the signals in the mass parameter space. This can be easily accomplished thanks to the unique bin and process names for each signal. We can then input each of these combined datacards into the Higgs Combined Tool.

## 6.4 Higgs Combined Tool

The Higgs Combined Tool uses an asymptotic methods to compute the confidence level (CL) for each of the cross section limits. The tool is able to convert the datacards into a Likelihood function to calculate the limits. The Likelihood function is

$$L(r, \vec{\theta}) = \prod_i \frac{[r \cdot s_i(\vec{\theta}) + b_i(\vec{\theta})]^{n_i}}{n_i!} e^{-[r \cdot s_i(\vec{\theta}) + b_i(\vec{\theta})]} \prod_{\kappa} e^{-\frac{1}{2}\theta_{\kappa}^2}, \quad (6.1)$$

where  $r$  is the POI which is unconstrained only by the observed data,  $s_i(\vec{\theta})$  and  $b_i(\vec{\theta})$  are nuisance parameters which have external constraints. Each of these three parameters are jointly fitted to get a value of  $r$ .

## Appendix A

### Tau Multivariate Analysis

The identification of taus that decay hadronically has been under extensive study to distinguish whether the custom tau multivariate analysis (tauMVA), the isolated track (isotrack) method, or the MVA from that is provided by the tau POG (tau-POG). The custom tauMVA was trained on PF charged hadron candidates with  $p_T > 10 \text{ GeV}$  and  $|\eta| < 2.4$  along with an additional PF photon candidate, if any, with highest  $p_T > 0.5 \text{ GeV}$  and within a cone of  $\Delta R \leq 0.2$  of the charged hadron candidate. The tau candidate is also required to have a transverse mass  $m_T(\tau_h, \cancel{E}_T) < 100 \text{ GeV}$ , where  $m_T(\tau_h, \cancel{E}_T)$  is defined as follows,

$$m_T(\tau_h, \cancel{E}_T) = \sqrt{2 \cdot p_T(\tau_h + \text{nearest}\gamma) \cdot \cancel{E}_T \cdot (1 - \cos \Delta\phi)}. \quad (\text{A.1})$$

The addition of photons in the final definition is due to the possibility of taus decaying to neutral pions. This improves the resolution for the hadronic tau candidate. The inputs for the MVA are as follows:

- The  $p_T$  and  $|\eta|$  of the  $\tau$  candidate.
- The sum  $p_T$  of charged particles associated to the primary vertex within  $\Delta R$  cones of sizes 0.1, 0.2, 0.3, and 0.4 around the  $\tau$  candidate.
- The summed  $p_T$  of all particles within  $\Delta R$  cones of sizes 0.1, 0.2, 0.3, and 0.4 around the candidate, now including the neutral contribution from pileup parti-

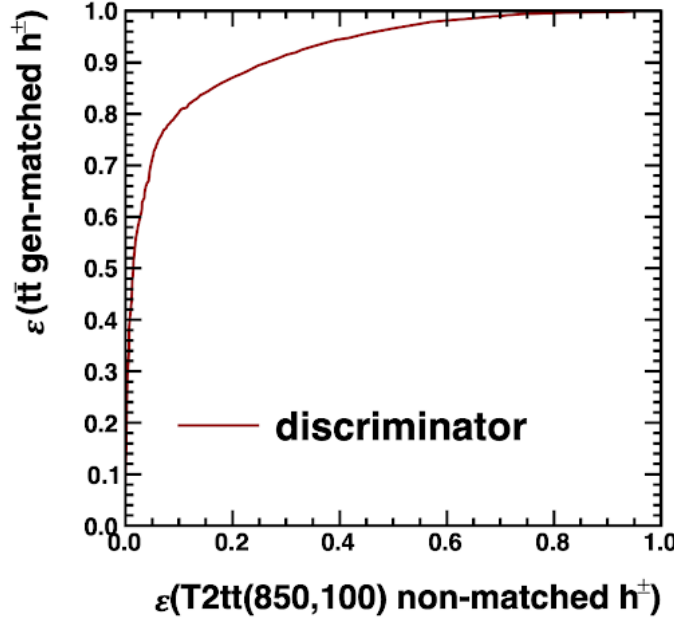


Figure A.1 : A Reciever operator characteristic curve for the tauMVA discriminator.

cles, which is reduced by applying the  $\Delta\beta$  correction to the neutral component of the isolation quantity.

- The distance in  $\Delta R$  to the nearest charged PF candidate with  $p_T > 1 \text{ GeV}$ .
- The distance in  $\Delta R$  to the axis of the jet containing the  $\tau$  candidate, and the b-tagging discriminant (DeepCSV) value for the jet, provided that the jet has  $p_T > 30 \text{ GeV}$  and  $|\eta| < 2.4$ .

Now that we have the definition for the TauMVA and have trained it on our samples to identify hadronically decaying taus. We want to compare the veto efficiencies and fake rates of the each method: TauMVA, IsoTrack, TauPOG, or a combination of IsoTrack and TauPOG. In Table A.3

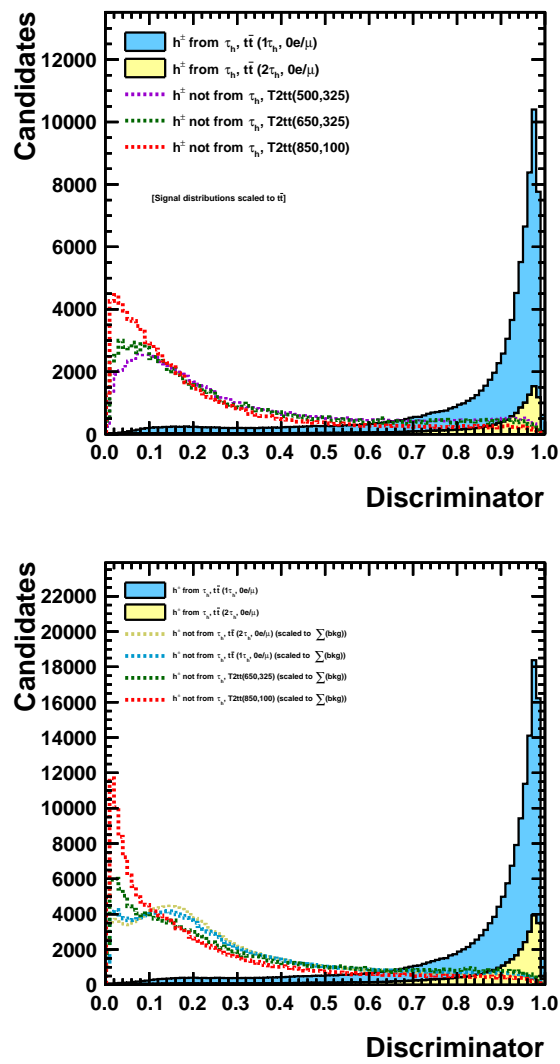


Figure A.2 : Tau MVA discriminator for different types of samples.

Type	Discriminator Cut	$t\bar{t}$ 1-lepton			$t\bar{t}$ Di-lepton		
		Efficiency	Fake Rate	Efficiency/Fake	Efficiency	Fake Rate	Efficiency/Fake
IsoTrack	-	27.9 %	6.1 %	4.541	24.8 %	6.1 %	4.084
TauMVA	0.68	34.9 %	6.9 %	5.046	24.7 %	5.3 %	4.689
TauMVA	0.70	34.6 %	6.5 %	5.355	24.4 %	4.9 %	4.997
TauMVA	0.71	34.4 %	6.2 %	5.525	24.2 %	4.7 %	5.170
TauMVA	0.73	33.9 %	5.7 %	5.914	23.8 %	4.3 %	5.540
TauMVA	0.74	33.6 %	5.5 %	6.119	23.6 %	4.1 %	5.712
TauMVA	0.75	33.4 %	5.2 %	6.356	23.4 %	3.9 %	5.961

Table A.1 : Comparing the efficiencies and Fake Rates of many difference discriminator cuts for the TauMVA and IsoTrack methods with SM simulation.

Type	Discriminator Cut	T1tttt(2000,100)			T2tt(850,100)		
		Efficiency	Fake Rate	Efficiency/Fake	Efficiency	Fake Rate	Efficiency/Fake
IsoTrack	-	7.4 %	2.9 %	2.503	5.5 %	2.0 %	2.704
TauMVA	0.68	5.7 %	8.1 %	0.696	4.8 %	4.7 %	1.017
TauMVA	0.70	5.5 %	7.5 %	0.735	4.7 %	4.4 %	1.075
TauMVA	0.71	5.5 %	7.2 %	0.760	4.7 %	4.2 %	1.102
TauMVA	0.73	5.4 %	6.6 %	0.806	4.6 %	3.9 %	1.175
TauMVA	0.74	5.3 %	6.3 %	0.832	4.5 %	3.7 %	1.214
TauMVA	0.75	5.2 %	6.0 %	0.869	4.5 %	3.5 %	1.262

Table A.2 : Comparing the efficiencies and Fake Rates of many difference discriminator cuts for the TauMVA and IsoTrack methods with two SUSY simulations.

Methods	$t\bar{t}$ 1-lepton		T1tttt(2000,100)		T2tt(850,100)	
	Veto Percentage	Veto Efficiency	Veto Percentage	Veto Efficiency	Veto Percentage	Veto Efficiency
TauMVA	32.2%	57.7%	12.9 %	10.7 %	6.5%	10.9 %
IsoTrack	21.3 %	37.9 %	4.4 %	2.5 %	2.6 %	6.6 %
TauPOG	171 %	29.7 %	7.0 %	3.2 %	5.2 %	2.5 %
IsoTrack + TauPOG	29.0 %	49.1 %	10.4 %	5.6 %	7.2 %	22.6 %

Table A.3 : Comparing the veto percentage and efficiency for the TauMVA, IsoTrack, and the IsoTrack + TauPOG methods with SM and SUSY simulations.

## Bibliography

- [1] F. Halzen and A. D. Martin, *Quarks and Leptons: An Introductory Course in Modern Particle Physics*. New York, Usa: Wiley ( 1984) 396p, 1984.
- [2] M. Peskin and D. Schroeder, *An Introduction to quantum field theory*. Addison-Wesley, 1995.
- [3] S. Chatrchyan and et al, “Observation of a new boson at a mass of 125 GeV with the CMS experiment at the LHC,” *Physics Letters B*, vol. 716, pp. 30–61, Sept. 2012.
- [4] S. P. Martin, “A Supersymmetry Primer,” *arXiv:hep-ph/9709356*, Sept. 1997. arXiv: hep-ph/9709356.
- [5] M. Cacciari, G. P. Salam, and G. Soyez, “The anti-ktjet clustering algorithm,” *Journal of High Energy Physics*, vol. 2008, pp. 063–063, Apr. 2008.
- [6] “JetID.”
- [7] “JEC.”
- [8] D. Griffiths, *Introduction to elementary particles*. Weinheim, Germany: Wiley-VCH (2008) 454 p, 2008.
- [9] “Performance of b tagging algorithms in proton-proton collisions at 13 TeV with Phase 1 CMS detector - CERN Document Server.”

- [10] “BtagRecommendation2016legacy.”
- [11] “BtagRecommendation94x.”
- [12] “BtagRecommendation102x.”
- [13] “Soft Drop - INSPIRE-HEP.”
- [14] “InclusiveSecondaryVertexFinder.”
- [15] “EgammaPublicData < CMSPublic < TWiki.”
- [16] “SWGuideMuonId < CMSPublic < TWiki.”
- [17] “The CMS Particle Flow Algorithm - INSPIRE-HEP.”
- [18] B. P. Roe, H.-J. Yang, J. Zhu, Y. Liu, I. Stancu, and G. McGregor, “Boosted Decision Trees as an Alternative to Artificial Neural Networks for Particle Identification,” Aug. 2004.
- [19] A. Hoecker, P. Speckmayer, J. Stelzer, J. Therhaag, E. von Toerne, H. Voss, M. Backes, T. Carli, O. Cohen, A. Christov, D. Dannheim, K. Danielowski, S. Henrot-Versille, M. Jachowski, K. Kraszewski, A. Krasznahorkay Jr., M. Kruk, Y. Mahalalel, R. Ospanov, X. Prudent, A. Robert, D. Schouten, F. Tegenfeldt, A. Voigt, K. Voss, M. Wolter, and A. Zemla, “TMVA - Toolkit for Multivariate Data Analysis,” *arXiv:physics/0703039*, Mar. 2007. arXiv: physics/0703039.
- [20] “Search for direct production of top squark pairs decaying to all-hadronic final states in pp collisions at  $\sqrt{s} = 13$  TeV - CERN Document Server.”

- [21] C. Bravo, “Search for Supersymmetric Top Quarks in pp Collisions at  $\sqrt{s} = 13$  TeV,” vol. CMS-AN-15-027, 2015.